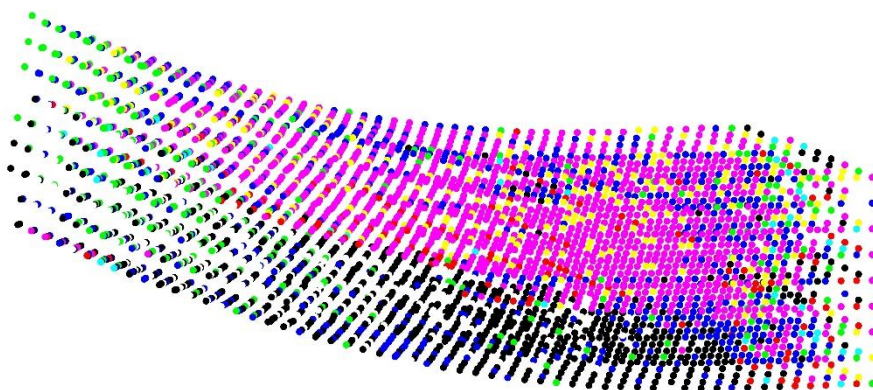


---

# MOLECULAR DYNAMICS SIMULATIONS OF POLARIZATION DOMAINS, PIEZOELECTRICITY & FLEXOELECTRICITY IN BARIUM TITANATE

---



---

Polytechnic University of Catalonia  
AMASE program  
Master Thesis

BSc. Edgar Abarca Morales



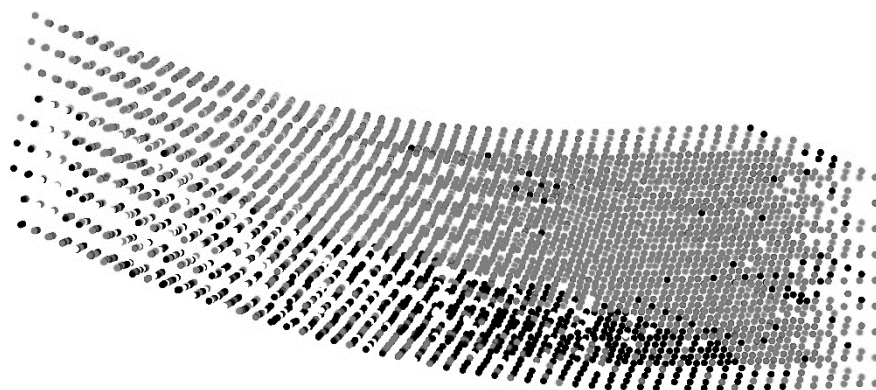
Erasmus+



---

# MOLECULAR DYNAMICS SIMULATIONS OF POLARIZATION DOMAINS, PIEZOELECTRICITY & FLEXOELECTRICITY IN BARIUM TITANATE

---



---

Polytechnic University of Catalonia  
AMASE program  
Master Thesis

Contact information: eamorales1990@gmail.com



Erasmus+



## About the supervisors

**Prof. Jorge Alcalá Cabrelles** is an associate professor at the Polytechnic University of Catalonia. His expertise lies in several Material's Science topics including Molecular Dynamics, Dislocation Dynamics, Finite Element Methods, Contact Mechanics, Material Mechanics, Micromechanics, Nanomechanics, Crystalline Plasticity, among others.

**Dr. Jan Ocenasek** is a researcher at the University of West Bohemia (Pilsen, Czech Republic). He has collaborated with Prof. Alcalá in many scientific publications mainly related to Nanomechanics, Micromechanics and Crystalline Plasticity.

## About the author



**Edgar Abarca Morales** is a physicist (BSc. in physics, 2016) graduated from the National Autonomous University of Mexico (UNAM). His background, interest and professional experience resides in solid state physics, nanotechnology and theoretical material science. Nowadays he is enrolled in the Advanced Materials Science and Engineering (AMASE) master's program coordinated by the European School of Materials (EUSMAT).

# INDEX

<b>Abstract</b> .....	7
<b>Abstract (Catalan version)</b> .....	8
<b>Abstract (Spanish version)</b> .....	9
<b>Literature Review</b> .....	10
Introduction to Molecular Dynamics Simulations .....	10
1.1.    The basics .....	10
1.2.    Interaction potentials .....	12
1.3.    Statistical ensembles and external fields .....	13
1.4.    Boundary conditions .....	14
1.5.    Flow chart of a MD simulation .....	14
Barium Titanate.....	15
2.1.    Overview.....	15
2.2.    Phase transitions .....	16
2.3.    Ferroelectricity .....	17
2.4.    The Takahashi model .....	18
The Core – Shell Model .....	20
3.1.    Overview.....	20
3.2.    Modeling of BTO.....	20
3.3.    Ab initio parameters fitting .....	21
3.4.    Parameters .....	22
Piezoelectricity .....	22
4.1.    Theoretical overview.....	22
4.2.    Piezoelectricity in BTO .....	23
Flexoelectricity .....	24
5.1.    Theoretical overview.....	24
5.2.    Flexoelectricity in BTO.....	25

<b>Computational Procedures .....</b>	26
Running a simulation in LAMMPS .....	26
1.1.    Introduction to LAMMPS.....	26
1.2.    Supercell definition for BTO .....	26
1.3.    Simulation scripts .....	28
1.4.    Output.....	32
Custom Graphical User Interface .....	35
2.1.    Overview.....	35
2.2.    Stereographic projection.....	36
2.3.    Global strain tensor measurements .....	38
Detailed objectives of the investigation .....	38
3.1.    Overview.....	38
3.2.    The simulations .....	38
<b>Results and Discussion.....</b>	42
Phase Diagram of BTO.....	42
1.1.    Spontaneous polarization.....	42
1.2.    Correlation with the Takahasi model .....	44
1.3.    Induced thermalization .....	47
1.4.    TP diagram construction.....	48
1.5.    Polarization near phase transitions .....	54
1.6.    Experimental comparison.....	58
Calculating the piezoelectric coefficients .....	60
2.1.    Simulation analysis.....	60
2.2.    The piezoelectric coefficients .....	61
Hysteresis cycles and ferroelectricity.....	62
3.1.    Simulation analysis.....	62
3.2.    Electric Susceptibility and dielectric constants .....	65

<b>Future work</b>	67
4.1.    Releasing the periodic boundaries	67
4.2.    Surface Modifications	68
4.3.    Indentation and bending	69
4.4.    Flexoelectricity at first glance	71
4.5.    Phonons in BTO	72
<b>Conclusion</b>	74
<b>Economic &amp; ecological impact</b>	75
<b>References</b>	76
<b>Appendix</b>	79
A:    Database	79
B:    Strain gradients	79
1.1.    Wedge deformation	80
1.2.    Circular bending	81
1.3.    Accordion bending	83
<b>Definitions</b>	85
<b>Acronyms</b>	87
<b>Mathematical conventions</b>	87

## ABSTRACT

The present work is a master thesis for the M.Sc. (Master of Science) double degree from AMASE (Advanced Materials Science and Engineering) international study program in collaboration with the Polytechnic University of Catalonia (UPC), funded by the Erasmus+ Programme of the European Union and coordinated by the European School of Materials (EUSMAT).

This thesis is a part of a project started in December 2016 in collaboration with Prof. Jorge Alcalá Cabrelles (UPC, Barcelona) and Dr. Jan Ocenasek (ZCU institute, Czech Republic) aiming to perform piezoelectric and flexoelectric studies in barium titanate by means of molecular dynamics simulations. The specific objective of this work is to gain expertise on molecular dynamics simulations of piezoelectric response, develop several analytical tools and characterize the basic thermodynamic and electric properties through a core-shell model of barium titanate fitted from first principle calculations.

With the emergence of increasingly powerful and cheap supercomputing, atomistic simulations are quickly becoming a very attractive and reliable method for testing materials at the nanoscale and mesoscale. This thesis provides a literature review regarding the basics of molecular dynamics simulations performed to investigate dielectric properties of barium titanate, which is a key archetypal material used in sensors and memory storage devices as well as in the development of new supercapacitors. This work comprises a series of 13 simulations of barium titanate aimed to characterize the spontaneous polarization developing in the ferroelectric phases, study the effect of externally applied electric fields, build the temperature versus pressure phase diagram, estimate the piezoelectric coefficients of the tetragonal phase, calculate the hysteresis loops, identify ferroelectric switching and analyze the paraelectricity of the cubic phase.

Furthermore, the limitations of simulating barium titanate using periodic boundary conditions are described and alternatives are given in the context of the investigation of flexoelectric response. Phonon dispersion is introduced as a key aspect to elucidate the underlying mechanisms in phase transformations. Finally, considerable amount of software has been developed to facilitate tracking, measuring and analysis of the physical properties in each simulation.

**Keywords:** Molecular dynamics, barium titanate, core-shell model, flexoelectricity.

## ABSTRACT (CATALAN VERSION)

Aquest treball és una tesi de mestratge per obtenir el grau de M.Sc. (Mestre en Ciències) amb doble titulació, atorgat pel programa d'estudis internacionals AMASE (Ciència i Enginyeria de Materials Avançada) en col·laboració amb la Universitat Politècnica de Catalunya (UPC), patrocinat pel programa Erasmus + de la Unió Europea i coordinat per la escola Europea de Materials (EUSMAT).

La tesi forma part d'un projecte amb començament el desembre del 2016 en col·laboració amb el professor Jorge Alcalá Cabrelles (UPC, Barcelona) i el doctor Jan Ocenasek (Institut ZCU, República Txeca) enfocat en realitzar estudis de piezoelectricitat i flexoelectricidad en titanat de bari mitjançant simulacions de dinàmica molecular. L'objectiu d'aquest treball consisteix a acumular experiència en simulacions de dinàmica molecular de la resposta piezoelèctrica, desenvolupar diverses eines d'anàlisi i caracteritzar les propietats termodinàmiques i elèctriques bàsiques partint d'un model core-shell de titanat de bari derivat de primers principis.

Amb l'aparició de superordinadors cada vegada més potents i econòmiques, les simulacions atomístiques s'estan convertint ràpidament en un mètode atractiu i fiable per provar materials en les escales nanomètrica i mesoscòpica. La tesi inclou una revisió literària establint els fonaments en simulacions de dinàmica molecular orientada a la investigació de les propietats dielèctriques del titanat de bari, el qual és un material arquetípic emprat en sensors i dispositius d'emmagatzematge, així com en el desenvolupament de nous supercapacitors. El treball engloba una sèrie de 13 simulacions de titanat de bari enfocades a caracteritzar la polarització espontània desenvolupada en les fases ferroelèctriques, estudiar l'efecte de camps elèctrics externs, construir el diagrama de fases de temperatura contra pressió, estimar els coeficients piezoelèctrics en fase tetragonal, calcular els cicles d'histeresi, identificar el canvi de polarització ferroelèctric i analitzar la paraelectricitat de la fase cúbica.

A més, es descriuen les limitacions presents en simular titanat de bari en condicions periòdiques i es proposen alternatives en el context de la investigació de la resposta flexoelèctrica. La dispersió de fonons és introduïda com un aspecte clau per elucidar els mecanismes presents en les transformacions de fase. Finalment, s'ha desenvolupat una gran quantitat de programari per facilitar el seguiment, el mesurament i l'anàlisi de les propietats físiques en cada simulació.

**Paraules clau:** Dinàmica molecular, titanat de bari, model core-shell, flexoelectricidad.

## ABSTRACT (SPANISH VERSION)

Este trabajo es una tesis de maestría para obtener el grado de M.Sc. (Maestro en Ciencias) con doble titulación, otorgado por el programa de estudios internacionales AMASE (Ciencia e Ingeniería de Materiales Avanzada) en colaboración con la Universidad Politécnica de Cataluña (UPC), patrocinado por el programa Erasmus+ de la Unión Europea y coordinado por la Escuela Europea de Materiales (EUSMAT).

La tesis forma parte de un proyecto con comienzo en diciembre del 2016 en colaboración con el profesor Jorge Alcalá Cabrelles (UPC, Barcelona) y el doctor Jan Ocenasek (Instituto ZCU, República Checa) enfocado en realizar estudios de piezoelectricidad y flexoelectricidad en titanato de bario mediante simulaciones de dinámica molecular. El objetivo de este trabajo consiste en acumular experiencia en simulaciones de dinámica molecular de la respuesta piezoeléctrica, desarrollar diversas herramientas de análisis y caracterizar las propiedades termodinámicas y eléctricas básicas partiendo de un modelo *core-shell* de titanato de bario derivado de primeros principios.

Con la aparición de supercomputadoras cada vez más potentes y económicas, las simulaciones atomísticas se están convirtiendo rápidamente en un método atractivo y confiable para probar materiales en las escalas nanométrica y mesoscópica. La tesis incluye una revisión literaria estableciendo los fundamentos en simulaciones de dinámica molecular orientada a la investigación de las propiedades dieléctricas del titanato de bario, el cual es un material arquetípico empleado en sensores y dispositivos de almacenamiento, así como en el desarrollo de nuevos supercapacitores. El trabajo engloba una serie de 13 simulaciones de titanato de bario enfocadas a caracterizar la polarización espontánea desarrollada en las fases ferroeléctricas, estudiar el efecto de campos eléctricos externos, construir el diagrama de fases de temperatura contra presión, estimar los coeficientes piezoelectricos en fase tetragonal, calcular los ciclos de histéresis, identificar el cambio de polarización ferroeléctrico y analizar la paraelectricidad de la fase cúbica.

Además, se describen las limitaciones presentes al simular titanato de bario en condiciones periódicas y se proponen alternativas en el contexto de la investigación de la respuesta flexoelectrica. La dispersión de fonones es introducida como un aspecto clave para elucidar los mecanismos presentes en las transformaciones de fase. Finalmente, se ha desarrollado una gran cantidad de software para facilitar el seguimiento, la medición y el análisis de las propiedades físicas en cada simulación.

**Palabras clave:** Dinámica molecular, titanato de bario, modelo core-shell, flexoelectricidad.

## LITERATURE REVIEW

This section consists of a literature review outlining and synthesizing the basic background needed to develop the current project. The concepts are covered following a specific order meant to first introduce the flow chart of molecular dynamic simulations and then relate it to barium titanate and the corresponding ferroelectric, piezoelectric and flexoelectric responses. Important concepts are *italicized* along the text and some of them are marked with the legend “(see definitions)”; the latter can be consulted in the *definitions* section at the end of this thesis. Also, acronyms are introduced only once in the text and certain mathematical conventions are employed. These can be consulted in the *acronyms* and *mathematical conventions* sections at the end of this thesis, respectively.

### INTRODUCTION TO MOLECULAR DYNAMICS SIMULATIONS

#### 1.1. THE BASICS

On its most general form, Molecular Dynamics (MD) is a series of computational steps aiming to numerically solve Newton’s equations of motion for an assembly of  $N$  particles. The term *particle* is always used in the classical way; that is, as being completely determined under the condition that for every value of  $t$  (*time*) within some interval, there exist elements  $\mathbf{r}$  (*position*) and  $\mathbf{p}$  (*momentum*) in an Euclidian tridimensional space.

In the case when particles have a one-to-one correspondence with atoms, MD methods are said to be *classical*; where each atom is represented by its position and momentum vectors. Nonetheless, more accurate MD in representing single molecules or crystals (for example) requires atoms to be treated not as single particles but as collections of them. Indeed, one atom could be represented by two classical particles: one accounting for its electronic degrees of freedom and the other carrying its ionic properties. Any MD treatment of atoms as a collection of particles is said to be *ab initio*, due to the properties of those particles (mass, charge, etc.) need to be known prior to MD. In this work, MD responds to an *ab initio* approach under what is called a *core - shell* model, to be detailed in the next sections. Nevertheless, in this section, MD will be discussed on its more general formulation; that is, in dealing with classical particles.

By considering that  $\mathbf{r}^{3N}(t) = \{\mathbf{r}_1(t), \mathbf{r}_2(t), \dots, \mathbf{r}_N(t)\}$  for the collection of  $N$  particles with  $3N$  coordinates at time  $t$ , the objective of MD is to solve the system of  $N$  coupled second-order differential equations<sup>1</sup>:

$$\mathbf{F}_j(\mathbf{r}^{3N}(t)) = m \frac{d^2 \mathbf{r}_j}{dt^2} = -\nabla_{\mathbf{r}_j} U(\mathbf{r}^{3N}(t))$$

Equation (1)

<sup>1</sup> The mass of the particles has been taken to be the same for simplicity.

Where  $\mathbf{F}$  is the force exerted on particle  $j$  and  $U$  is a prescribed interaction potential<sup>2</sup>. To numerically integrate equation (1), a specific algorithm called an *integrator* must be applied. There are several types of integrators that can be chosen considering *physical fidelity*, *computational efficiency* and *long-term stability* requirements (see definitions).

Commonly, integrators are divided into *symplectic* and *non-symplectic* whether they preserve or do not preserve the position-momentum space volume (phase space volume) among successive iterations, respectively.

The specific role of the integrator is to divide the total simulation time  $L * \Delta t$  into  $L$  steps of width  $\Delta t$  such that solutions to equation (1) are obtained iteratively through the whole integration process:  $\mathbf{r}^{3N}(t_0) \rightarrow \mathbf{r}^{3N}(t_1) \rightarrow \dots \rightarrow \mathbf{r}^{3N}(t_L)$ . The typical value for  $\Delta t$  in MD is 1 *femtosecond* while  $L$  can range from  $10^4$  to  $10^8$ ; this is equivalent to maximum simulation times of about 10 *nanoseconds*. For times higher than this value, physical fidelity is compromised due to the accumulation of floating-point round-off errors and the non-preservation of phase space volume when using non-symplectic integrators [1].

One of the simplest integrators is the *Verlet* or *leapfrog* (symplectic) integrator, which is described here to illustrate how equation (1) can be iteratively solved. Supposing the initial conditions of the system  $\{\mathbf{r}^{3N}(t_0), \dot{\mathbf{r}}^{3N}(t_0)\}$  are known, expanding the position functions  $\mathbf{r}_j(t)$  around  $t_0 + \Delta t$  and  $t_0 - \Delta t$  and then adding them gives:

$$\mathbf{r}_j(t_0 + \Delta t) = \mathbf{r}_j(t_0) + \mathbf{v}_j(t_0)\Delta t + \frac{1}{2}\mathbf{a}_j(t_0)(\Delta t)^2 + \dots$$

$$\mathbf{r}_j(t_0 - \Delta t) = \mathbf{r}_j(t_0) - \mathbf{v}_j(t_0)\Delta t + \frac{1}{2}\mathbf{a}_j(t_0)(\Delta t)^2 + \dots$$

$$\mathbf{r}_j(t_0 + \Delta t) = -\mathbf{r}_j(t_0 - \Delta t) + 2\mathbf{r}_j(t_0) + \mathbf{a}_j(t_0)(\Delta t)^2 + \dots$$

Equation (2)

Where the definitions  $\mathbf{v} = \dot{\mathbf{r}} = \frac{d\mathbf{r}}{dt}$  and  $\mathbf{a} = \ddot{\mathbf{r}} = \frac{d^2\mathbf{r}}{dt^2}$  have been applied as usual. Equation (2) induces an iterative process on which the only unknown is  $\mathbf{a}_j(t_0)$ ; however, substituting equation (1) yields:

$$\mathbf{r}_j(t_{n+1}) = -\mathbf{r}_j(t_{n-1}) + 2\mathbf{r}_j(t_n) - \frac{\nabla_{\mathbf{r}_j} U(\mathbf{r}^{3N}(t_n))}{m} (\Delta t)^2 + \dots$$

Equation (3)

<sup>2</sup> A more detailed explanation regarding the interaction potential will be done in the following sections.

For  $n = 1, \dots, L - 1$ ; thus, equation (1) can be integrated over a desired time if the functional form of the interaction potential is known. It should be noticed that a small interval  $\Delta t$  is required to achieve lower error tolerances due to the truncated series; moreover, the floating-point round-off errors accumulated during the numerical computation of the gradient<sup>3</sup> could be reduced but are at all costs inescapable, leading to loss of physical fidelity and possibly long-term stability for arbitrarily large simulation times.

## 1.2. INTERACTION POTENTIALS

As it can be seen from equation (3), all the physics of a specific MD simulation is inscribed by the interaction potential  $U$ . Although the dependence of the potential on the particles positions  $\mathbf{r}^{3N}$  could be extremely complex, it turns out that approximating its functional form as a sum of  $N$ -body interactions considerably simplifies the problem if the sum is truncated at the expense of some physical fidelity. That is, the potential  $U$  may be written as:

$$U(\mathbf{r}^{3N}) = \sum_{j=1}^N V_1(\mathbf{r}_j) + \sum_{i < j}^N V_2(\mathbf{r}_i, \mathbf{r}_j) + \sum_{i < j < k}^N V_3(\mathbf{r}_i, \mathbf{r}_j, \mathbf{r}_k) + \dots$$

Equation (4)

The first term  $V_1$  represents the coupling of any of the  $N$  particles to an external applied field (electric, magnetic, etc.). Meanwhile,  $V_2$  exclusively models the pairwise interaction between any couple of particles,  $V_3$  accounts only for 3-body interactions, and so on. Even though this may appear as a rough approximation, for certain systems lots of physical properties can be simulated by truncating equation (4) up to pairwise interactions. Moreover,  $V_2$  can be further simplified by considering it as being central, that is, only dependent on the distance  $r_{ij} = |\mathbf{r}_i - \mathbf{r}_j|$  between particles. An example of this kind is the well-known Lennard – Jones potential which relies on two parameters to be fitted experimentally (see figure 1) [2].

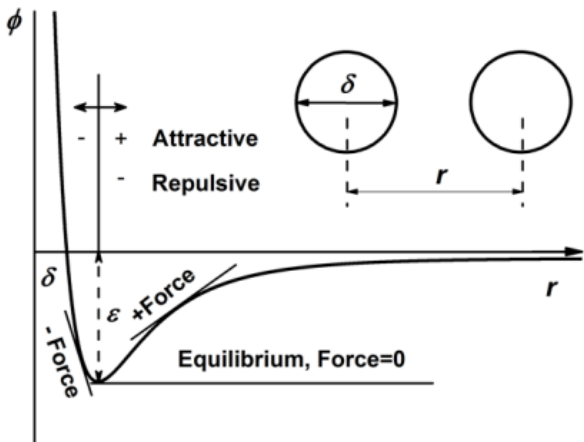


Figure 1 – The Lennard Jones potential  $\phi(r)$  is dependent on two parameters:  $\epsilon$  which models its depth (strength of the interaction) and  $\delta$  which represents the separation distance at zero energy.

Figure taken from [2].

<sup>3</sup> A vast number of algorithms to compute derivatives exists within the field of numerical methods; those will not be addressed here for the sake of brevity.

Many potentials exist in the literature, aiming to describe different systems subjected to different conditions. The best way to validate the applicability of a certain potential is to calculate an expected property of the real system that has not been used in fitting the potential. If the calculation provides a reasonably accurate result, a test of the *transferability* of the potential has been provided. That is, the potential shows to be adequate in describing the physical system and the robustness of the model allows for predictive assertions.

### 1.3. STATISTICAL ENSEMBLES AND EXTERNAL FIELDS

Even though equation (1) can be solved for the system of  $N$  particles, the specific constraints have not yet been specified. Usually, in classical mechanics, constraints are introduced via sets of equations which restrict the possible behavior of the system; for example, by setting constant the distance between any two particles <sup>4</sup> [3]. Nevertheless, in MD, the introduction of *holonomic* and *non-holonomic* constraints is used to statistically restrict the behavior of the system in such way that it resembles the control capabilities over its macroscopic or thermodynamic properties; that is, rather than “freezing” or restricting the motion of a group of particles by directly pinning them with a certain function, statistical variables such as *temperature* or *pressure* can be defined, fixed and measured during the simulation. In general, these statistical variables, which link thermodynamics and mechanics via equilibrium statistical mechanics are all encompassed within the concept of a *statistical ensemble* (see definitions).

Some of the most typical statistical ensembles are the *microcanonical* or NVE ensemble, some variants of the *canonical* ensemble like the NVT or NPT ensembles and the *grand canonical ensemble*  $\mu$ VT. In each case, the total number of particles  $N$ , the volume  $V$ , the total energy  $E$ , the pressure  $P$  or the chemical potential  $\mu$  remain fixed to a certain value; thus for example, using an NPT ensemble fixes the number of particles in the system, its pressure and its temperature [4]. Although the analytical *partition functions* (see definitions) for each of the afore ensembles exist, the definition and control of the required thermodynamic variables is achieved using certain techniques which emulate the behavior of temperature, pressure, etc. by modifying the equations of motion and the integrator.

A very popular algorithm in controlling MD temperature is the *Nose - Hoover thermostat*; its purpose is to modify equation (1) by the introduction of a frictional degree of freedom  $\zeta(t)$  aiming to slow down the motion of the particles until a certain value of temperature is measured by means of the *kinetic energy* and the *equipartition theorem* for the system (see definitions) [5]. The equations of motion can be thus written as follows:

$$m_i \frac{d^2 \mathbf{r}_i}{dt^2} = \mathbf{F}_i - \zeta(t)m_i \mathbf{v}_i$$

---

<sup>4</sup> Also known as the rigid body constraint.

$$\frac{d\zeta(t)}{dt} = \frac{1}{Q} \left[ \sum_{i=1}^N m_i \frac{v_i^2}{2} - \frac{3N+1}{2} k_B T \right]$$

Equation (5)

Being  $Q$  a relaxation parameter and  $k_B$  the Boltzmann constant. An integrator can then be written for equation (5) at a target temperature  $T$  defined by the user. Similarly, a very well-known algorithm for controlling pressure is the so called *Berendsen barostat*. Its functionality is similar the Nose – Hoover thermostat but in terms of a target pressure  $P$ <sup>5</sup> [6]. In this work, both a thermostat and a barostat will be employed to account for the thermodynamics of barium titanate. Furthermore, in addition to thermodynamic ensembles, constant forces depending on particle parameters like mass or charge can be added to the dynamical equations to simulate externally applied fields (electric, magnetic, etc.).

---

#### 1.4. BOUNDARY CONDITIONS

In general, MD can be applied to a wide variety of systems ranging from isolated molecules to evaporating liquids, gases, proteins and crystals. On each case, boundary conditions should be defined. While in the case of molecules like proteins non-periodic boundary conditions seem perfectly reasonable to study the isolated nature of those entities, for bulk systems such as gases liquids or crystals the introduction of periodic boundary conditions enhances simulation stability and eliminates surface effects. Specifically, as will be discussed in the next sections, barium titanate will be introduced as a crystal and therefore the most employed periodic boundary conditions are the *Born-von-Karman* [7].

The basic statement of such conditions is that any wave or observable in the crystal should have the same value in position  $\mathbf{r}$  as it has in position  $\mathbf{r} + \mathbf{L}$ , where  $\mathbf{L} = [L_x \ L_y \ L_z]$  is the sample length vector with components in directions  $x$ ,  $y$  and  $z$  respectively. Thus, the system can be visualized to have the same topology as a hypertorus such that travelling in any direction will result into physical periodicity.

---

#### 1.5. FLOW CHART OF A MD SIMULATION

Once having exposed the heart of MD simulations, the full procedure can be summarized technically (see figure 2). The second step consists in defining the initial conditions  $\{\mathbf{r}^{3N}(t_0), \dot{\mathbf{r}}^{3N}(t_0)\}$ , that is, assigning particles initial position and velocity. Meanwhile the particles position can be read directly from a pre-built file defined by the user, initial particle velocities are usually assigned on-the-go according to *Maxwell-Boltzmann* or *Gaussian* distributions for a given target temperature  $T$  (see definitions). In the third step, the interaction potential is “turned on” by means of calculating the force on each particle and then the iterative process of the integrator begins (see equation 3, for example). At the end of any step the coordinates and velocities of the system can be saved to file.

---

<sup>5</sup> The Berendsen barostat will not be discussed further for the sake of brevity.

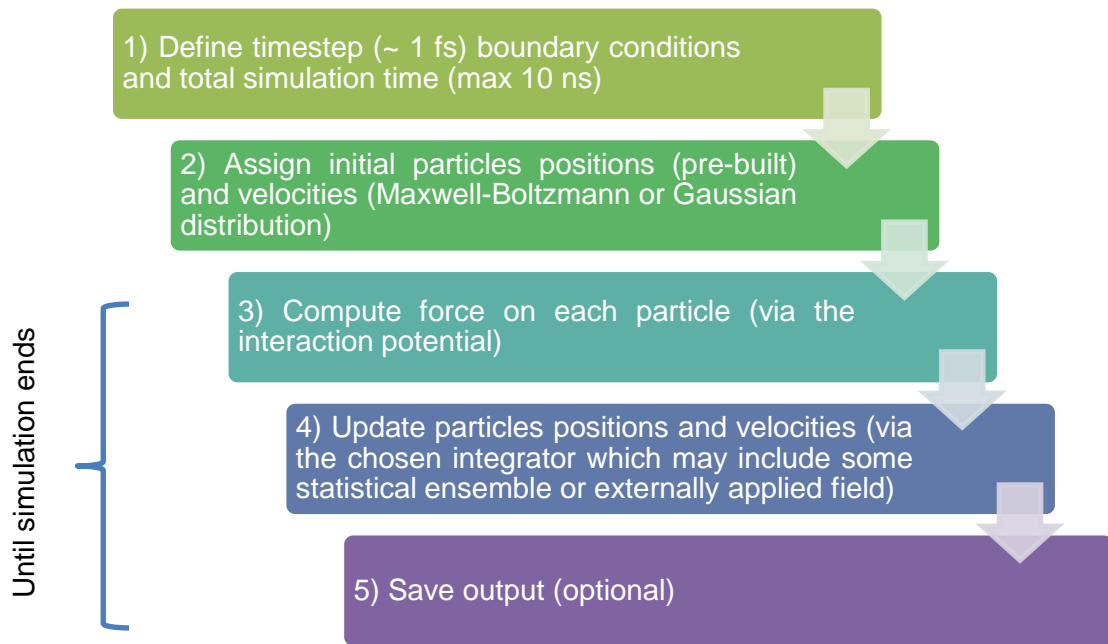


*Figure 2 – Flow chart of a molecular dynamics simulation. The iterative process triggered by the integrator continues until the simulation ends.*

It should be noted that the integrator may be supported based on a specific statistical ensemble in which case the related thermodynamic variables (temperature, pressure, etc.) should be defined prior to the iterative process. The explicit way the thermostat and barostat are controlled in a simulation will be addressed in the *computational procedures* section of this thesis.

## BARIUM TITANATE

### 2.1. OVERVIEW

Barium titanate (BTO) is a ferroelectric ceramic material with the *perovskite* structure  $A^{2+}B^{4+}X_3^{2-}$  where  $A$ ,  $B$  and  $X$  are the barium, titanium and oxygen ions, respectively. The ferroelectric behavior of BTO makes it an excellent candidate for ultra-high capacitance applications and development of memory devices. Moreover, ferroelectric materials play a major role in microelectronics, integrated optics and optoelectronics. Also, BTO shows interesting piezoelectric, flexoelectric, pyroelectric and photorefractive effects [8] [9] [10] [11].

The crystalline structure of BTO can be described by simple cubic, tetragonal, orthorhombic and rhombohedral lattices, depending on temperature. In studying the electric behavior of BTO, it is useful to define the primitive unit cell as shown in figure 3 [12]; while the atom basis can be defined in units of the primitive lattice vectors as follows:

$$Ba = [0 \ 0 \ 0]$$

$$O_{xy} = \begin{bmatrix} 1 & 1 & 0 \end{bmatrix} \quad O_{xz} = \begin{bmatrix} 1 & 0 & 1 \end{bmatrix} \quad O_{yz} = \begin{bmatrix} 0 & 1 & 1 \end{bmatrix}$$

$$Ba = \begin{bmatrix} 1 & 1 & 1 \end{bmatrix}$$

Equation (6)

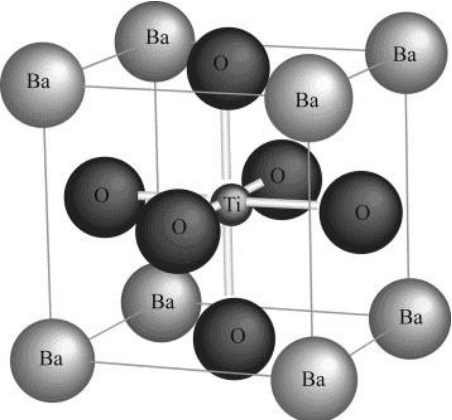


*Figure 3 – Primitive unit cell for BTO.* This representation is useful due to the clear and symmetric visualization of the titanium atom, whose displacement accounts for the ferroelectric properties of BTO (see section 2.3. of this chapter).

Figure taken from [12].

## 2.2. PHASE TRANSITIONS

In the absence of applied pressure, BTO undergoes phase transformations from a high-temperature paraelectric cubic phase to three low temperature ferroelectric phases with tetragonal, orthorhombic and rhombohedral geometry, respectively. The order-disorder versus the displacive character of these transitions is still a subject of debate. Both types of transitions have been supported by experimental evidence; the displacive character proved to be consistent with the softening of T-O phonon modes detected by neutron scattering which leave the titanium atom in an unstable transition within the oxygen octahedra. On the other hand, the relaxational dynamics of the order-disorder behavior has been accounted by several experimental techniques including X-ray diffuse scattering, electric paramagnetic resonance (EPR), nuclear magnetic resonance (NMR), convergent-beam electron diffraction (CBED), among others [8] [13].

Furthermore, a local order-disorder model of phase transformations based in the off-centering of the titanium atom towards the  $\langle 1\ 1\ 1 \rangle$  directions was proposed by Takahasi et al. in 1961; nevertheless, no local structures related to an order-disorder character were observed before 2012, when the work of Tsuda et al. proved their existence by means of CBED analysis of lattice symmetries [13] [14]. In table 1, BTO phases are briefly described as a function of temperature in the absence of applied pressure; the symmetry groups and expected electric behavior are also shown. Besides, the application of hydrostatic pressure can induce phase transitions in BTO (see figure 4) [15].

Temperature range (K)	Lattice	Space group	Electric behavior
0 – 180	Rhombohedral	R3m	Ferroelectric
180 - 290	Orthorhombic	Amm2	Ferroelectric
290 - 400	Tetragonal	P4mm	Ferroelectric
400 – HT phase	Cubic	Pm3m	Paraelectric

Table 1 – BTO phases at atmospheric pressure, ferroelectricity is lost in the tetragonal-to-cubic phase transition for a Curie point of nearly 400K.

Transition temperatures taken from [15].

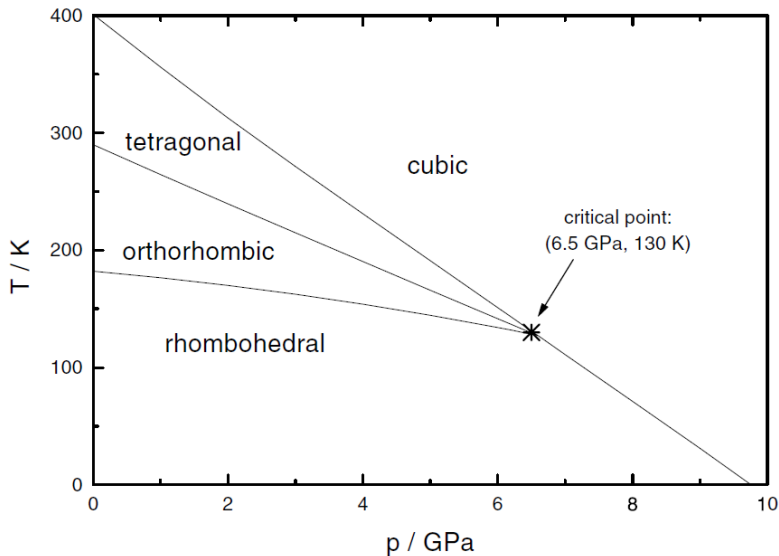


Figure 4 – Phase diagram for BTO based on low-pressure experiments and classical extrapolation. The application of hydrostatic pressure can lead to phase transitions; moreover, a critical point appears at a pressure of 6.5 GPa and temperature of 130K.

Figure taken from [15].

### 2.3. FERROELECTRICITY

Due to crystallographic symmetries, the ferroelectric nature of BTO implies that it is also pyroelectric, piezoelectric and non-centrosymmetric. The ferroelectric properties of BTO emerge from off-centering distortions of the titanium atom with respect to the oxygen octahedra; besides, the distortions seem to be unaffected by means of thermal fluctuations [8] [16]. At any temperature from 0K to the tetragonal-to-cubic transition (~400K, 0GPa) spontaneous and reversible polarization density is observed and thus hysteresis is also present. Explicitly, the off-centering of the titanium atom generates a net electric dipole moment which can be computed as follows [17]:

$$P_{\alpha m} = \frac{1}{V_m} \left[ \sum_i \sum_{v=1}^2 q_{ivm} r_{iv\alpha m} \right]$$

Equation (7)

Where  $P_{\alpha m}$  is the polarization density of the primitive unit cell  $m$  in the direction  $\alpha$ ,  $V$  is the cell volume,  $q$  is electric charge,  $r$  is position component and  $i$  and  $v$  refer to a specific atom in the basis and to a nuclear or ionic degree of freedom, respectively. As usual, for a bulk crystal the polarization density  $\mathbf{P}$  satisfies the classical electromagnetism relation [18].

$$\mathbf{D} = \epsilon_0 \mathbf{E} + \mathbf{P}$$

Equation (8)

On which  $\mathbf{D}$  is the electric displacement field,  $\mathbf{E}$  is an externally applied electric field and  $\epsilon_0$  is the vacuum permittivity. For dielectric materials such as BTO, the polarization density is quite generally linearly dependent on the applied electric field, yielding:

$$\begin{aligned}\mathbf{P} &= \epsilon_0 [\mathbf{X}] \mathbf{E} \\ \mathbf{D} &= \epsilon_0 [\mathbf{I} + \mathbf{X}] \mathbf{E} = \epsilon_0 [\boldsymbol{\epsilon}_r] \mathbf{E} = [\boldsymbol{\epsilon}] \mathbf{E}\end{aligned}$$

Equation (9)

Where  $[\mathbf{X}]$  is the electric susceptibility tensor,  $[\mathbf{I}]$  is the identity tensor,  $[\boldsymbol{\epsilon}_r] \equiv [\mathbf{I} + \mathbf{X}]$  is the relative electric permittivity and  $[\boldsymbol{\epsilon}] \equiv \epsilon_0 [\boldsymbol{\epsilon}_r]$  is the electric permittivity of the material. Nonetheless, equation (9) should be carefully applied in the case of BTO due to its ferroelectric and thus hysteresis properties <sup>6</sup>. The matrix representations of  $[\mathbf{X}]$  considering the point group symmetries of the rhombohedral, orthorhombic, tetragonal and cubic phases are, respectively [19]:

$$[\mathbf{X}]_r \doteq \begin{bmatrix} X_{11} & 0 & 0 \\ 0 & X_{11} & 0 \\ 0 & 0 & X_{33} \end{bmatrix} \quad [\mathbf{X}]_o \doteq \begin{bmatrix} X_{11} & 0 & 0 \\ 0 & X_{22} & 0 \\ 0 & 0 & X_{33} \end{bmatrix} \quad [\mathbf{X}]_t \doteq \begin{bmatrix} X_{11} & 0 & 0 \\ 0 & X_{11} & 0 \\ 0 & 0 & X_{33} \end{bmatrix} \quad [\mathbf{X}]_c \doteq X_{11} \mathbf{I}$$

Equation (10)

## 2.4. THE TAKAHASI MODEL

On behalf of the order-disorder vs. displacive character of phase transformations in BTO, Takahasi et al. postulated a model where local structures defined by a specific directionality for the off-centering of the titanium atom could be formed. The off-centering would be restricted within the eight  $\langle 1 1 1 \rangle$  directions in the primitive unit cell and their occupancy would be ruled by thermal activation (see figure 5) [13] [14].

Explicitly, starting at 0K the off-centering of the titanium atom can point only in one  $\langle 1 1 1 \rangle$  direction for every unit cell in the crystal, thus generating a local and global rhombohedral symmetry due to the corner-pointing distortion (see figure 5a). However, when the temperature reaches certain level a phase transition is marked by the occupancy of another  $\langle 1 1 1 \rangle$  direction which induces a global orthorhombic symmetry due to the

---

<sup>6</sup> Equation (9) predicts null polarization density for no external electric field. This is incorrect for a hysteresis cycle where the remnant or spontaneous polarization needs to be considered.

average in off-centering of individual unit cells; besides, local structures of rhombohedral character are always present with a minimum size of a unit cell (see figure 5b). The next phase transition is defined by the occupancy of a total of 4  $\langle 1\ 1\ 1 \rangle$  directions generating an average tetragonal distortion of the lattice even when local rhombohedral or even orthorhombic distortions may be present (see figure 5c).

Furthermore, in the three scenarios already treated the titanium distortion generates a non-zero polarization density and thus ferroelectricity can be explained. This is not the case for the high temperature paraelectric cubic phase on which the occupancy of all  $\langle 1\ 1\ 1 \rangle$  directions yield an average null titanium displacement; yet rhombohedral, orthorhombic and tetragonal local distortions may still be present in the crystal (see figure 5d).

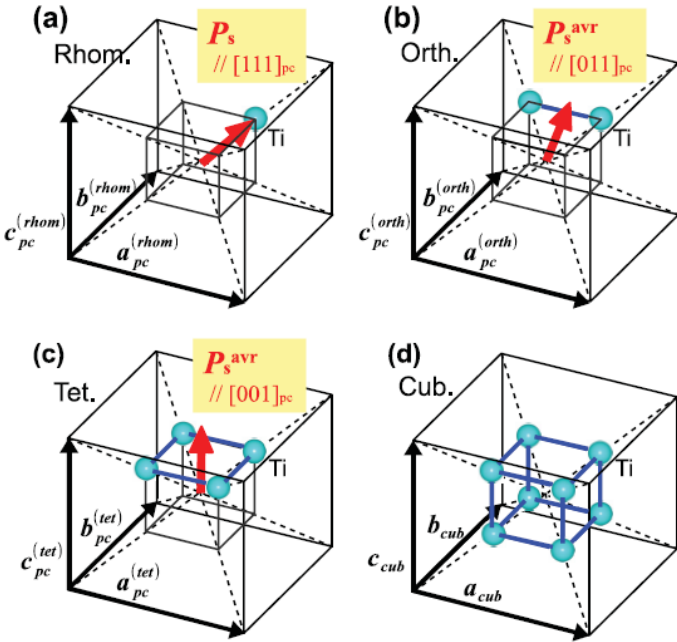


Figure 5 – The Takahashi model for phase transitions in BTO in terms of a discretized titanium off-centering. On each case the lattice constants  $a$ ,  $b$  and  $c$  are shown in pseudocubic axes due to a relatively little distortion compared to the cubic phase.

Figure taken from [13].

The local structures predicted by the Takahashi model were visualized by Tsuda et al. by means of CEBD. They discovered that while the symmetries expected for the rhombohedral ( $R\bar{3}m$ ) space group were present at the rhombohedral BTO phase, the symmetries for the orthorhombic ( $Amm2$ ) and tetragonal ( $P4mm$ ) space groups were broken at the orthorhombic and tetragonal BTO phases when the material is studied at the nanometer length scale [13]. Furthermore, the predictions made by the Takahashi model have been consistently validated by means of quantum mechanical density functional theory (DFT) simulations [20]. Nonetheless, the mechanisms driving the occupancy of the  $\langle 1\ 1\ 1 \rangle$  directions and its relation to experimental results suggesting onset of displacive phase transitions are still unknown. In fact, recent evidence suggests coexistence rather than mutual exclusion between the order-disorder and the displacive pictures, where slower dynamics of cluster polarization flipping and a faster order-disorder titanium hopping toward the  $\langle 1\ 1\ 1 \rangle$  directions are reconciled. Additionally, Heisenberg spin-like models have been developed in order to extrapolate the capabilities of the Takahashi model to the mesoscale [8].

## THE CORE – SHELL MODEL

### 3.1. OVERVIEW

Obtaining a reliable model for the interaction potential must be addressed to simulate BTO by means of MD. Its electronic properties could be much better described if a splitting between the electronic and ionic degrees of freedom is made; therefore, the atoms in BTO will not be treated themselves as single particles but as couples of them, one carrying the electronic information and the other accounting for the ionic behavior in what is called a *core-shell model*. This assumption necessarily requires the MD simulation to be *ab initio*; thus the parameters fitting the interaction potentials need to be acquired a priori from calculations or experiments such that a wave function description is used for the electronic degrees of freedom [1].

### 3.2. MODELING OF BTO

The interaction potential for BTO will be built as the sum of three contributions. The interaction between the cores of the atoms in BTO will be modeled with a Buckingham short-range potential of the form:

$$\phi^B(r) = A e^{-\frac{r}{\rho}} - \frac{C}{r^6}$$

Equation (11)

On which  $r$  is the distance separating both cores and  $A$ ,  $\rho$  and  $C$  are fitting parameters. Meanwhile, the core-shell interaction within one atom will be described via an anharmonic isotropic spring potential that can be written as:

$$\phi^S(r) = \frac{1}{2}k_2 r^2 + \frac{1}{24}k_4 r^4$$

Equation (12)

Where  $k_2$  and  $k_4$  are fitting parameters. Improvements on this potential include the addition of anisotropic terms that distinguish between longitudinal and transversal vibrations in the core-shell interaction within oxygen atoms<sup>7</sup> [21]. Finally, all cores and shells interact between each other via Coulomb's law except for the core and shell of the same atom:

$$\phi^C(r) = \frac{1}{4\pi\epsilon_0} \frac{q_a q_b}{r}$$

Equation (13)

<sup>7</sup> The anharmonic anisotropic potential for the core-shell interaction will not be discussed in this work; however, its application is currently available in LAMMPS thanks to Dr. Jan Ocenasek (see the experimental section for a definition of LAMMPS).

With  $a \neq b$  and the electric charges being fitting parameters. Therefore, the electric charge for the core and shell of different atoms, the spring constants between the core and shell of the same atom and the parameters of the Buckingham potential for the cores, need to be obtained for BTO. A graphic summary of the modeled interactions is shown in figure 6 [22].

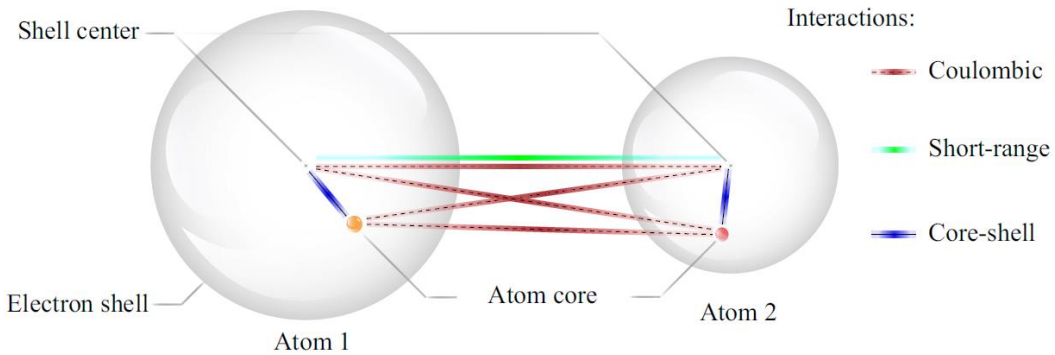


*Figure 6 – Schematic representation of interactions among atoms in the core-shell model for BTO.*

Figure taken from [22].

### 3.3. AB INITIO PARAMETERS FITTING

The core-shell model for BTO was fitted by Vielma et al. based on DFT calculations using the Perdew-Burke-Ernzehof generalized gradient approximation for solids (PBEsol); which leads to very accurate lattice parameters for the ground state and much better oxygen-titanium displacements in BTO. The DFT approach is generally easier and much less computationally demanding than solving an effective model Hamiltonian [23].

The fitting parameters were found via least squares minimization between the core-shell model (see equations 11 to 13) and DFT energy differences in the potential energy surface:

$$\chi^2 = \sum_{i=1}^N \sigma_i^2 [(E_{C,DFT} - E_{i,DFT}) - (E_{C,CS} - E_{i,CS})]^2$$

Equation (14)

Where  $\chi^2$  was minimized using the Nelder-Mead Downhill Simplex Method,  $E_{CS}$  and  $E_{DFT}$  respectively refer to core-shell and DFT potential energy surface,  $C$  defines a perfect cubic structure employed as reference and  $i$  tags different configurations weighted by the factor  $\sigma$ . In the work of Vielma et al. the sum runs over 2200 different structures including cubic, tetragonal, orthorhombic and rhombohedral phases of BTO [23].

### 3.4. PARAMETERS

The set of *ab initio* parameters for the core-shell model of BTO obtained from Vielma et al. are shown in table 2. The applicability of those parameters have been successfully tested in the literature regarding MD simulations of BTO [22] [23].

Atoms	Core charge	Shell charge	$k_2$	$k_4$
	$ e $	$ e $	$eV/\text{\AA}^2$	$eV/\text{\AA}^4$
Ba	5.042	-2.870	298.51	0.0
Ti	4.616	-1.544	306.14	500.0
O	0.970	-2.718	36.93	5000.0
Buckingham	$A(eV)$	$\rho(\text{\AA})$	$C(eV/\text{\AA}^6)$	
Ba - O	7149.81	0.3019	0.0	
Ti - O	7220.27	0.2303	0.0	
O - O	3719.60	0.3408	597.17	

Table 2 – Anharmonic isotropic core-shell model parameters for BTO obtained from DFT first principle calculations.

Parameters taken from [22].

## PIEZOELECTRICITY

### 4.1. THEORETICAL OVERVIEW

Piezoelectricity is the generation of polarization density in response to applied mechanical stress shown by certain materials; specifically, crystals with no inversion symmetry [24]. Theoretically, piezoelectricity can be described as a linear electromechanical interaction due to the coupling of equation (9) with the classical stress-strain continuum mechanics relation:

$$[S] = [s][\sigma]$$

Equation (15)

Being  $[s]$  the 4-rank compliance tensor relating the stress tensor  $[\sigma]$  with the strain tensor  $[S]$ <sup>8</sup>. Thus, equations (9) and (15) simultaneously yield the system of coupled equations:

$$D = [\delta][\sigma] + [\varepsilon]E$$

$$[S] = [s][\sigma] + [\delta^\dagger]E$$

Equation (16)

Where  $[\delta]$  is the 3-rank piezoelectric tensor and  $[\delta^\dagger]$  refers to the associated transposed matrix of  $[\delta]$  written using *Voigt notation* (see definitions) [25]. While the first equation accounts for the *direct piezoelectric effect* on which a displacement field is induced due to applied mechanical stress in the absence of an external electric field, the second equation describes the *converse piezoelectric effect* where in the absence of applied mechanical stress an external electric field generates deformation. Hence, the equations consistently account for the reversibility of the piezoelectric effect. For the case of MD simulations is simpler to calculate  $[\delta]$  by exploiting the converse piezoelectric effect since measuring strain from the coordinates of particles while knowing the external electric field is easier than measuring displacement fields while knowing the applied mechanical stress. To measure  $[S]$  a continuum approach can be followed for the bulk of the crystal such that the classical equation holds:

$$[S] = \frac{1}{2}([F^\dagger][F] - [I])$$

Equation (17)

On which  $[F]$  is the deformation gradient tensor with components given by:

$$F_{ij} = \frac{\partial x_i}{\partial X_j}$$

Equation (18)

Such that  $X$ 's are the coordinates before deformation and  $x$ 's are the coordinates after deformation; thus, with  $[S]$  following a Lagrangian description.

## 4.2. PIEZOELECTRICITY IN BTO

Focusing in the highest temperature ferroelectric phase of BTO, which exhibits a macroscopic tetragonal symmetry, the system of coupled equations (16) can be further simplified by considering the symmetries of the space group *P4mm*, yielding the following matrix relations for the direct and converse piezoelectric effect, respectively [26]:

---

<sup>8</sup> The notation  $[\varepsilon]$  was not employed for the strain tensor to avoid confusion with the electric permittivity  $\varepsilon$ .

$$\begin{bmatrix} D_1 \\ D_2 \\ D_3 \end{bmatrix} = \begin{bmatrix} 0 & 0 & 0 & 0 & d_{15} & 0 \\ 0 & 0 & 0 & d_{15} & 0 & 0 \\ d_{31} & d_{31} & d_{33} & 0 & 0 & 0 \end{bmatrix} \begin{bmatrix} \sigma_1 \\ \sigma_2 \\ \sigma_3 \\ \sigma_4 \\ \sigma_5 \\ \sigma_6 \end{bmatrix} + \begin{bmatrix} \varepsilon_{11} & 0 & 0 \\ 0 & \varepsilon_{22} & 0 \\ 0 & 0 & \varepsilon_{33} \end{bmatrix} \begin{bmatrix} E_1 \\ E_2 \\ E_3 \end{bmatrix}$$

$$\begin{bmatrix} S_1 \\ S_2 \\ S_3 \\ S_4 \\ S_5 \\ S_6 \end{bmatrix} = \begin{bmatrix} s_{11} & s_{12} & s_{13} & 0 & 0 & 0 \\ s_{21} & s_{22} & s_{23} & 0 & 0 & 0 \\ s_{31} & s_{32} & s_{33} & 0 & 0 & 0 \\ 0 & 0 & 0 & s_{44} & 0 & 0 \\ 0 & 0 & 0 & 0 & s_{55} & 0 \\ 0 & 0 & 0 & 0 & 0 & 2(s_{11} - s_{12}) \end{bmatrix} \begin{bmatrix} \sigma_1 \\ \sigma_2 \\ \sigma_3 \\ \sigma_4 \\ \sigma_5 \\ \sigma_6 \end{bmatrix} + \begin{bmatrix} 0 & 0 & d_{31} \\ 0 & 0 & d_{33} \\ 0 & 0 & d_{15} \\ d_{15} & 0 & 0 \\ 0 & 0 & 0 \end{bmatrix} \begin{bmatrix} E_1 \\ E_2 \\ E_3 \end{bmatrix}$$

Equation (19)

Therefore, due to the symmetries present in the tetragonal phase, the piezoelectric behavior of BTO is fully determined by 3 coefficients. Besides, experimental evidence for BTO shows that the piezoelectric coefficients are strongly dependent on the annealing temperature, density and grain size. Hiroshi Maiwa obtained values for  $d_{33}$  ranging from  $45\text{pC/N}$  to  $172\text{pC/N}$  for hot isostatic-pressed barium titanate (HIP-BT) with different annealing temperature; also,  $d_{31}$  and the average relative permittivity (dielectric constant)  $\varepsilon_r$  exhibited significant variation depending on processing conditions [27].

## FLEXOELECTRICITY

### 5.1. THEORETICAL OVERVIEW

Flexoelectricity is the generation of polarization density in response to applied strain gradients shown by certain materials. Unlike piezoelectricity, which is exclusive of non-centrosymmetric configurations, the flexoelectric effect may occur in centrosymmetric materials induced by symmetry breaking due to the non-uniform strain [28]. The polarization density generated due to the strain field is given by:

$$\mathbf{P}_i = \boldsymbol{\mu}_{ijkl} \frac{\partial \mathbf{S}_{jk}}{\partial x_l}$$

Equation (20)

Being  $\boldsymbol{\mu}_{ijkl}$  the matrix elements of the 4-rank flexoelectric tensor  $[\boldsymbol{\mu}]$ . Notice that for constant strain tensor  $[\mathbf{S}]$  the polarization density is null. If additionally, the material is piezoelectric and ferroelectric, the total induced polarization density will be the sum of the corresponding effects:

$$\mathbf{P}_T = \mathbf{P}_S + \varepsilon_0 [\mathbf{X}] \mathbf{E} + [\boldsymbol{\delta}] [\boldsymbol{\sigma}] + [\boldsymbol{\mu}] [\partial \mathbf{S}]$$

Equation (21)

Where  $P_S$  is the built-in or spontaneous polarization and  $[\partial S]$  represents the strain gradient tensor, not to be confused with the deformation gradient (see equation 18). Thus, equation (21) should be understood as a generalization of equation (9). Furthermore, in analogy with piezoelectricity, the *converse flexoelectric effect* is described as the coupling between an applied gradient of electric field and the induced mechanical stress [29] [30].

$$[\sigma] = [\mu^\ddagger] \partial E$$

Equation (22)

With  $[\mu^\ddagger]$  the 4-rank converse flexoelectric tensor and  $\partial E$  standing for the gradient of applied electric field. Even though  $[\mu]$  and  $[\mu^\ddagger]$  can be proven to be the same tensor, the Voigt representation of  $[\mu]$  is 3x18 while the one for  $[\mu^\ddagger]$  is 6x9, making it impossible to relate them via matrix transposition, unlike the case of the piezoelectric effect [29]. Therefore, the notation  $[\mu^\ddagger]$  indicates that the matrix representation of  $[\mu]$  needs to be rearranged in the converse flexoelectric effect.

## 5.2. FLEXOELECTRICITY IN BTO

As stated in section 5.1. above, the flexoelectric effect does not have crystallographic restrictions, allowing centrosymmetric materials to exhibit this behavior. In the case of BTO, on which the rhombohedral, orthorhombic and tetragonal phases are ferroelectric, polarization density is already existent prior to the application of curvature; however, this is not the case for the paraelectric phase where the average titanium off-centering vanishes according to the Takahasi model. Thus, an interesting candidate for studying flexoelectricity in BTO would be the high temperature cubic phase. Furthermore, Shu et al. proved that the number of non-zero independent flexoelectric coefficients for the cubic point group  $m3m$  is 3. The explicit shape of  $[\mu]$  in matrix notation is [29]:

$$[\mu] \doteq \begin{bmatrix} \mu_{11} & 0 & 0 & \mu_{11} & 0 & 0 & \mu_{14} & 0 & 0 & 0 & \mu_{14} & 0 & 0 & 0 & \mu_{111} & 0 & 0 & 0 \\ 0 & \mu_{14} & 0 & 0 & \mu_{11} & 0 & 0 & \mu_{14} & 0 & \mu_{111} & 0 & 0 & 0 & 0 & 0 & 0 & 0 & \mu_{111} \\ 0 & 0 & \mu_{14} & 0 & 0 & \mu_{14} & 0 & 0 & \mu_{11} & 0 & 0 & 0 & \mu_{111} & 0 & 0 & 0 & \mu_{111} & 0 \end{bmatrix}$$

Equation (23)

Where the coefficient notation by Shu et al. is being used. Regarding experimental studies, Ma et al. found values for the  $\mu_{12}$  coefficient ranging from  $5\mu C/m$  in the orthorhombic phase to about  $50\mu C/m$  near the tetragonal-cubic phase transition, displaying a non-linear increasing behavior with temperature. Additionally, the coefficient was sensitive to phase symmetry, microstructure and chemical makeup [31]. Moreover, Shu et al. measured converse flexoelectric coefficients for other perovskite-like structures showing good agreement with theoretical predictions [30].

## COMPUTATIONAL PROCEDURES

This section describes MD simulations of BTO aiming to obtain its phase diagram as a function of pressure and temperature, determine its piezoelectric coefficients and examine its electric behavior (flexoelectric and paraelectric) by means of hysteresis cycles. These studies, characterized by the implementation of periodic boundary conditions, settled the basis to achieve higher levels of simulation complexity, involving the release of boundary conditions and the application of surface modifications required for testing flexoelectricity in BTO. The first part of this section describes the basics of the open source software employed to carry out the MD simulations including the custom-made tool designed to analyze the MD output. The second describes the design and flow chart of each one of the simulations reported in this thesis.

### RUNNING A SIMULATION IN LAMMPS

#### 1.1. INTRODUCTION TO LAMMPS

The Large/scale Atomic/Molecular Massively Parallel Simulator (LAMMPS) is an open source classical molecular dynamics code developed by Sandia National Laboratories from the US Department of Energy. The code has been distributed and employed since the early 2000's covering a wide range of applications in solid-state materials, soft matter and coarse-grained or mesoscopic systems [32] [33]. LAMMPS is written in C++ and designed for allowing easy modification, it natively runs in Linux although pre-built executables are available for other platforms. The code supports a vast amount of interaction potentials, statistical ensembles, integrators, numerical methods, miscellaneous pre/post processing tools and computing algorithms that makes it extremely robust and versatile; moreover, the software is fully documented, supported and updated continuously.

LAMMPS can run on a single processor or in parallel by following instructions from an *input script* that is written employing a *specific syntax* and which contains all the information embedded in the flow chart of the MD simulation (see figure 2). To enhance computational efficiency LAMMPS does not run through a graphical user interface (GUI); also, visualization and analysis of the MD simulations need to be done by means of external methods which may require custom software developing. LAMMPS *output* consist in several types of data such as thermodynamic information, text dump files of particle coordinates, velocities and other per-particle quantities, etc. (see section 1.4. of this chapter).

#### 1.2. SUPERCELL DEFINITION FOR BTO

The number, mass, charge, type and initial coordinates of the particles forming the system are read from a text file specified in the LAMMPS *input script*. In the case of crystals like BTO, the set of all particle coordinates defines a so-called *supercell* made of  $X \times Y \times Z$  unit cells. In BTO each cell consists of 10 particles from counting the cores and shells of the 5 atoms in the basis (see section 2.1. of the literature review).

Thus, the total number of particles in a simulation is  $10 \times X \times Y \times Z$  meanwhile the total number of atoms corresponds to the half of this figure. To avoid the accumulation of residual stress which may lead to simulation instability, it is recommended to set the initial separation between the atoms according to the experimental lattice parameters at the working temperature. In this thesis the initial atom separation has been set according to the lattice parameters found by Boddu et al. by means of MD simulations of BTO [22]. Furthermore, the initial separation between the core and shell of atoms have been randomly distributed and spatially oriented.

The mass of the titanium, oxygen and barium atoms can be consulted elsewhere in the literature<sup>9</sup>; on the other hand, the mass of the shells was defined to be exactly 2 a.u. so that the shell motion could be treated dynamically<sup>10</sup> [23] [34]. A custom tool called *BTO\_generator* programmed in MATLAB® R2018a (Academic License) was designed to generate the file containing the number, mass, charge, type and initial coordinates of the particles for a user defined BTO supercell with dimensions XYZ.

Additionally, the tool allows for supercell pre-visualization (see figure 7) and supports other capabilities including surface modifications in a specific dimension and the generation of indexing files for phonon dispersion studies. The *BTO\_generator* source files as well as all other custom-made software can be found in the electronic database attached to this thesis (see appendix A).

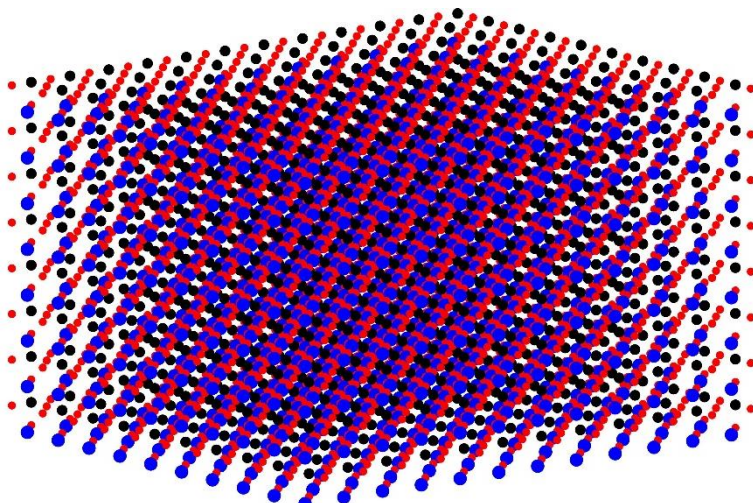


*Figure 7 - 12x10x8 BTO supercell built with *BTO\_generator*. Titanium atoms are represented in black, oxygen atoms in red and barium atoms in blue. Each atom consists of a slightly separated core and shell.*

---

<sup>9</sup> The mass of barium is nearly three times the one of titanium and the mass of titanium is nearly three times that of oxygen. This is consistent with polarization being induced due to titanium off-centering relative to the oxygen octahedra, while the heavier barium atoms remain fixed.

<sup>10</sup> The mass of the core is then the mass of the atom reduced by 2 a.u.

---

### 1.3. SIMULATION SCRIPTS

The standard LAMMPS *input script* employed in this investigation is shown below. Although certain variations and additions can be made depending on the specific simulation, the physical models and flow chart structure will remain unchanged (see figure 2).

```
# Input Script LAMMPS
# ----- INITIALIZATION -----
units          metal
dimension      3
boundary       p p p
atom_style    full
# ----- ATOMS DEFINITION -----
fix csinfo all property/atom i_CSID
read_data BTO_50x10x10.txt fix csinfo NULL CS-Info
change_box all triclinic
neighbor 2.0 bin
comm_modify vel yes
# ----- FORCE FIELDS -----
pair_style born/coul/wolf/cs 0.25 9.0 11.0
#           A        rho      sigma     C        D
pair_coeff * *  0.0      1.000   0.00     0.00    0.00
pair_coeff 4 5  7149.8110 0.3019  0.00     0.0000  0.00  #Ba-0
pair_coeff 5 6  7220.2700 0.2303  0.00     0.0000  0.00  #Ti-0
pair_coeff 5 5  3719.6000 0.3408  0.00     597.1700 0.00  #O-0
bond_style class2
#           R0      K2        K3        K4
bond_coeff 1   0.0    149.2550  0.0000   0.0000  #Ba  core-shell
bond_coeff 2   0.0    18.4650   0.0000  208.3333  #O  core-shell
bond_coeff 3   0.0    153.0700  0.0000  20.8333  #Ti  core-shell
special_bonds coul 0.0 0.0 0.0
# ----- GROUP DEFINITION -----
group cores type 1 2 3
group shells type 4 5 6
# ----- INITIAL VELOCITIES -----
thermo_style custom step etotal temp press vol
compute CSequ all temp/cs cores shells
thermo_modify temp CSequ
velocity all create 150 983629 dist gaussian mom yes rot no bias yes temp CSequ
velocity all scale 150 temp CSequ
# ----- THERMALIZATION -----
fix 1 all npt temp 300 300 0.04 tri 1.0 1.0 0.04
fix_modify 1 temp CSequ
thermo 500
dump D1 all atom 1000 dumps/stab1_*.txt
timestep 0.0004
run 100000
unfix 1
undump D1
# ----- ELECTRIC FIELD -----
variable myT equal "(step-100000) / 1000.0"
variable PyAmp python myPy
python myPy input 1 v_myT return v_PyAmp format ff file funcs.py
fix ELF all efield 0.0 0.0 v_PyAmp
fix 2 all npt temp 300 300 0.04 tri 1.0 1.0 0.04
fix_modify 2 temp CSequ
timestep 0.0004
thermo 50
dump D2 all atom 10000 dumps/stab2_*.txt
run 100000
```

In the following, every section of the *input script* will be itemized. For that purpose, is pointed out that in LAMMPS syntax any string of characters following the # symbol is a comment.

#### ▪ Initialization

```
units          metal
dimension      3
boundary       p p p
atom_style     full                                     # p=periodic
```

In this section, the units of measurement used in the simulation, the dimensionality of the system and the boundary conditions on every dimension are assigned. The set of units of measurement for the selected style `metal` can be consulted in [35].

#### ▪ Atoms definition

```
fix csinfo all property/atom i_CSID
read_data BTO_50x10x10.txt fix csinfo NULL CS-Info           # BTO_50x10x10.txt is read
change_box all triclinic
neighbor 2.0 bin
comm_modify vel yes
```

The text file built with *BTO\_generator*, containing the number, mass, type and initial coordinates of the particles forming the system is read by LAMMPS. Also, the core and shell of every atom are linked via `csinfo` (a series of tags also contained in the text file). In addition, the periodic boundary conditions are switched to `triclinic` meaning that the supercell is free to assume any possible geometry within the most general Bravais crystal system<sup>11</sup>. More emphasis regarding the triclinic system will be made in section 1.4. of this chapter where LAMMPS *output* is described.

#### ▪ Force fields

```
pair_style born/coul/wolf/cs 0.25 9.0 11.0
#
#          A          rho        sigma    C          D
pair_coeff * *   0.0        1.000     0.00    0.00    0.00
pair_coeff 4 5   7149.8110   0.3019    0.00    0.0000   0.00    #Ba-0
pair_coeff 5 6   7220.2700   0.2303    0.00    0.0000   0.00    #Ti-0
pair_coeff 5 5   3719.6000   0.3408    0.00    597.1700   0.00    #O-0
bond_style class2
#
#          R0        K2 / 2      K3        K4 / 24
bond_coeff 1     0.0        149.2550   0.0000    0.0000   #Ba    core-shell
bond_coeff 2     0.0        18.4650    0.0000   208.3333   #O    core-shell
bond_coeff 3     0.0        153.0700   0.0000   20.8333   #Ti    core-shell

special_bonds coul 0.0 0.0 0.0      # Coulomb potential inactive between an atom core-shell
```

In this part of the code, the core-shell model is invoked and defined by means of the coefficients for the Buckingham and anharmonic isotropic spring potential fitted from *ab initio* calculations (see section 3.4. of the *literature review*). Besides, the coulomb interaction is activated according to the particle charges previously read from the text file.

---

<sup>11</sup> Indeed, any crystal system is a subset of the triclinic system.

The spring constants  $k_2$  and  $k_4$  have been renormalized to fit LAMMPS conventions; moreover, the introduction of the Buckingham potential is done via the more general Born potential for the case when the fitting parameters  $\sigma$  and  $D$  are set to zero (compare with equation 11):

$$\phi^B(r) = Ae^{\frac{\sigma-r}{\rho}} - \frac{C}{r^6} + \frac{D}{r^8}$$

Equation (24)

#### ▪ Group definition

```
group cores type 1 2 3
group shells type 4 5 6
```

During the simulation is possible to define and track any subset of the total particles to implement specific calculations or methods; for example, fixing some particles movement, calculating the temperature of a certain group, apply a local electric field, etc. In this case, the particles are grouped into cores and shells to perform special thermodynamic calculations needed during the initial velocity assignment.

#### ▪ Initial velocities

```
thermo_style custom step etotal temp press vol      # Thermodynamic information format
compute CSequ all temp/cs cores shells          # Special method for cores and shells
thermo_modify temp CSequ
velocity all create 150 983629 dist gaussian mom yes rot no bias yes temp CSequ
velocity all scale 150 temp CSequ
```

The thermodynamic information is formatted to output the simulation step, total energy of the system, temperature, pressure and volume (see section 1.4. below). Also, the initial velocities for the particles are assigned according to a selected gaussian distribution to produce the requested temperature of 150K shown in this example.

#### ▪ Thermalization

```
fix 1 all npt temp 300 300 0.04 tri 1.0 1.0 0.04 # NPT ensemble with T=300K and P=0.1MPa
fix_modify 1 temp CSequ
thermo 500          # Display thermodynamic information every 500 steps
dump D1 all atom 1000 dumps/stab1_*.txt        # Output coordinates every 1000 steps
timestep 0.0004      # Timestep of integration is 0.4fs
run 100000          # Simulation will run for 100000 steps = 40ps
unfix 1             # Integrator is deactivated
undump D1
```

In this section, the thermalization of the supercell is done with respect to the control parameters introduced by a thermodynamic ensemble. Thermalization can be defined as the process in which the system reaches thermal equilibrium by means of the interaction of its constituents. In molecular dynamics the standard route to thermalization is to couple the system to a fictitious thermostat, barostat, etc. and to analyze the relaxation of the whole system (original one plus thermostat, barostat, etc.) to a stationary state [36].

This idea was introduced previously in this thesis within the concept of statistical ensemble (see section 1.3. of the *literature review*). Although the control degrees of freedom introduced by the ensemble (temperature, pressure, etc.) are targeted through the dynamical equations, it will take a certain number of steps for the system to achieve those values as measured directly from the particles position and momentum (see definitions, equations D.4 and D.5). The number of simulation steps on which the system achieves thermodynamic equilibrium depends on the system itself, the target values of thermodynamic parameters, the application of external fields and constraints, etc.

Additionally, it may occur that even if the thermodynamic parameters have achieved its target value, the system of particles exhibits collective phenomena such as slightly damped oscillations. Although these mechanical responses might vanish after a certain number of steps, there exist computational techniques (like the introduction of viscosity parameters) which may aid the system in achieving its energy minimization.

In the example code above an npt ensemble has been chosen for a target temperature and pressure of 300K and 0.1MPa, respectively. Besides, a damping parameter of 0.4 has been introduced to reduce fluctuations in temperature and pressure (which might generate collective mechanical oscillations and longer thermalization). In the next lines the output frequency of thermodynamic information and particle coordinates is established, a timestep value is set and a total number of simulation steps is entered.

At the end of the simulation stage the current integrator is deactivated; however, LAMMPS allows to define a new simulation flow chart which considers the previous simulation last step as its initial conditions. Hence several simulation stages can be linked, so that for any new simulation stage, the initial velocities are taken from the end of the previous flow chart instead of being assigned via Maxwell-Boltzmann or Gaussian distributions (see figure 2).

#### ▪ Electric field

```
variable myT equal "(step-100000) / 1000.0"      # Define the input variable for funcs.py
variable PyAmp python myPy
python myPy input 1 v_myT return v_PyAmp format ff file funcs.py # Compute electric field
fix ELF all efield 0.0 0.0 v_PyAmp           # Add the electric field in the z direction
fix 2 all npt temp 300 300 0.04 tri 1.0 1.0 0.04
fix_modify 2 temp CSequ
timestep 0.0004
thermo 50
dump D2 all atom 10000 dumps/stab2_.txt
run 100000
```

Supposing the thermalization of the supercell have been achieved in the previous steps, spontaneous polarization might have been generated depending on the working temperature of the BTO simulation. In any case, the application of external electric fields allows to study the electric and converse piezoelectric behavior of the system: Hysteresis cycles can be performed by means of cyclically applied electric fields while constant fields can be used to induce strain, for example.

The script section above is analogous to the one for thermalization, except for the act of defining and adding an externally applied electric field to the integrator. As stated at the end of section 1.3. of the *literature review*, the force due to the electric field is added as a constant in the dynamical equations; thus, allowing the field to be time dependent along the simulation<sup>12</sup>. The explicit form of the electric field is introduced as a *Python* function script `funcs.py` which reads the current timestep `myT` and outputs a value for the field. The field is then defined to point in the z-direction and is included in the previously detailed integrator. A typical example of `func.py` is shown below for the case of a linearly decreasing electric field. The field magnitude is given assigned units of MV/m by the variable `v` while the timestep is input from variable `T`.

```
def myPy(T):
    if T<10.0:
        v = 0.005
    elif T<20.0:
        v = 0.005 - 0.005*(T-10)/10.0
    else:
        v = 0.0
    return v;
```

## 1.4. OUTPUT

Although a vast amount of simulation data can be output by LAMMPS including thermodynamic information, running information, special computations output and so forth, the most fundamental data consists in the set of all particle coordinates for a specific simulation step. The particle coordinates can be saved with a user defined frequency into text dump files called *dumps* which possess a specific structure defined by LAMMPS and need to be post-processed for simulation analysis and visualization.

Every *dump* contains a header: which includes crucial simulation information such as timestep and supercell geometry, and a body: listing the particle coordinates along with one or more particle identifiers. The first few lines of a standard *dump* obtained in this thesis are shown below with the body and header signalized.

```
ITEM: TIMESTEP
72000
ITEM: NUMBER OF ATOMS
10000
ITEM: BOX BOUNDS xy xz yz pp pp pp
4.442653097167617e-02 3.9976027815564976e+01 2.4326261328940928e-02
-2.1299117413470015e-02 4.0238924297747850e+01 -1.8719106673849343e-03
-2.6881464142245903e-01 4.0266814641420979e+01 3.7625180333556052e-02
ITEM: ATOMS id type xs ys zs
2007 2 0.248538 0.0466704 0.0042565
4007 2 0.446725 0.0469513 0.00372935
5222 4 0.496839 0.197362 0.203847
1101 1 0.0995465 0.099229 0.00234421
1201 1 0.0977765 0.199999 0.00302279
3007 2 0.348538 0.0496547 0.0051362
```

<sup>12</sup> A constant force can be simply added to the potential gradient every timestep.

The supercell geometry defined in the header (highlighted in yellow above) is given in the following format (see section 6.12. in [37]):

$$\begin{array}{lll} x_{lo\_bound} & x_{hi\_bound} & xy \\ y_{lo\_bound} & y_{hi\_bound} & xz \\ z_{lo\_bound} & z_{hi\_bound} & yz \end{array}$$

Such that a fictional orthogonal bounding box encloses the triclinic supercell with tilt factors  $xy$ ,  $xz$  and  $yz$ , defined as the amount of displacement applied to the faces of an originally orthogonal supercell to transform it into a general parallelepiped. The dimensions of the orthogonal bounding box and the originally orthogonal supercell are given by, respectively:

$$\begin{aligned} l_{x\_bound} &= x_{hi\_bound} - x_{lo\_bound} \\ l_{y\_bound} &= y_{hi\_bound} - y_{lo\_bound} \\ l_{z\_bound} &= z_{hi\_bound} - z_{lo\_bound} \end{aligned}$$

Equation (25)

$$\begin{aligned} l_x &= x_{hi} - x_{lo} \\ l_y &= y_{hi} - y_{lo} \\ l_z &= z_{hi} - z_{lo} \end{aligned}$$

Equation (26)

With the parameters  $x_{hi}$ ,  $x_{lo}$ ,  $y_{hi}$ ,  $y_{lo}$ ,  $z_{hi}$  and  $z_{lo}$  related to the orthogonal bounding box via:

$$\begin{aligned} x_{lo\_bound} &= x_{lo} + \min(0, xy, xz, xy + xz) \\ x_{hi\_bound} &= x_{hi} + \max(0, xy, xz, xy + xz) \\ y_{lo\_bound} &= y_{lo} + \min(0, yz) \\ y_{hi\_bound} &= y_{hi} + \min(0, yz) \\ z_{lo\_bound} &= z_{lo} \\ z_{hi\_bound} &= z_{hi} \end{aligned}$$

Equation (27)

Finally, the relation between the dimensions of the originally orthogonal supercell that underwent tilting and the conventional triclinic system description (in terms of lattice vectors  $\mathbf{a}$ ,  $\mathbf{b}$ ,  $\mathbf{c}$  and angles  $\alpha$ ,  $\beta$  and  $\gamma$ ) is given according to the transformation:

$$\begin{aligned} \mathbf{a} &= [l_x \quad 0 \quad 0] \\ \mathbf{b} &= [xy \quad l_y \quad 0] \\ \mathbf{c} &= [xz \quad yz \quad l_z] \end{aligned}$$

Equation (28)

Expressed in cartesian coordinates; thus, the following relations hold:

$$\begin{aligned} a &= l_x \\ b^2 &= l_y^2 + xy^2 \\ c^2 &= l_z^2 + xz^2 + yz^2 \\ \cos \alpha &= \frac{(xy * xz + l_y * yz)}{b * c} \\ \cos \beta &= \frac{xz}{c} \\ \cos \gamma &= \frac{xy}{b} \end{aligned}$$

Equation (29)

Regarding the *dump*'s body, a single particle output has been highlighted in turquoise above with data formatted as follows:

Number	Type	x	y	z
--------	------	---	---	---

The *Number* and *Type* of the particle are invariant throughout the whole simulation after being defined by *BTO\_generator*, that is, they are the particle tags or identifiers allowing to track the simulation under any post-processing computation. Meanwhile *Number* runs from 1 to the total number of particles  $N$ , *Type* takes values from 1 to 6 tagging atom species (barium, titanium, oxygen) and core-shell attribute. Furthermore, the particle coordinates are displayed in *adimensional normalized crystal units* with the physical dimensions of the supercell being bounded within 0 and 1; thus, the coordinates need to be rescaled according to the *dump*'s header information: this process is easily achievable by referring to the coordinates transformation matrix induced by equation 28:

$$\mathbf{T} = \begin{bmatrix} l_x & xy & xz \\ 0 & l_y & yz \\ 0 & 0 & l_z \end{bmatrix}$$

Equation (30)

Which acts on the left of column arrays of unscaled coordinates. Indeed, the supercell corner coordinates [1 1 1] are mapped into the triclinic parallelepiped corner  $\mathbf{a} + \mathbf{b} + \mathbf{c}$  with components  $[l_x + xy + xz \ l_y + yz \ l_z]$ .

The thermodynamic information of a simulation, unlike particles coordinates, is not dumped into indexed text files; instead, it is updated in an accumulative simulation report known as a *log file* which also outputs processed instructions, computation statistics and errors. The specific thermodynamic parameters and the frequency at which those are displayed can be user defined (see section 1.3. of this chapter). Some few lines displaying thermodynamic information are shown below for a LAMMPS *log file*.

```

Memory usage per processor = 16.1413 Mbytes
Step TotEng E_coul E_bond Temp Press Volume
    0   -3237491.1   -3472734.2    2364.791   1.0015433   -51730.202   1713521.8
   10   -3240905.2   -3492182.4    3354.9425   3.9709005   -13820.265   1695498.7
   20   -3240650.1   -3491370.5    3600.9256   10.881901   -15894.579   1693920.9
   30   -3239674.6   -3491913.6    4528.919    20.321744   -16223.153   1694234.8
   40   -3240372.6   -3493542.5    4261.049    26.130498   -13847.734   1697401
   50   -3239597.1   -3491442.6    2442.7743   27.828149   -11292.292   1695858.6
   60   -3240503     -3497957    5551.7846   24.845218   -9384.2342   1697260.7
   70   -3239679.8   -3497545.9    5924.7242   21.572163   -9707.2559   1695629.6

```

In this case, total energy, coulomb interaction energy, bonding energy, temperature, pressure and volume are being updated every 10 steps.

## CUSTOM GRAPHICAL USER INTERFACE

### 2.1. OVERVIEW

After the simulation ends, the *dump* files together with the thermodynamic information and other per-particle data needs to be processed to meet specific computation goals. Also, there exists a relatively broad catalog of post-processing tools supported by LAMMPS, none of them provides the level of versatility and full computational resources needed in this thesis; thereby, the custom tool called *BTO\_Visuals* programmed in MATLAB® R2018a (Academic License) was designed to aid the simulation analysis required in this work.

*BTO\_Visuals* can be defined as a post-processing LAMMPS graphical user interface exclusively suited for barium titanate, but whose capabilities may be easily generalized for other crystalline materials. The tool has been developed since December 2016 as a collaboration between the author of this thesis and Dr. Jan Ocenasek and its supported capabilities up to the latest debugged version (14 June 2018) are the following:

- Global and local supercell selective visualization
- Triclinic lattice parameters evolution
- Global and local polarization computing
- Stereographic polarization visuals
- Polarization clustering visuals
- Polarization histograms
- Polarization evolution and hysteresis cycle analysis
- Global strain tensor measurements
- Phonon dispersion analysis (post-processed from LAMMPS)

Furthermore, some features currently under development include:

- Core-shell phonon dispersion analysis
- Local strain tensor measurements

In the next section, the algorithms behind two of the most important listed capabilities will be detailed. A screen shot of the *BTO\_Visuals* GUI is shown in figure 8.

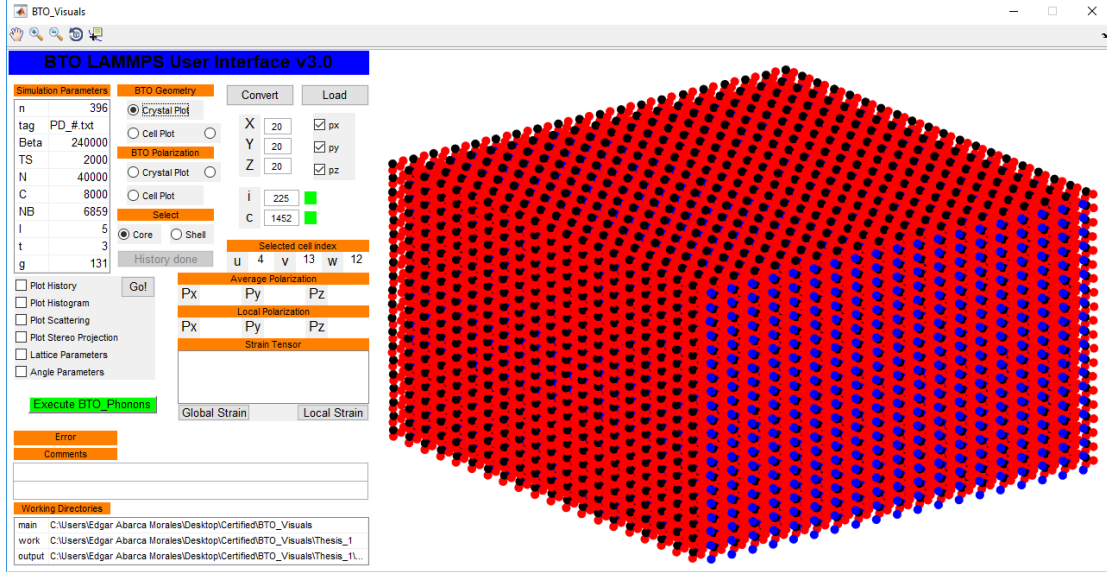


*Figure 8 – The BTO\_Visuals GUI allows for several calculations regarding electric and mechanical behavior of barium titanate supercells. The BTO\_Visuals source files can be found in the electronic database attached with this thesis (see appendix A).*

## 2.2. STEREOGRAPHIC PROJECTION

Stereographic projection represents a powerful visualization tool for simultaneously analyzing the polarization of every unit cell in the supercell. Mathematically, it can be defined as a mapping between the unitary sphere and a 2D plane such that every point in the sphere except for one is represented by a unique non-divergent point in the plane. The special point is called the *pole* and the mapping is built so that the line joining the pole with any other point of the sphere pierces a specific location in the 2D plane [38].

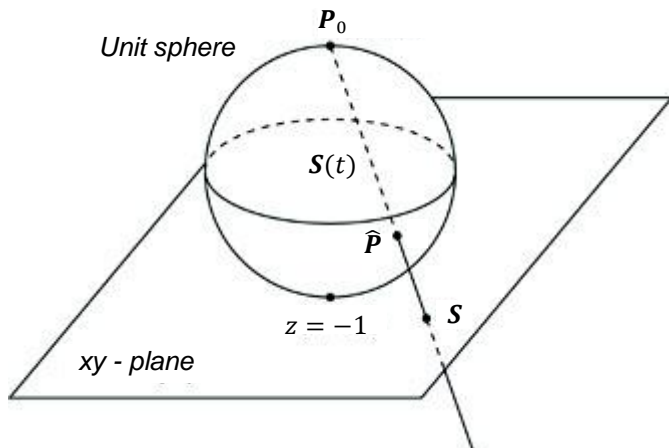


*Figure 9 – The stereographic projection with respect to the pole  $P_0 = [0 \ 0 \ 1]$ . The unit sphere is mapped into the xy - plane by means of building the line  $S(t)$ .*

Figure taken and adapted from [38].

For simplicity, considering the unitary sphere centered at the origin and the plane  $z = -1$  (see figure 9), the equation of the line joining a chosen pole  $\mathbf{P}_0 = [0 \ 0 \ 1]$  with an arbitrary point  $\hat{\mathbf{P}} = [\hat{P}_x \ \hat{P}_y \ \hat{P}_z]$  in the sphere is given by:

$$\mathbf{S}(t) = \mathbf{P}_0 + (\hat{\mathbf{P}} - \mathbf{P}_0)t$$

Equation (31)

With the parameter  $t \in \mathbb{R}$ ; thus, in the intersection  $\mathbf{S} = [x \ y \ -1]$  between the line and the plane  $z = -1$  the following equations hold:

$$t = \frac{-2}{\hat{P}_z - 1}$$

$$[x \ y] = \begin{bmatrix} -2\hat{P}_x & -2\hat{P}_y \\ \hat{P}_z - 1 & \hat{P}_z - 1 \end{bmatrix}$$

Equation (32)

The last one defining the so-called  $z$  stereographic projection. It should be noticed that the mapping is divergent in the pole  $\mathbf{P}_0$  and that the following inequalities are satisfied:

$$\hat{P}_z > 0 \Rightarrow |[x \ y]| > 2$$

$$\hat{P}_z < 0 \Rightarrow |[x \ y]| < 2$$

Equation (33)

Besides  $|[x \ y]| = 2$  in  $P_z = 0$ ; therefore, the inequalities make a distinction between the north and south hemispheres of the unit sphere, respectively. The stereographic projection here derived will be applied to the unitary polarization density  $\hat{\mathbf{P}} = |\mathbf{P}|^{-1}\mathbf{P}$  (see equation 7) while the magnitude  $|\mathbf{P}|$  of the vectors will be considered in generating colored stereographic plots representing the spatial distribution of the polarization density within the whole BTO supercell. An example plot is shown in figure 10 below.

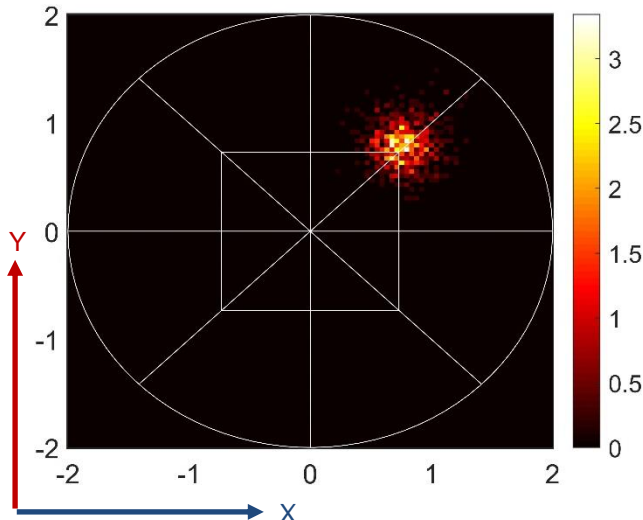


*Figure 10 – Colormap generated from the southern hemisphere of the  $z$  stereographic projection for a  $10 \times 10 \times 10$  BTO supercell at 100K. The brighter color represents zones of higher accumulated polarization magnitude in units of  $C/m^2$ . Polarization density is distributed towards the  $[1 \ 1 \bar{1}]$  direction. The corners of the centered square represent the set of four possible  $\langle 1 \ 1 \ 1 \rangle$  directions within the hemisphere bounded by the circumference  $|[x \ y]| < 2$ .*

### 2.3. GLOBAL STRAIN TENSOR MEASUREMENTS

Equation (17) can be employed to calculate the global strain tensor  $[S]$  from a triclinic supercell configuration  $A$  to a triclinic supercell configuration  $B$ . Supposing the existence of a constant deformation gradient  $[F]$  by neglecting possible local strain gradients  $[\partial S]$  and solving equation (18) via straightforward integration yields:

$$x = [F]X$$

Equation (34)

Which is a linear map between the old coordinates  $X$ 's and the new coordinates  $x$ 's. Thereby, the old triclinic basis  $[a \ b \ c]$  must be mapped into the new triclinic basis  $[a' \ b' \ c']$ . Using equation (27) for expressing the triclinic lattice vectors and identifying the result with equation (30) gives:

$$[F] \doteq \begin{bmatrix} l'_x & xy' & xz' \\ 0 & l'_y & yz' \\ 0 & 0 & l'_z \end{bmatrix} \begin{bmatrix} l_x & xy & xz \\ 0 & l_y & yz \\ 0 & 0 & l_z \end{bmatrix}^{-1} = T'T^{-1}$$

Equation (35)

This expression can be directly plugged into equation (17) after reading the supercell geometry parameters from the corresponding *dump* file headers.

## DETAILED OBJECTIVES OF THE INVESTIGATION

### 3.1. OVERVIEW

In this section, the main simulations of BTO carried out in this thesis are described by indicating its specific objective and by showing its design parameters. Every simulation is tagged with a name to keep track of it along this document and in the attached electronic database (see appendix A). For the sake of clarity, the simulations referred in the *future work* section of the *results and discussion* chapter will not be detailed here.

### 3.2. THE SIMULATIONS

- ⊕ Reference\_100, Reference\_220 & Reference\_300

Objective: To study the spontaneous polarization of BTO in the three ferroelectric phases (rhombohedral, orthorhombic and tetragonal) at constant temperatures of 100K, 220K and 300K, respectively. Also, estimate the thermalization time of the BTO supercell in each case <sup>13</sup>.

<sup>13</sup> Knowing the thermalization times is essential for developing any further stable simulation; furthermore, it allows for computing time saving.

Design parameters:

<b>Stages</b>	1
<b>Supercell</b>	10x10x10
<b>Boundary conditions</b>	Periodic
<b>Initial velocities</b> <b>temperature</b>	100K, 220K, 300K, resp.
<b>Statistical ensemble</b>	NPT
<b>Temperature</b>	100K, 220K, 300K, resp.
<b>Pressure</b>	0.1MPa (atmospheric)
<b>Electric field</b>	No
<b>Timestep</b>	0.4 fs
<b>Steps</b>	500,000 (200ps)

✚ *Induced\_Thermalization*

Objective: Induce supercell thermalization at low temperatures via temporary electric field application. This thermalization procedure will be used to obtain the BTO phase diagram.

Design parameters:

<b>Stages</b>	1
<b>Supercell</b>	10x10x10
<b>Boundary conditions</b>	Periodic
<b>Initial velocities</b> <b>temperature</b>	1K
<b>Statistical ensemble</b>	NPT
<b>Temperature</b>	10K
<b>Pressure</b>	0.1MPa (atmospheric)
<b>Electric field</b>	Yes
<b>Electric field function (per component)</b>	50MV/m during 125,000 steps + linear decrease from 50MV/m to 0MV/m in 125,000 steps + 0MV/m during 250,000 steps.
<b>Electric field direction</b>	[1 1 1]
<b>Timestep</b>	0.4 fs
<b>Steps</b>	500,000 (200ps)

✚ *Phase\_Diagram\_0, Phase\_Diagram\_2, Phase\_Diagram\_4 & Phase\_Diagram\_6*

Objective: To obtain the phase diagram of BTO for temperatures between 10K and 400K. Hydrostatic pressures of 0.1MPa, 2GPa, 4GPa and 6GPa will be selected, respectively. This set of simulations will provide the lattice parameters and polarization evolution. The thermalization stage will follow the procedure described in the *Induced\_Thermalization* simulation. Temperature is slowly modified to achieve a quasi-static behavior in the thermostat.

Design parameters:

<b>Stages</b>	2
<b>Supercell</b>	10x10x10
<b>Boundary conditions</b>	Periodic
<b>Initial velocities</b>	
<b>temperature</b>	1K
<b>Statistical ensemble</b>	NPT
<b>Stage 1</b>	
<b>Temperature</b>	10K
<b>Pressure</b>	0.1MPa, 2GPa, 4GPa, 6GPa, resp.
<b>Electric field</b>	Yes
<b>Electric field function (per component)</b>	50MV/m during 100,000 steps + linear decrease from 50MV/m to 0MV/m in 100,000 steps.
<b>Electric field direction</b>	[1 1 1]
<b>Timestep</b>	0.4 fs
<b>Steps</b>	200,000 (80ps)
<b>Stage 2</b>	
<b>Temperature</b>	10K – 400K
<b>Pressure</b>	0.1MPa, 2GPa, 4GPa, 6GPa, resp.
<b>Electric Field</b>	No
<b>Timestep</b>	0.4fs
<b>Steps</b>	2,000,000 (800ps)

### Piezoelectric\_300

Objective: To determine the  $d_{31}$ ,  $d_{32}$  and  $d_{33}$  piezoelectric coefficients for the tetragonal BTO phase (see equation 19). The converse piezoelectric effect will be induced by means of a relatively strong electric field.

Design parameters:

<b>Stages</b>	1
<b>Supercell</b>	30x30x30
<b>Boundary conditions</b>	Periodic
<b>Initial velocities</b>	
<b>temperature</b>	300K
<b>Statistical ensemble</b>	NPT
<b>Temperature</b>	300K
<b>Pressure</b>	0.1MPa (atmospheric)
<b>Electric field</b>	Yes
<b>Electric field function</b>	250MV/m during 50,000 steps + linear decrease from 250MV/m to 0MV/m in 25,000 steps + 0MV/m during 25,000 steps.
<b>Electric field direction</b>	[0 0 1]
<b>Timestep</b>	0.4 fs
<b>Steps</b>	100,000 (40ps)

■ *Hysteresis\_100, Hysteresis\_220, Hysteresis\_300 & Hysteresis\_400*

Objective: To study the electric behavior of BTO in the three ferroelectric phases (rhombohedral, orthorhombic and tetragonal) and in the paraelectric phase (cubic) at constant temperatures of 100K, 220K, 300K and 400K respectively. This study shall provide the electric susceptibility coefficients of the distinct BTO phases (see equation 10); moreover, the linearity of the model given by equation (9) can be further analyzed.

Design parameters:

<b>Stages</b>	2
<b>Supercell</b>	10x10x10
<b>Boundary conditions</b>	Periodic
<b>Initial velocities</b> <b>temperature</b>	100K, 220K, 300K, 400K, resp.
<b>Statistical ensemble</b>	NPT
<b>Stage 1</b>	
<b>Temperature</b>	100K, 220K, 300K, 400K, resp.
<b>Pressure</b>	0.1MPa
<b>Electric field</b>	Yes (except in cubic case)
<b>Electric field function</b> <b>(per component)</b>	50MV/m during 100,000 steps + linear decrease from 50MV/m to 0MV/m in 100,000 steps.
<b>Electric field direction</b>	[1 1 1], [1 1 0], [0 0 1], [0 0 1], resp.
<b>Timestep</b>	0.4 fs
<b>Steps</b>	200,000 (80ps)
<b>Stage 2</b>	
<b>Temperature</b>	100K, 220K, 300K, 400K, resp.
<b>Pressure</b>	0.1MPa
<b>Electric Field</b>	Yes
<b>Electric field function</b> <b>(in magnitude)</b>	Sinusoidal cycle with amplitudes of 120MV/m, 75MV/m, 50MV/m, 100MV/m, resp. and period of 2,000,000 steps.
<b>Electric field direction</b>	[1 1 1], [1 1 0], [0 0 1], [0 0 1], resp.
<b>Timestep</b>	0.4fs
<b>Steps</b>	2,500,000 (1ns)

The LAMMPS *input scripts*, initial coordinates files, electric field scripts, *log files*, *dumps* and *shell launcher* files<sup>14</sup> for all the simulations can be consulted in the attached electronic database (see appendix A).

---

<sup>14</sup> Technical script employed to gather the simulation input documents, run the simulation and redirect the output from/to specific directories within the supercomputing cluster.

## RESULTS AND DISCUSSION

In this chapter, the MD simulations outlined in section 3.2. of the *computational procedures section* are thoroughly described and analyzed. Ongoing work regarding flexoelectricity and supercell vibrations in BTO is discussed by means of some preliminary results and simulation methods obtained/developed within the research group.

### PHASE DIAGRAM OF BTO

#### 1.1. SPONTANEOUS POLARIZATION

The polarization history (polarization versus time plots) from simulations Reference\_100, Reference\_220 and Reference\_300 are shown in figures 11 to 13, respectively. In all cases, a stationary state of spontaneous polarization is achieved after some iteration steps, where the time for developing stable spontaneous polarization considerably increases at cryogenic temperatures. Times of 20ps, 9ps and 112ps are required at 300K, 220K and 100K, respectively. Hence, due to nonlinear correlation, times possibly much higher than 112ps would be necessary to induce stable spontaneous polarization at 10K. Indeed, times up to 160ps have been measured in achieving stationary polarization of  $10 \times 10 \times 10$  supercells at 100K for simulations not reported in this thesis; thus, finding stationary spontaneous polarization states at less than 100K is computationally inefficient and electric-field-induced polarization is used instead (see section 1.2. of this chapter). Overall, these simulations show that the employed model reproduces the ferroelectric behavior of BTO.

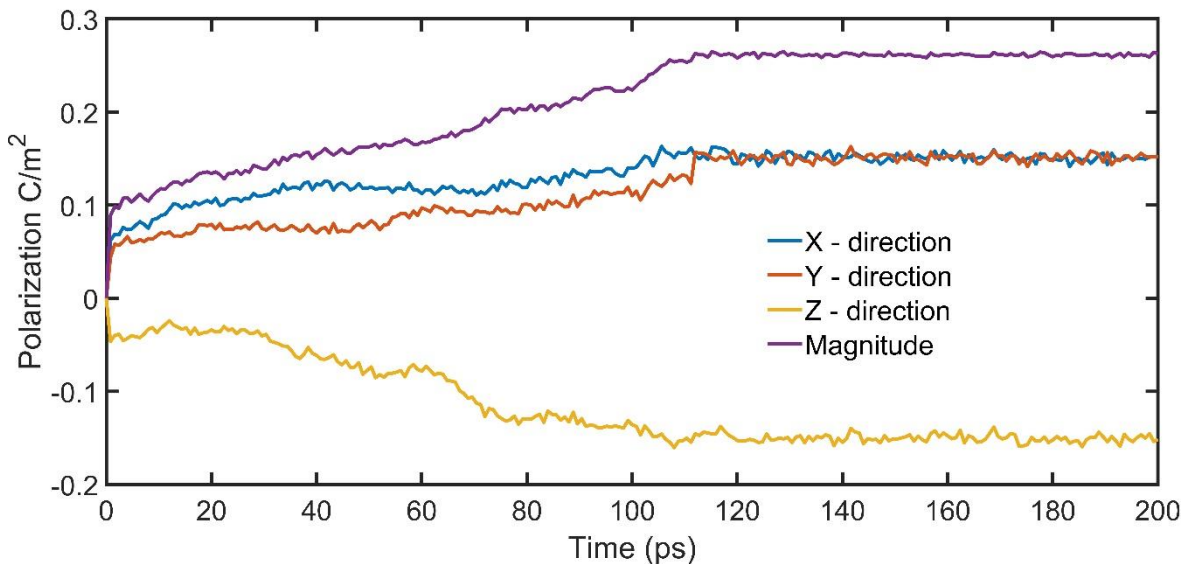
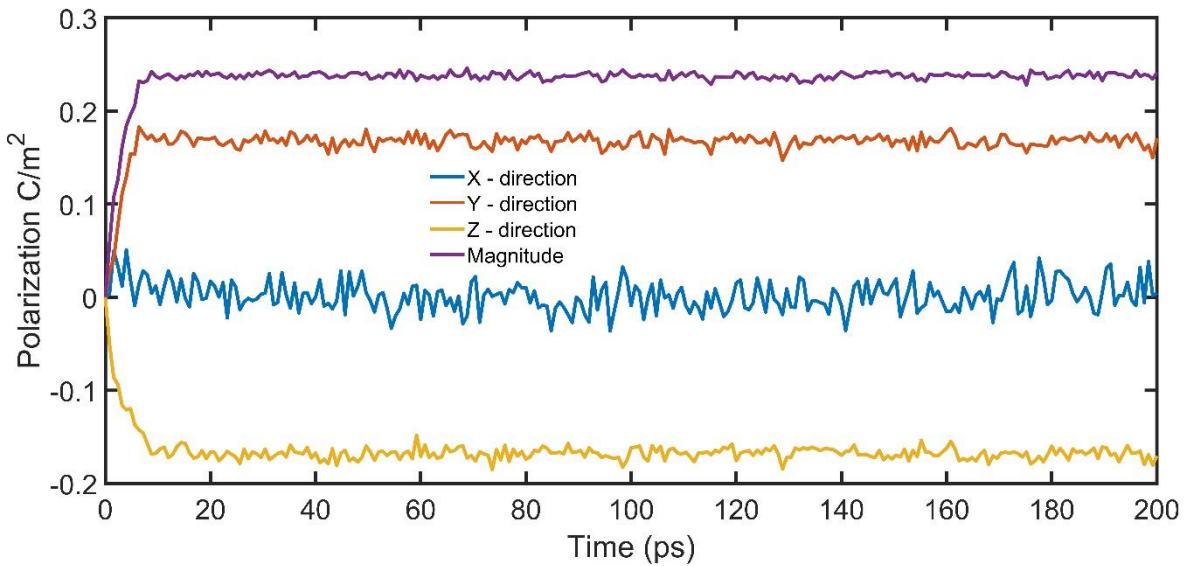
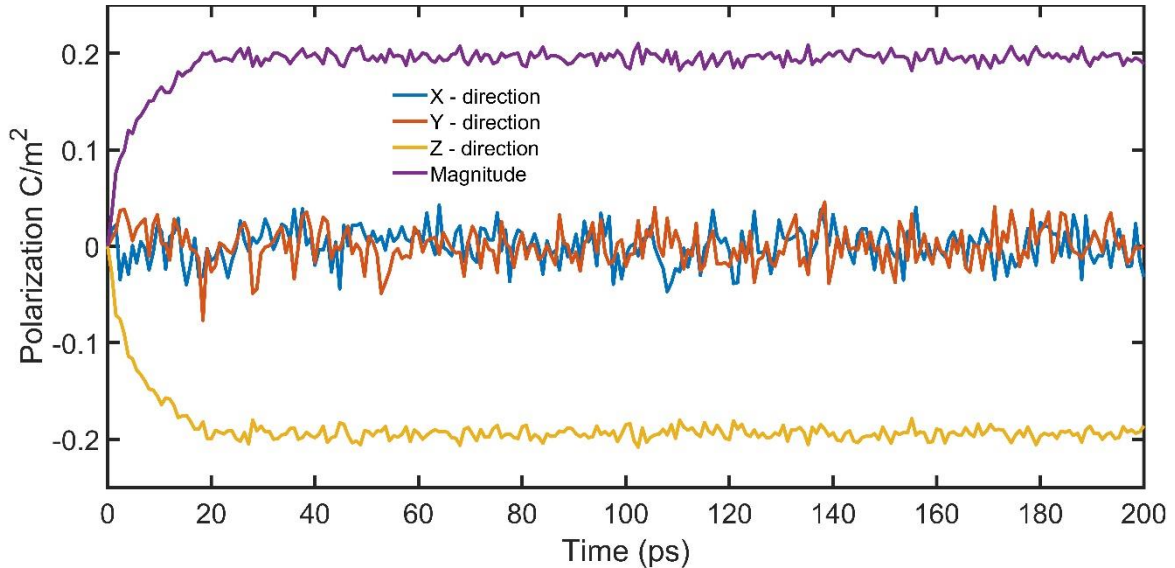


Figure 11 – Average polarization versus time for a  $10 \times 10 \times 10$  supercell of BTO at 100K. A state of stationary polarization is spontaneously achieved after 112ps. The average polarization points toward the [1 1 -1] direction with magnitude of  $0.26\text{C}/\text{m}^2$ .



*Figure 12 – Average polarization versus time for a 10x10x10 supercell of BTO at 220K. A state of stationary polarization is spontaneously achieved after 9ps. The average polarization points toward the [0 1 -1] direction with magnitude of 0.24C/m<sup>2</sup>.*



*Figure 13 – Average polarization versus time for a 10x10x10 supercell of BTO at 300K. A state of stationary polarization is spontaneously achieved after 20ps. The average polarization points toward the [0 0 -1] direction with magnitude of 0.19C/m<sup>2</sup>.*

Furthermore, the magnitude of the polarization slightly decreases with temperature, showing a higher decrease from 220K to 300K than from 100K to 220K. Also, simulation instabilities due to the thermostat and barostat equilibration are displayed in the figures as random noise.

## 1.2. CORRELATION WITH THE TAKAHASI MODEL

Polarization stereographic colormaps taken for the first (0ps) and for the last (200ps) step of the *Reference\_100*, *Reference\_220* and *Reference\_300* simulations are shown in figures 14 to 16, respectively. In the three figures an initial randomly distributed polarization tends to spontaneously increase in magnitude and configurate along the  $\langle 1\ 1\ 1 \rangle$  directions as stated by Takahasi (see section 2.4. of the *literature review*). For every figure, the first row of images is taken at 0ps and the second at 200ps while the first column shows the south hemisphere and the second the north hemisphere of the stereographic projection (see section 2.2. of the *computational procedures* section). Polarization is given in units of C/m<sup>2</sup>.

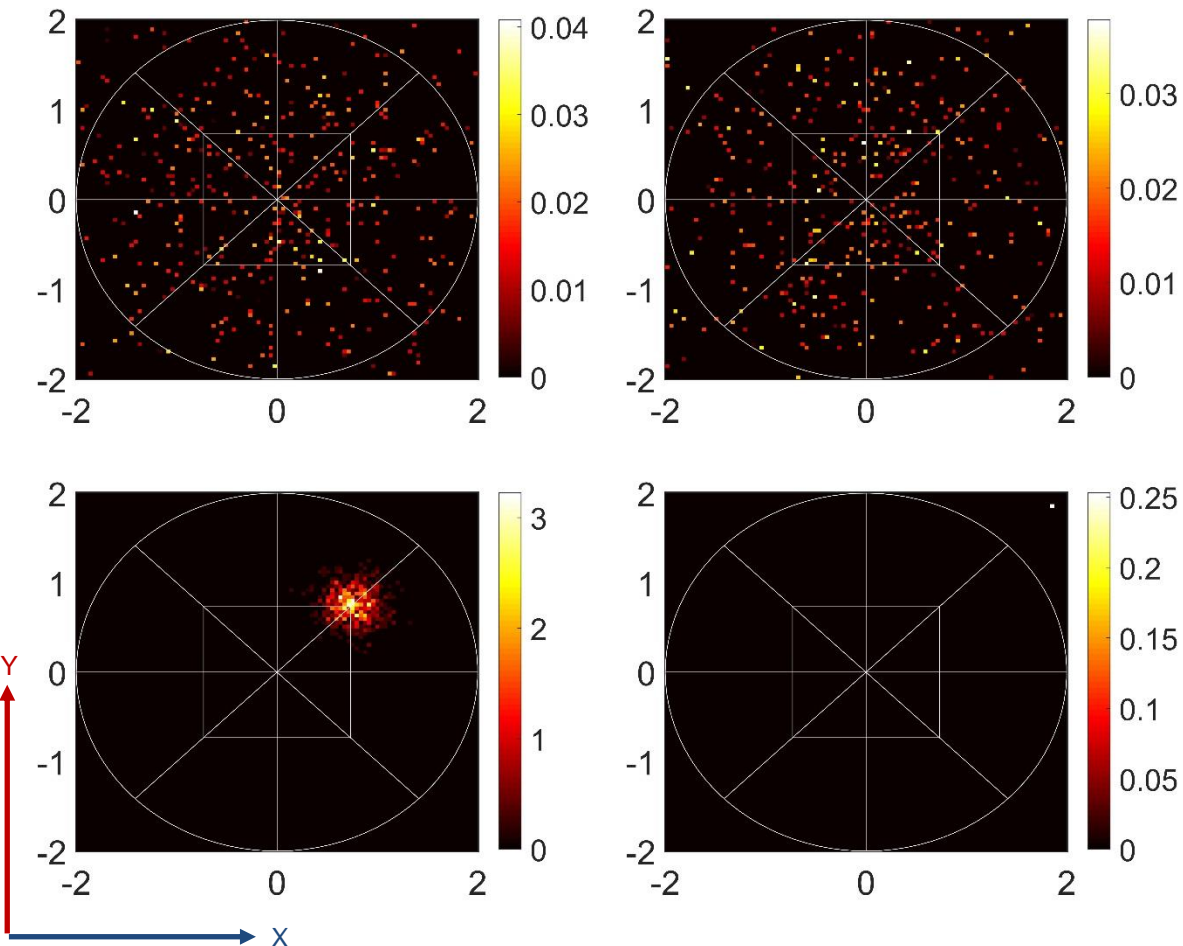


*Figure 14* – Polarization stereographic colormap for a 10x10x10 supercell of BTO at 100K. Up: Polarization density distribution prior to the simulation. Down: Polarization density is spontaneously generated and distributed towards the  $[1\ 1\ -1]$  direction (compare with figure 11).

In figure 14, the polarization density of each unit cell ends up pointing nearly towards the  $[1\ 1\ -1]$  direction, leaving the northern hemisphere of the stereographic projection empty as the point in the up-right corner is out of bounds (belongs to the south hemisphere).

This is consistent with the Takahasi model and the rhombohedral symmetry of the lowest temperature ferroelectric BTO phase (see section 1.4. of this chapter). At this point it should be noticed that the  $\langle 1\ 1\ 1 \rangle$  directions in the stereographic projection does not coincide exactly with the  $\langle 1\ 1\ 1 \rangle$  direction in the supercell except for the cubic case. This is because the stereographic projection was built in cartesian coordinates; however, the geometrical variations from the cubic phase introduced by the ferroelectric phases are at any cost negligible and thus a pseudo-cubic approach is justified (see figure 5).

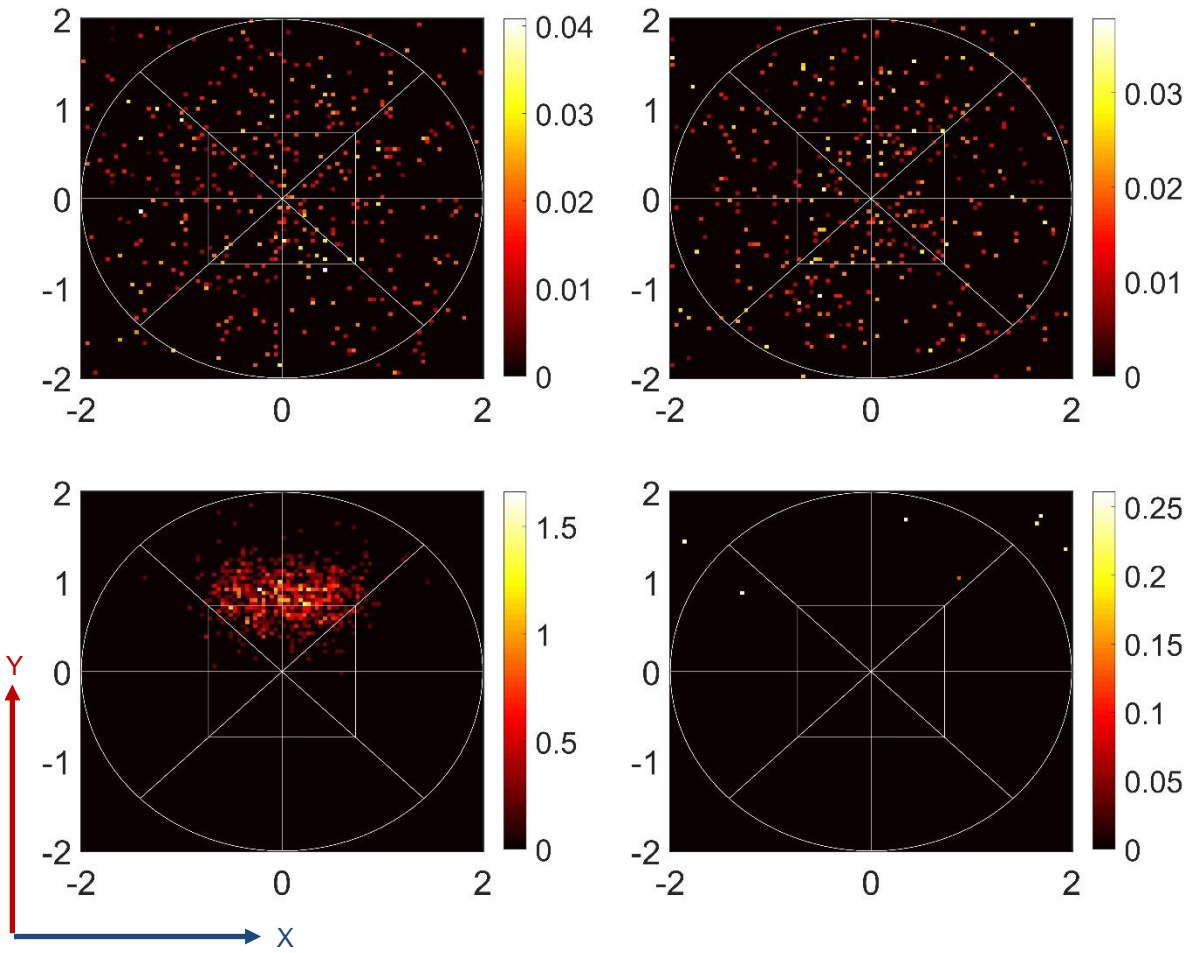


*Figure 15* – Polarization stereographic colormap for a  $10 \times 10 \times 10$  supercell of BTO at 220K. *Up*: Polarization density distribution prior to the simulation. *Down*: Polarization density is spontaneously generated and distributed within the  $[-X\ Y\ -Z]$  and  $[X\ Y\ -Z]$  quadrants (compare with figure 12).

In figure 15, the polarization density equitably distributes between the  $[-X\ Y\ -Z]$  and the  $[X\ Y\ -Z]$  quadrants, thus cancelling the x-component of the average polarization in figure 12. This is again consistent with the Takahasi model where the orthorhombic symmetry of the medium temperature ferroelectric BTO phase is explained as the result of combining local rhombohedral structures (see section 1.4. of this chapter). However, the polarization density becomes scattered among the line joining the expected  $\langle 1\ 1\ 1 \rangle$  directions rather than pointing towards them.

Additional experiments not reported in this thesis show that the directionality towards the expected  $[-1 \ 1 \ -1]$  and  $[1 \ 1 \ -1]$  directions is enhanced with the application of an externally applied electric field (see section 1.3. of this chapter). This means that the scattering may be caused due to insufficient equilibration time of the polarization; nevertheless, the relatively high temperature of 220K might require impractical computing times for achieving better polarization directionality. Moreover, figure 15 shows a non-empty north hemisphere for the stereographic projection measured at 200ps. Although the north hemisphere is scarcely populated, being non-empty indicates that local instabilities can be present regardless the level of thermal activity.

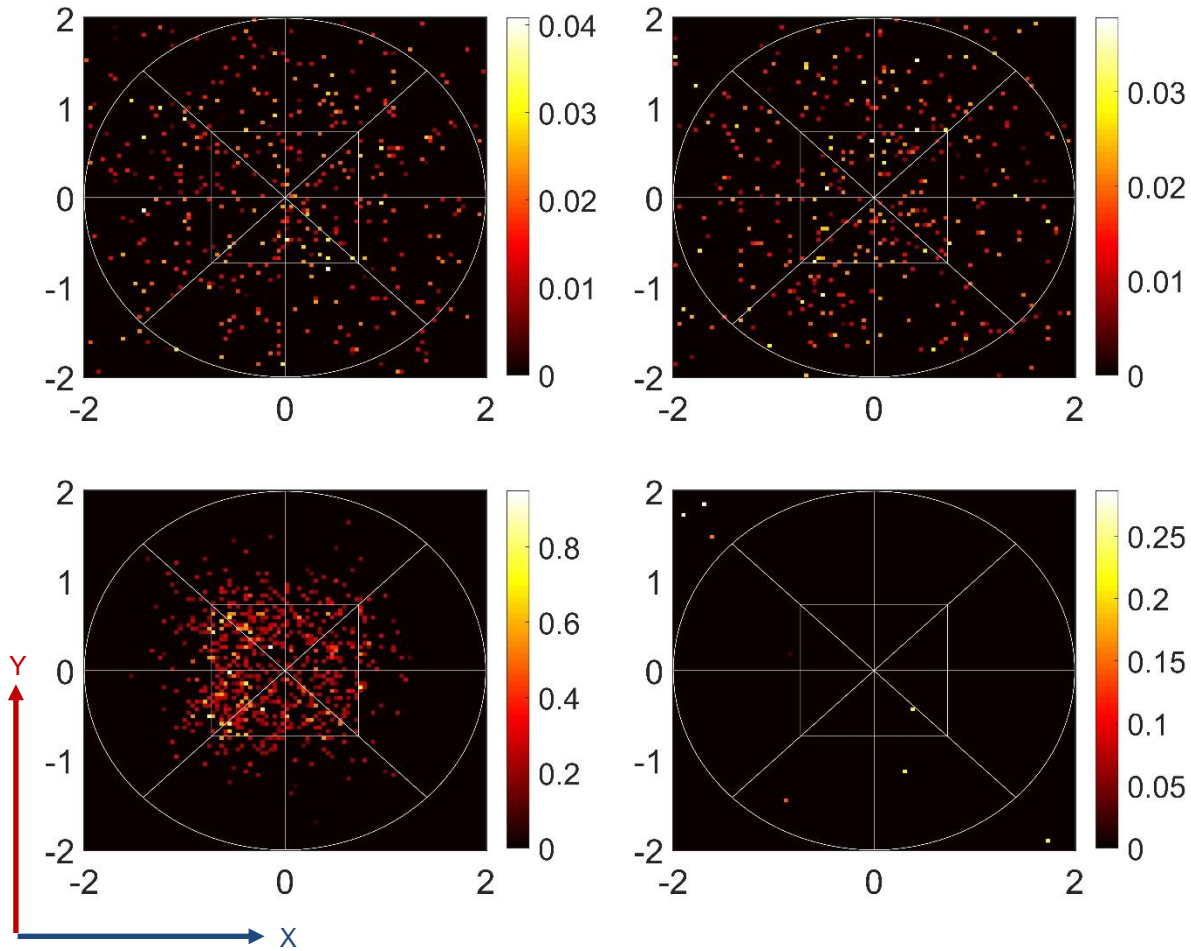


*Figure 16* – Polarization stereographic colormap for a  $10 \times 10 \times 10$  supercell of BTO at 300K. *Up*: Polarization density distribution prior to the simulation. *Down*: Polarization density is spontaneously generated and distributed within the  $[-X \ Y \ -Z]$ ,  $[X \ Y \ -Z]$ ,  $[-X \ -Y \ -Z]$  and  $[X \ -Y \ -Z]$  quadrants (compare with figure 13).

Finally, in figure 16 the polarization density equitably distributes between the  $[-X \ Y \ -Z]$ ,  $[X \ Y \ -Z]$ ,  $[-X \ -Y \ -Z]$  and  $[X \ -Y \ -Z]$  quadrants, thus cancelling the x-component and y-component of the average polarization in figure 13. Although the Takahashi model consistently holds for explaining the tetragonal symmetry of the high temperature paraelectric BTO phase (see section 1.4. of this chapter), considerable

amount of scattering is observed among the expected  $\langle 1\ 1\ 1 \rangle$  directions due to the higher thermal activity at 300K. Furthermore, as in the case for 220K, local instabilities are present in the north hemisphere. The study of the cubic paraelectric phase of BTO in terms of the Takahashi model will be done in section 1.5. of this chapter.

### 1.3. INDUCED THERMALIZATION

As stated in the previous section, it takes time for the spontaneous polarization to appear and stabilize towards the  $\langle 1\ 1\ 1 \rangle$  direction described by the Takahashi model; hence, the electric-field-induced thermalization approach tested in the *Induced\_Thermalization* simulation has been used to build the TP diagram of BTO. The polarization history of this simulation is showed in figure 17 while the polarization stereographic colormap taken at the last step (200ps) is displayed in figure 18.

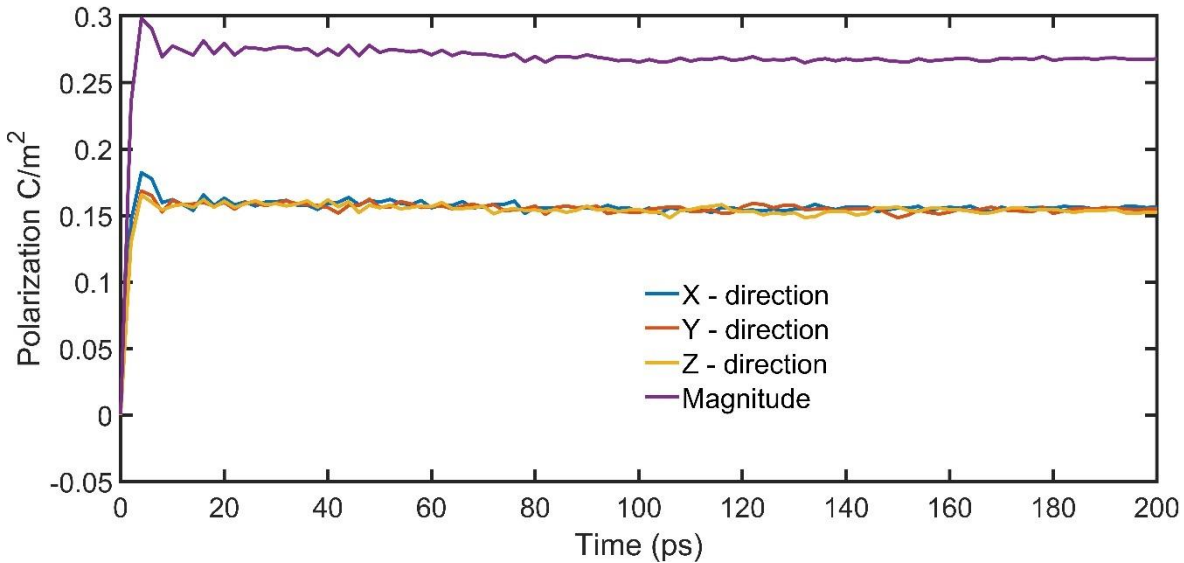
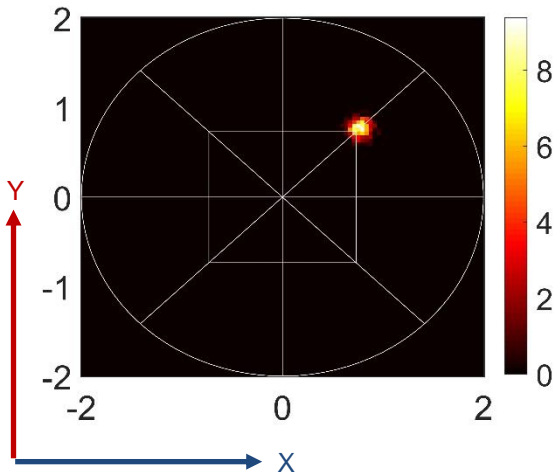


Figure 17 – Average polarization versus time for a 10x10x10 supercell of BTO at 10K. A state of stationary polarization is achieved after 8ps by means of an externally applied electric field of 50MV/m (per component) in the  $[1\ 1\ 1]$  direction during the first 50ps of the simulation. The field is then linearly released during 50ps. The average polarization in the absence of applied field points toward the  $[1\ 1\ 1]$  direction with magnitude of  $0.27\text{C}/\text{m}^2$ .

In figure 17 a stationary polarization state at 10K is achieved in nearly 8ps compared to the 112ps that it takes for the 10x10x10 supercell at 100K. Moreover, when the externally applied electric field is completely released (100ps) a remnant state of polarization is maintained with a magnitude of  $0.27\text{C}/\text{m}^2$ . This value is slightly higher than the  $0.26\text{C}/\text{m}^2$  found for the same ferroelectric phase at 100K (see figure 11). Furthermore, the magnitude peaks up to  $30\text{C}/\text{m}^2$  at 4ps of simulation but then it relaxes to nearly  $0.27\text{C}/\text{m}^2$ , meaning that the applied electric field is enough to induce polarization but not to overcome the value of spontaneous polarization given from the ferroelectric nature of the rhombohedral phase.

Additionally, figure 18 shows considerably less scattering in polarization density towards the [1 1 1] direction compared to the one for spontaneous polarization achieved at 100K (see figure 14). This result proves that the application of externally applied electric fields can favor the directionality of polarization density according to the Takahashi model; besides, computing times can be reduced using this approach during the thermalization stage of the BTO supercell (see section 1.4. of this chapter).



*Figure 18 – North hemisphere of a polarization stereographic colormap for a 10x10x10 supercell of BTO at 10K displaying remnant polarization after the application of an external electric field (compare with figure 17). The south hemisphere is not shown for being empty. The polarization density points towards the [1 1 1] direction and exhibits relatively little scattering (compare with figure 14).*

#### 1.4. TP DIAGRAM CONSTRUCTION

In comparison to the cases previously analyzed, on which no thermodynamic variable was being externally changed, temperature was slowly varied from 10K to 400K in *Phase\_Diagram\_0*, *Phase\_Diagram\_2*, *Phase\_Diagram\_4* and *Phase\_Diagram\_6* aiming to build the temperature versus pressure diagram of BTO in a state of quasi-equilibrium for pressures of 0.1MPa (atmospheric), 2GPa, 4GPa and 6GPa, respectively; however, the target temperatures set in the barostat are normally not precisely achieved and thus need to be corrected by consulting the thermodynamic information in the *log* files. With such corrections, the actual pressures employed during the simulations are nearly 0.1GPa, 1.9GPa, 3.9GPa and 5.9GPa, respectively. The evolution of triclinic lattice parameters and polarization density with temperature for each simulation is shown from figure 19 to 22. A *wavelet transform* algorithm was employed to denoise the plots from thermostat and barostat oscillations.

From the triclinic lattice parameters evolution with temperature (consisting of lattice constants  $a$ ,  $b$ ,  $c$  and angles  $\alpha$ ,  $\beta$ ,  $\gamma$ ), three phase transitions separating four BTO phases can be observed for the different pressures employed. As the phases are inferred from the supercell geometry defined by the set of triclinic scale parameters (see section 1.4. in the *computational procedures* chapter), this study accounts for the global geometry of the supercell regardless the existence of local structures. Thus, it is possible to build a phase diagram of BTO comparable to the one obtained for the bulk material. From the figures, the lowest temperature phase is defined by  $a = b = c$  and  $\alpha = \beta = \gamma \neq 90^\circ$ , characteristic of the rhombohedral lattice system.

It is noted that the lattice constant diminishes and the angle approaches orthogonality as the pressure increases. While the former is a direct effect of the application of hydrostatic pressure, the latter might be consequence of a mechanism aiming to achieve energy minimization after the reduction of the unit cell enclosing the titanium atom.

A medium temperature phase is observed to have roughly  $a = b \neq c$  and  $\alpha = \beta = 90^\circ \neq \gamma$ , which is described by an orthorhombic crystal system with a unit cell in the shape of a right rhombic prism. As in the case for the rhombohedral symmetry, the lattice constants decrease with pressure while  $\gamma$  increases and approximates to  $90^\circ$ . The next phase is defined by both:  $a = b \neq c$  and a somewhat unstable orthogonality originated from a discontinuous increase in  $\gamma$  coming from the orthorhombic phase. Meanwhile the tetragonal supercell shrinks with the application of hydrostatic pressure, the instability in orthogonality seems to increase close to the orthorhombic-tetragonal phase transition. Finally, a higher temperature cubic geometry defined by enhanced orthogonality stability with respect to the tetragonal phase is formed, as observed in the angle parameters evolution. As expected, the cubic geometry also gets compacted with pressure.

Moreover, when increasing the pressure an expansion in temperature range for the high temperature cubic phase is observed while the temperature intervals for the rhombohedral, orthorhombic and tetragonal phases shrinks and displaces up to the point that at 5.9GPa the orthorhombic phase barely exists and the tetragonal-to-cubic phase transition have been lowered in more than 200K. Also, the orthogonality instabilities present in the orthorhombic-to-tetragonal phase transition at 5.9GPa suggest the merging of the orthorhombic and tetragonal phases at some pressure higher to 5.9GPa making it possible to conceive the existence of at least one critical point. Furthermore, phase transitions are always accompanied by average polarization density discontinuities that are consistent to the phase change according to the Takahasi model (see section 1.5 of this chapter).

The polarization density exhibits a decreasing behavior with temperature; also, the polarization reduction at the orthorhombic-to-tetragonal transition is higher than in the rhombohedral-to-orthorhombic. This is consistent with the values of average stationary spontaneous polarization obtained from figures 11 to 13, which for the rhombohedral (100K), orthorhombic (220) and tetragonal (300K) phases are  $0.26\text{C/m}^2$ ,  $0.24\text{C/m}^2$  and  $0.19\text{C/m}^2$ , respectively. Moreover, polarization decreases with pressure, meaning that the piezoelectric effect is not strong enough to overcome the reduction in spontaneous polarization.

With the phase transition temperatures obtained from figures 19 to 22 it is possible to build the TP diagram for BTO shown in figure 23. From linear extrapolation the phase boundaries converge into a pair of critical points lying approximately at 7.2GPa for 102.8K and 8.4GPa for 95.2K. The first critical point was expected from the lattice parameters evolution shown in figure 22 on which the orthorhombic phase is considerably reduced at 5.9GPa; that is, the orthorhombic phase vanishing at 7.2GPa seems entirely reasonable. Furthermore, although the tetragonal phase is still well defined at 5.9GPa, its temperature range is also left-shifting and being reduced; thereby, it undergoes the same process as the orthorhombic phase but vanishes at the higher pressure of 8.4GPa.

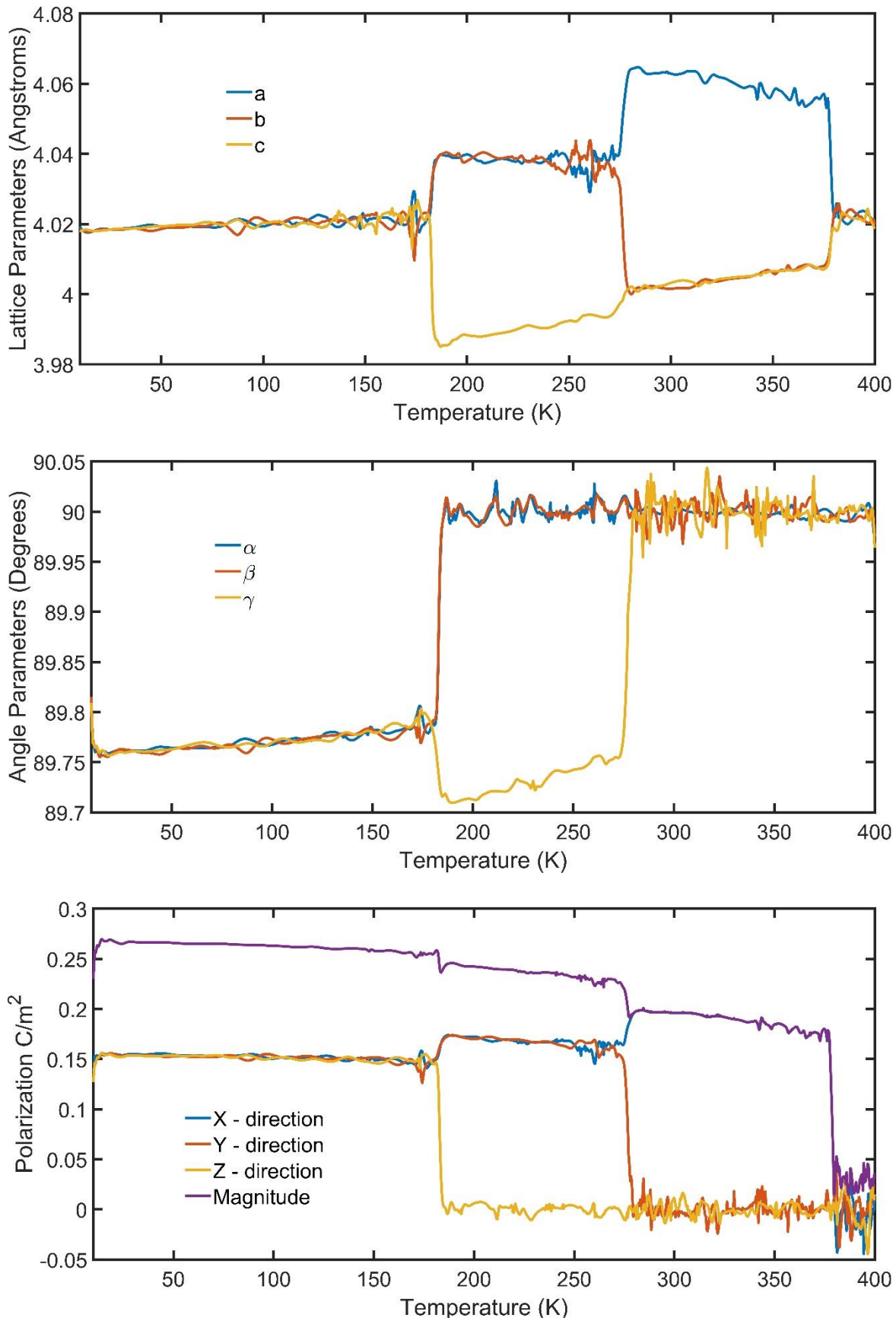


Figure 19 – Lattice parameters, angle parameters and spontaneous polarization history at 0.1GPa. 50

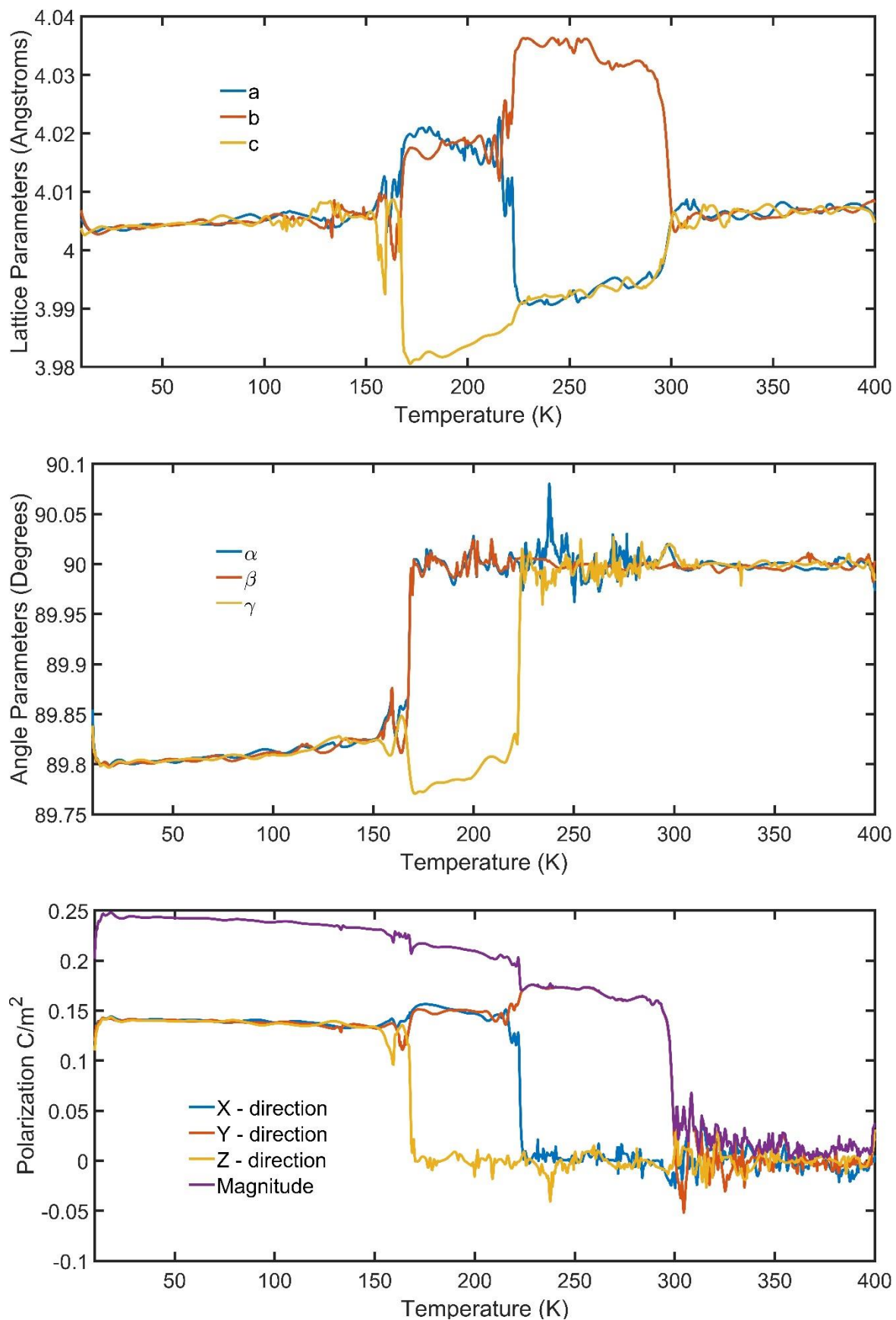


Figure 20 – Lattice parameters, angle parameters and spontaneous polarization history at 1.9GPa. 51

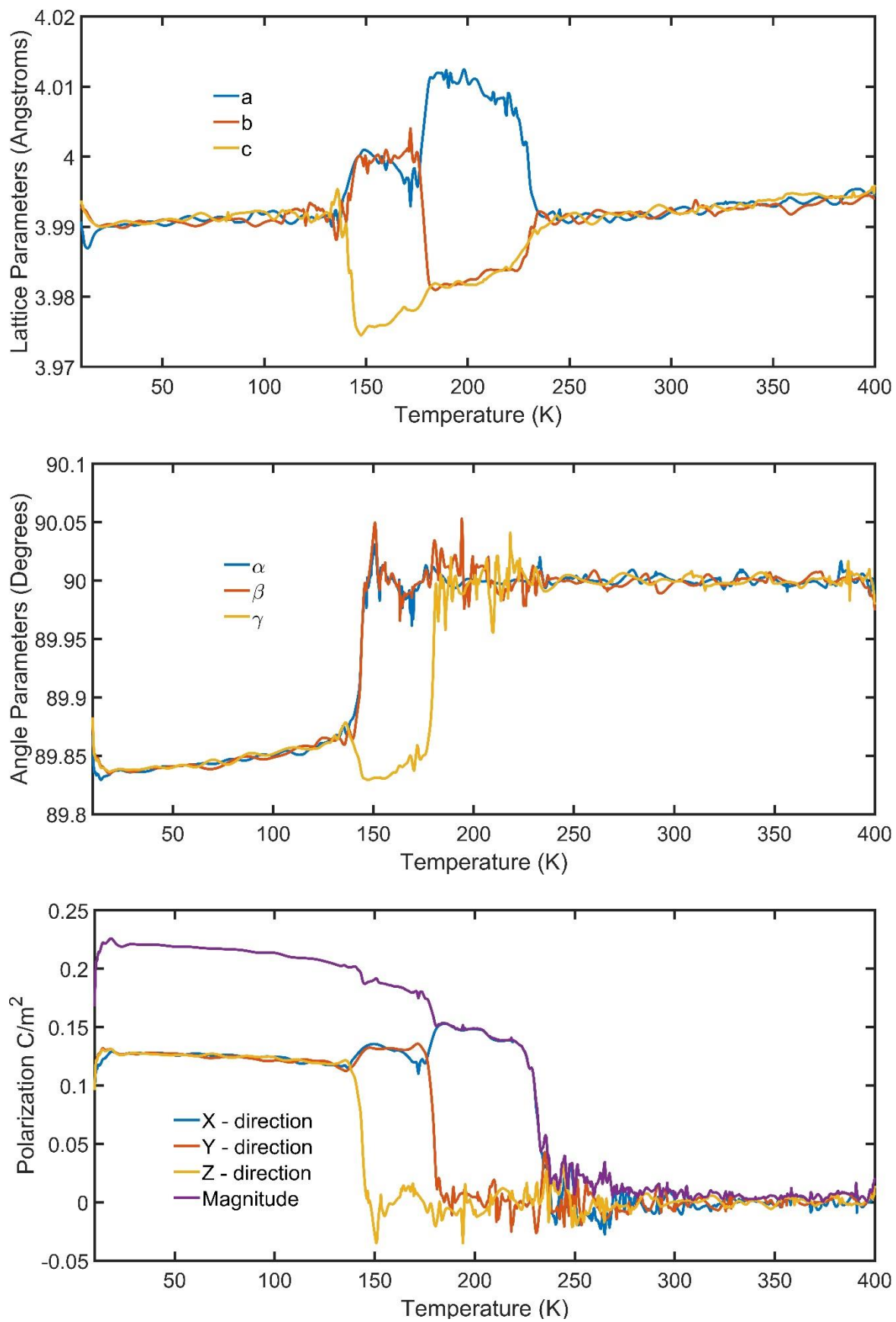


Figure 21 – Lattice parameters, angle parameters and spontaneous polarization history at 3.9GPa. 52

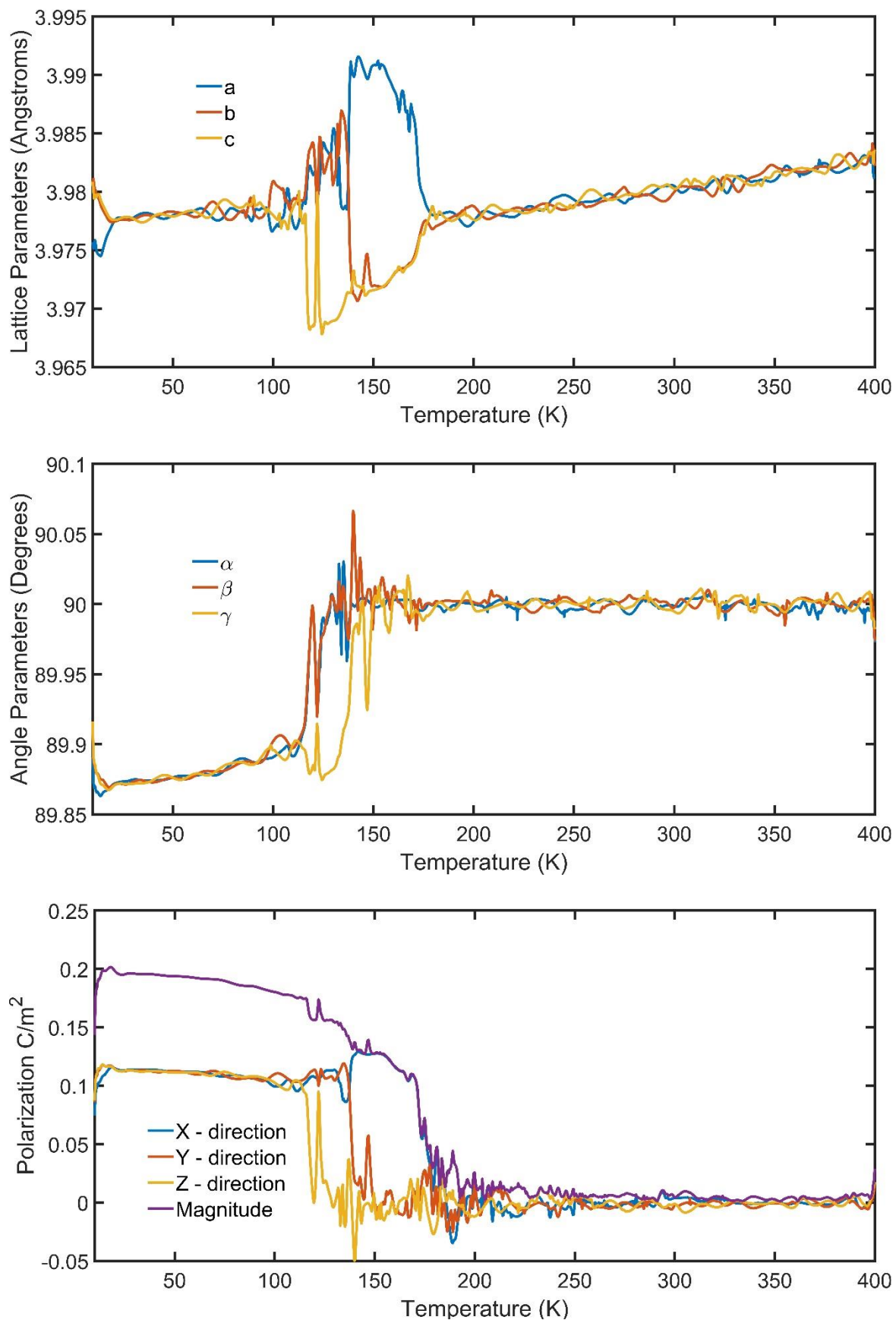
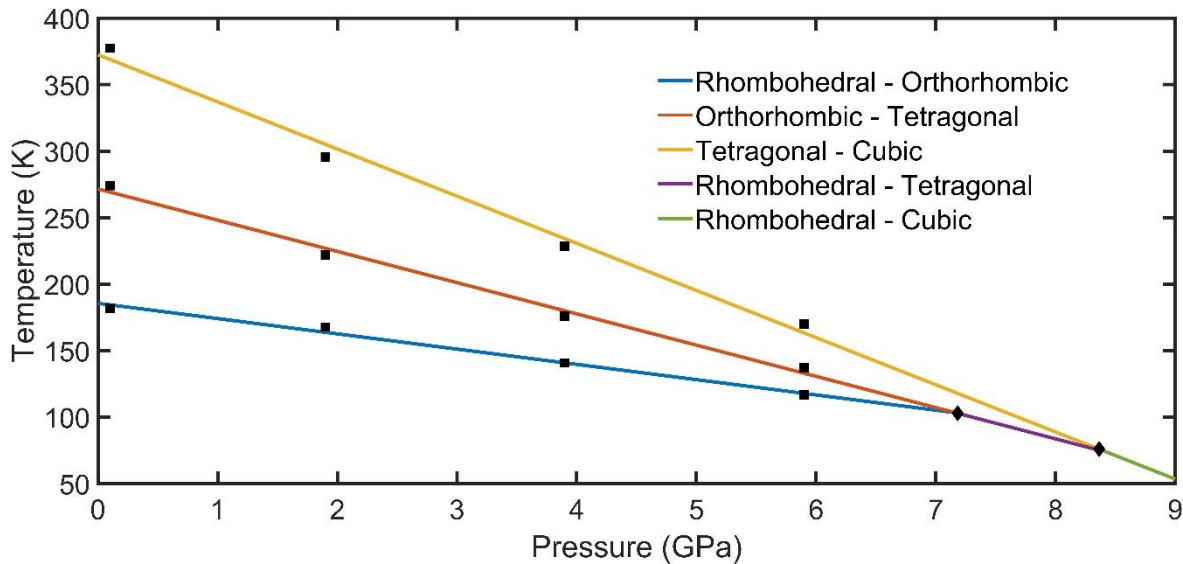


Figure 22 – Lattice parameters, angle parameters and spontaneous polarization history at 5.9GPa. 53



*Figure 23 – Temperature versus pressure phase diagram of BTO obtained from the phase transition temperatures shown in the lattice parameters evolution of figures 19 to 22. A linear fit has been employed to interpolate and extrapolate the phase boundaries. Two critical points are found at nearly 7.2GPa for 102.8K and 8.4GPa for 95.2K.*

## 1.5. POLARIZATION NEAR PHASE TRANSITIONS

In figures 24 to 26, polarization density is studied close to the three phase transitions observed for BTO at a pressure of 0.1GPa in order of increasing temperature. The polarization stereographic colormap prior and after the corresponding phase transition is shown in the upper and middle row of each figure, respectively, with the south hemisphere always plotted to the left of the north hemisphere. In the lower row of each figure the polarization density is mapped before the transition (left) and after the transition (right) for every unit cell in the  $10 \times 10 \times 10$  BTO supercell. The unit cells are represented with a spherical marker whose color indicates the cartesian quadrant at which the polarization vector belongs; thus, eight different colors are available depending on polarization directionality.

The color code is listed as follows:

▪ Indigo blue	$[X \quad Y \quad Z]$
▪ Green	$[X \quad Y \quad -Z]$
▪ Red	$[X \quad -Y \quad Z]$
▪ Ocean blue	$[X \quad -Y \quad -Z]$
▪ Ochre brown	$[-X \quad Y \quad Z]$
▪ Purple	$[-X \quad Y \quad -Z]$
▪ Orange	$[-X \quad -Y \quad Z]$
▪ Black	$[-X \quad -Y \quad -Z]$

### Rhombohedral to Orthorhombic phase transition

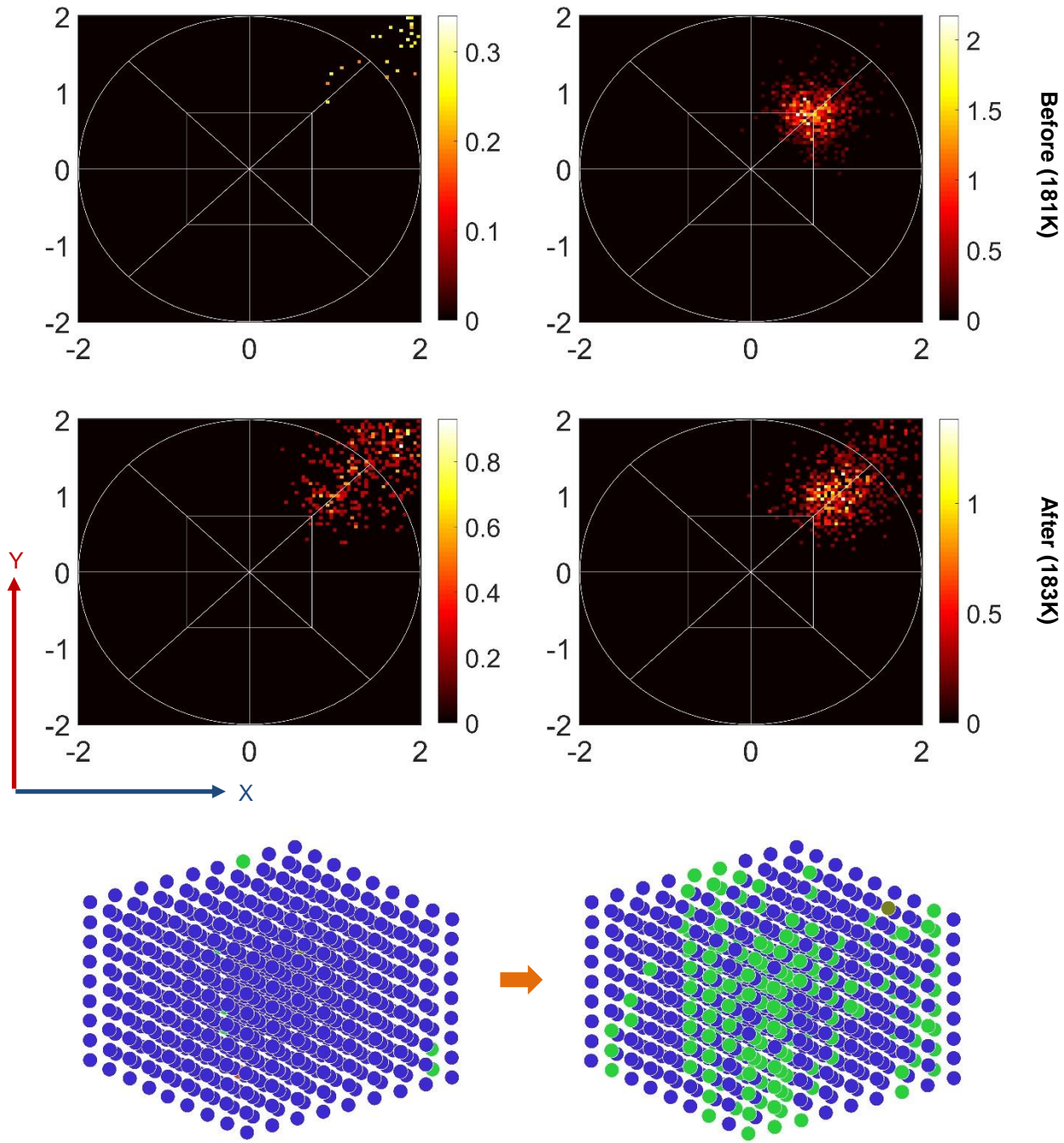


*Figure 24 –* Polarization stereographic colormap and polarization directionality mapping for a 10x10x10 supercell of BTO at 0.1GPa before (181K) and after (183K) the rhombohedral-to-orthorhombic phase transition. *Up:* Polarization density, initially distributed along the [1 1 1] direction within the [X Y Z] quadrant, scatters and begins migrating towards the [X Y -Z] quadrant. *Middle:* Polarization density redistributes among the [X Y Z] and [X Y -Z] quadrants as expected by the Takahasi model. *Down:* (Left) Only few unit cells adopt the [X Y -Z] directionality. (Right) The unit cells belonging to both available quadrants do not mix randomly among each other but rather form domain-like structures.

### Orthorhombic to Tetragonal phase transition

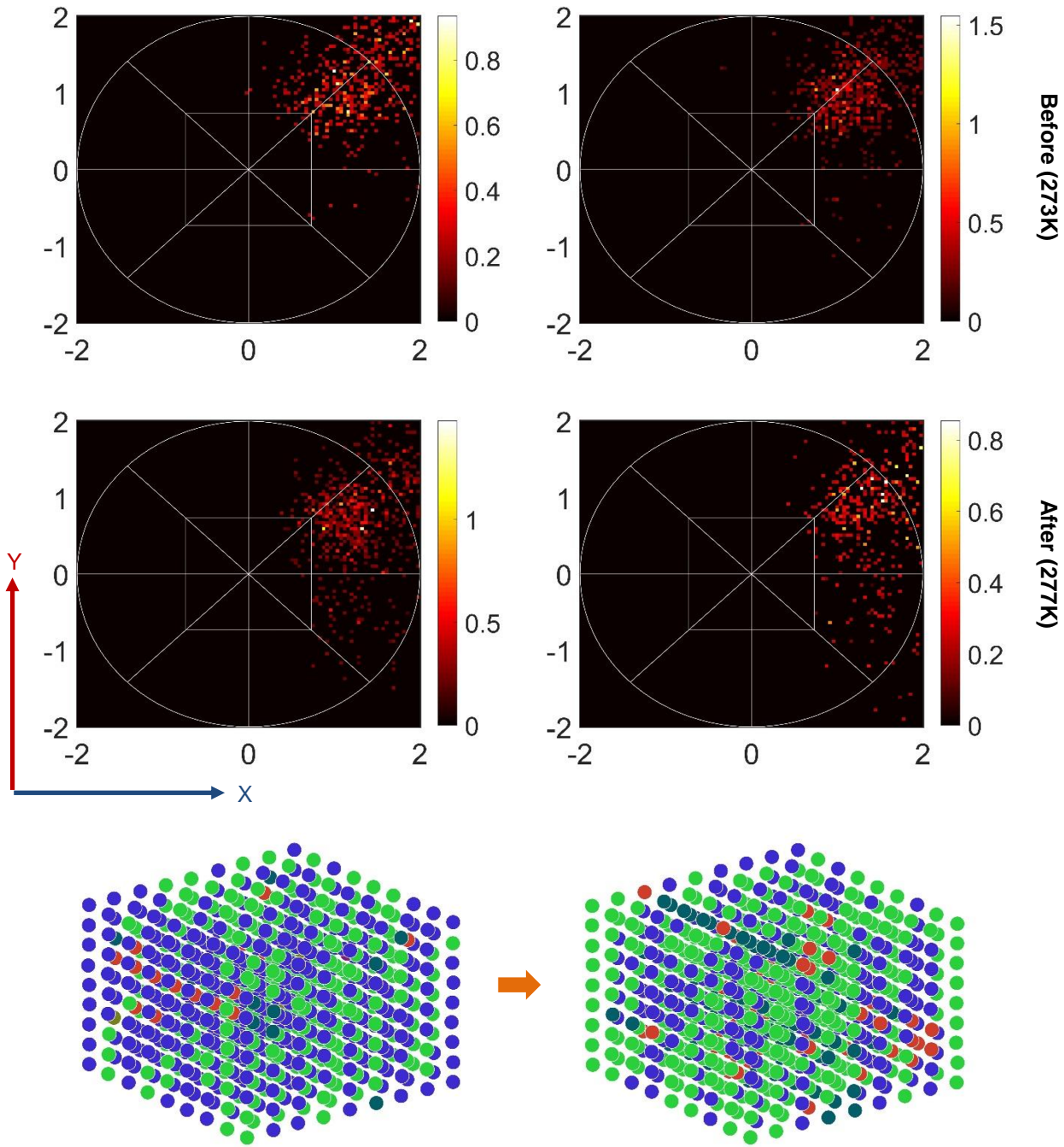


*Figure 25 –* Polarization stereographic colormap and polarization directionality mapping for a 10x10x10 supercell of BTO at 0.1GPa before (273K) and after (277K) the *orthorhombic-to-tetragonal* phase transition. *Up:* Polarization density, initially distributed along the line joining the [1 1 1] and [1 1 -1] directions within the [X Y Z] and [X Y -Z] quadrants, scatters and begins migrating towards the [X -Y Z] and [X -Y -Z] quadrants. *Middle:* Polarization density redistributes among the [X Y Z], [X Y -Z], [X -Y Z] and [X -Y -Z] quadrants as expected by the Takahashi model. *Down:* (Left) Only few unit cells adopt the [X -Y Z] and [X -Y -Z] directionalities. (Right) The unit cells belonging to the four available quadrants do not mix randomly among each other but rather form domain-like structures.

### Tetragonal to Cubic phase transition

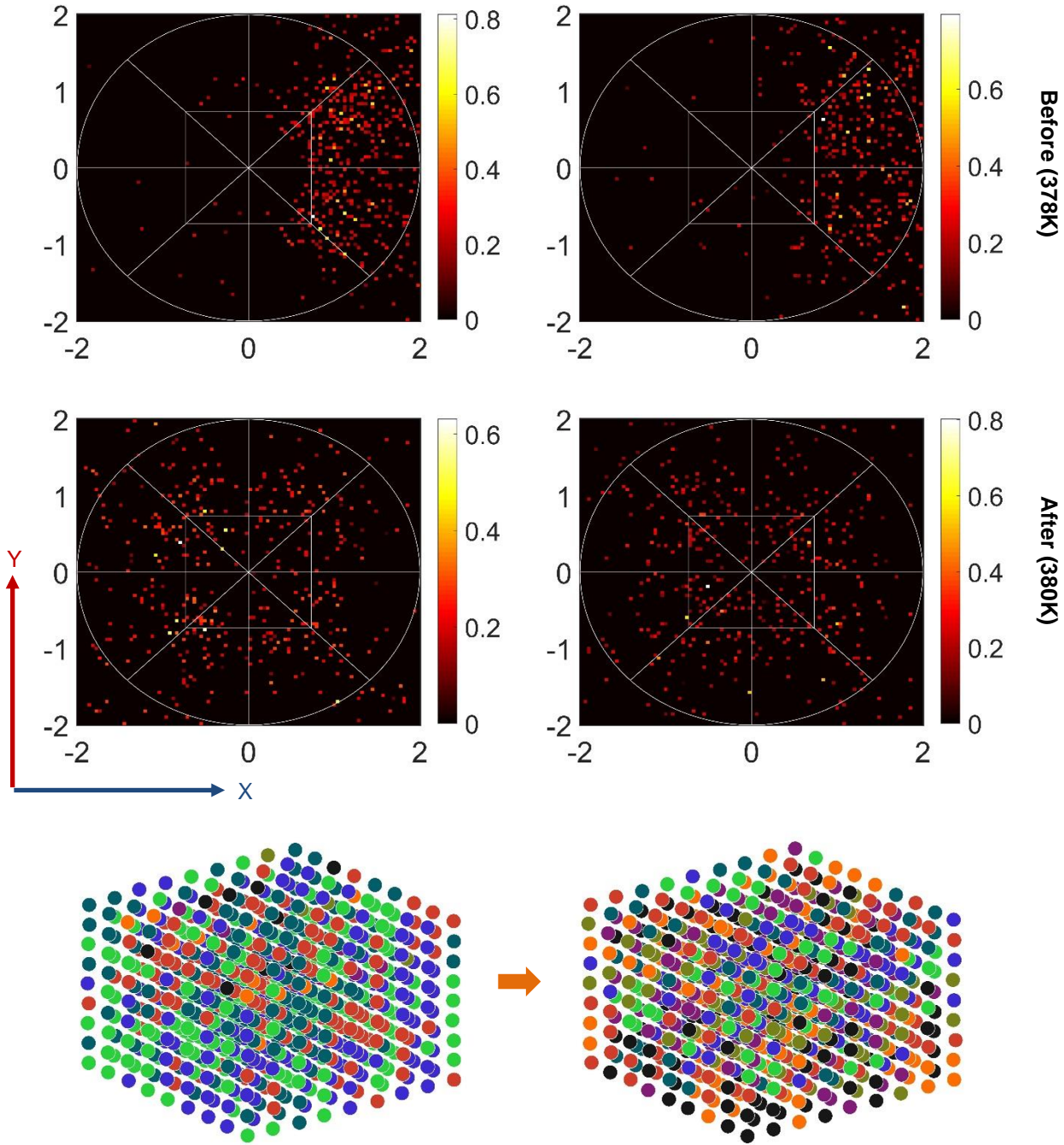


*Figure 26 –* Polarization stereographic colormap and polarization directionality mapping for a 10x10x10 supercell of BTO at 0.1GPa before (378K) and after (380K) the tetragonal-to-cubic phase transition. *Up:* Polarization density, initially distributed close to the  $\langle 1\ 1\ 1 \rangle$  directions within the  $[X\ Y\ Z]$ ,  $[X\ Y\ -Z]$ ,  $[X\ -Y\ Z]$  and  $[X\ -Y\ -Z]$  quadrants, scatters and begins migrating towards the  $[-X\ Y\ Z]$ ,  $[-X\ Y\ -Z]$ ,  $[-X\ -Y\ Z]$  and  $[-X\ -Y\ -Z]$  quadrants. *Middle:* Polarization density redistributes among all the quadrants as expected by the Takahashi model. *Down:* (Left) Only few unit cells adopt the  $[-X\ Y\ Z]$ ,  $[-X\ Y\ -Z]$ ,  $[-X\ -Y\ Z]$  and  $[-X\ -Y\ -Z]$  directionalities. (Right) The unit cells belonging to all quadrants do not mix randomly among each other but rather form domain-like structures.

From figures 24 to 26 phase transitions are always accompanied by polarization density reconfiguration according to the Takahashi model (compare the lattice parameters evolution and the polarization history in figure 19); indeed, it takes times in the order of few picoseconds for the polarization to migrate into new available thermally-activated directionalities once the corresponding phase transition temperature has been reached. Nevertheless, these results arise from simulations on which the polarization was previously equilibrated during the thermalization stage (as is the case of all the *Phase\_Diagram\_#* simulations here reported). When polarization density is not a priori equilibrated it may happen that the lattice parameters evolution still reproduces the phase transitions while not being accompanied by the expected polarization reconfiguration. This behavior of the model, which has been proven in several simulations not reported in this thesis, indicates that the polarization reconfiguration might be a slower mechanism not necessarily involved in the phase transformation, but triggered by the phase transformation.

As stated in section 2.2. of the *literature review*, several research groups have made big efforts to bring to light the underlying BTO phase transformation. One interesting route to follow consists in performing vibrational studies based on phonon dispersion analysis near the phase transitions (see section 4.5. in *future work* of this chapter)

In figure 24, the polarization density initially distributed along the [1 1 1] direction, migrates towards the [X Y -Z] quadrant such that the unit cells switch its polarization direction collectively, forming continuous structures resembling polarization domains. The structures are highly dynamic, being able to migrate or create/annihilate in time intervals ranging from few femtoseconds to several picoseconds; furthermore, its behavior is dependent of temperature and the application of external electric fields. In figure 25, the occupation of the quadrants available in the tetragonal phase is again marked by the clustering phenomena; although the structures are smaller due to the existence of four available quadrants instead of only two for the orthorhombic phase.

Finally, in figure 26 the annihilation of average polarization density for the cubic paraelectric phase is explained from the occupation of all possible quadrants towards the  $\langle 1 \ 1 \ 1 \rangle$  directions given in the Takahashi model; besides, although the average polarization does cancel, it fluctuates considerably around zero due to the continuous migration of polarization density among the eight quadrants (see the polarization history in figure 19). The directionality distribution of polarization density within the supercell looks much more random, although there still prevails some degree of clustering between units cells whose polarization vector belongs in the same quadrant.

---

## 1.6. EXPERIMENTAL COMPARISON

In figure 27, the polarization density and triclinic lattice constants evolution of a BTO  $10 \times 10 \times 10$  supercell at atmospheric pressure is shown as obtained by Boddu et al. by means of MD simulations using the Vielma et al. ab initio parameters. Meanwhile, in figure 28 the experimental temperature vs. pressure phase diagram of BTO is shown as obtained from Ishidate et al. and compared to a modified classical Devonshire model [15] [22] [23] [39].

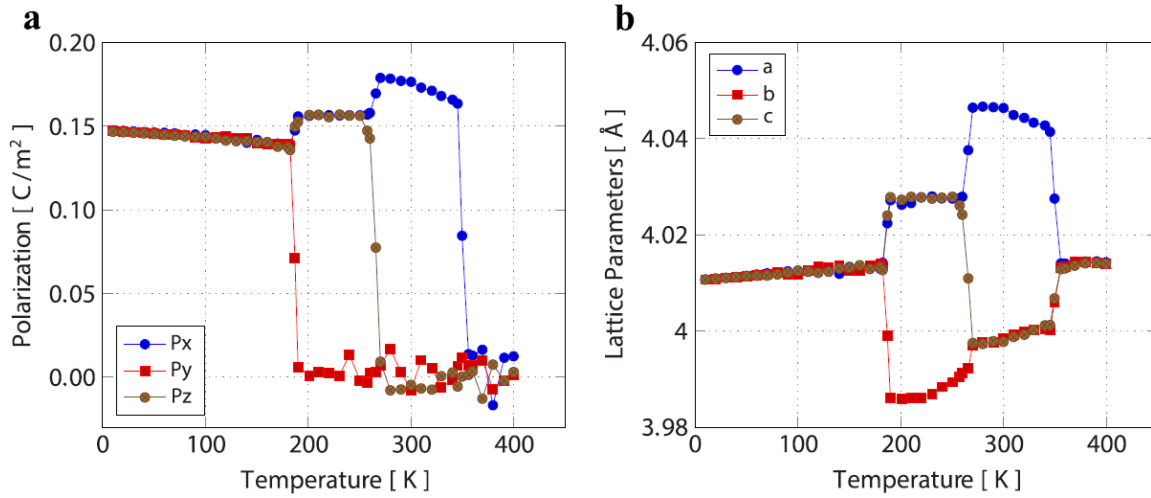


*Figure 27 – a: Average polarization density components for a  $10 \times 10 \times 10$  BTO supercell at atmospheric pressure. b: Triclinic lattice constants evolution for the same BTO supercell.*

Figure taken from [22].

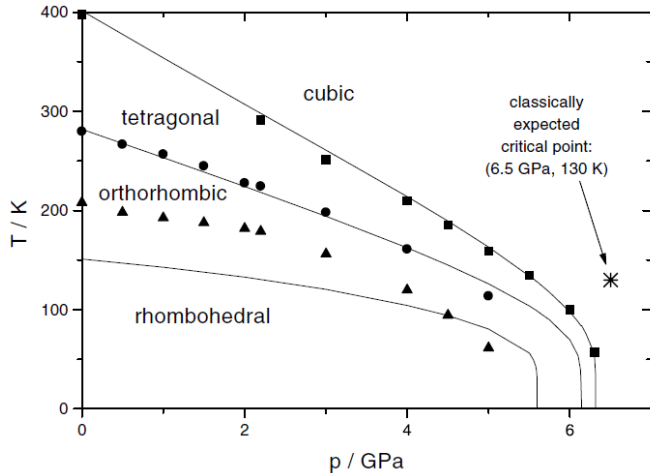


*Figure 28 – Temperature versus pressure diagram of BTO obtained from experimental data of Ishidate et al. as compared to a modified Devonshire model (solid lines).*

Figure taken from [15].

Comparison of figures 19 and 27 provides an excellent correspondence between the results by Boddu et al. and the ones obtained in this thesis; that is, the phase transition temperatures and polarization components display similar values in both cases. Thus, the model employed performs well in terms of stability and reproducibility, and the procedures followed in this thesis aiming to build the phase diagram can be trusted.

On the other hand, the phase diagram built in figure 23 does not display the decaying behavior of the phase boundaries showed in figure 28 near a pressure of 6 GPa. Moreover, in figure 23 the two critical points observed are clearly overestimated in pressure as compared to the experimental results; however, the temperatures at which both occur are more consistent with the Ishidate et al. data, on which the rhombohedral-tetragonal and orthorhombic-tetragonal boundaries may converge in a first critical point before joining to the tetragonal-cubic curve.

Furthermore, the MD model does not reproduce the non-linear behavior of the rhombohedral-orthorhombic boundary; besides, the transition temperatures at atmospheric pressure are underestimated especially in the case of the rhombohedral-orthorhombic and tetragonal-cubic curves. In any case, the existence of a single critical point at 6.5GPa and 130K is discarded by the experimental data and the Devonshire and MD models.

## CALCULATING THE PIEZOELECTRIC COEFFICIENTS

### 2.1. SIMULATION ANALYSIS

In the *Piezoelectric\_300* simulation, the converse piezoelectric effect is tested in the tetragonal phase of a 30x30x30 BTO supercell by means of the application and relaxation of a 250MV/m electric field towards the z-direction. A bigger supercell has been employed to improve the global strain tensor [ $S$ ] measurement previously described in section 2.3. of the *computational procedures* chapter. The triclinic lattice constants evolution is displayed in figure 29 while the polarization history is shown in figure 30.

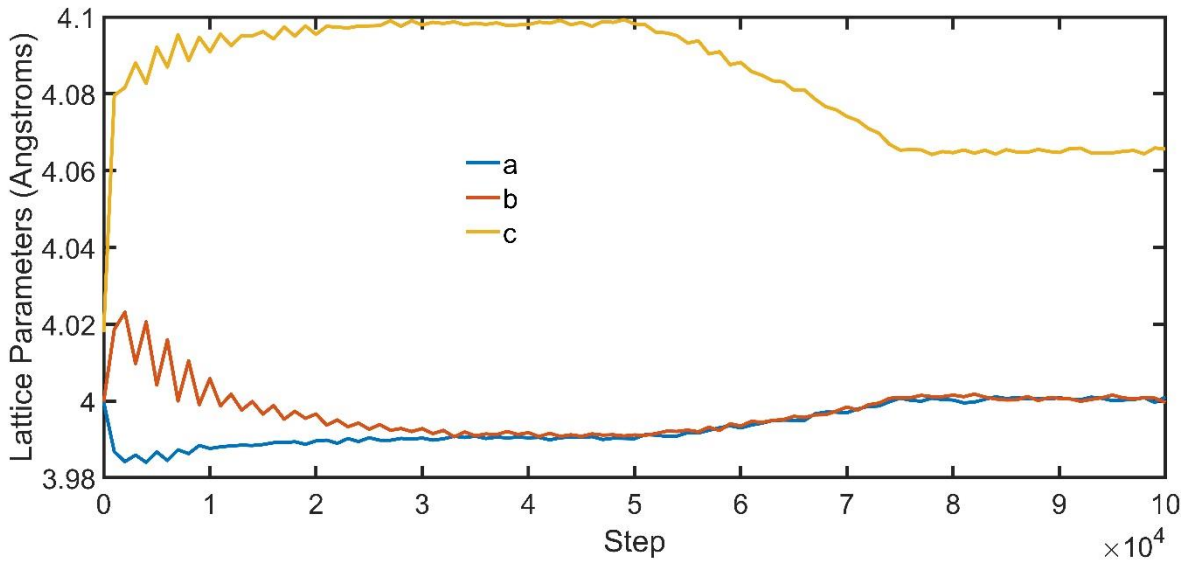


*Figure 29 – Triclinic lattice constants evolution for a 30x30x30 BTO supercell at 300K and 0.1GPa. An external electric field of 250MV/m is applied towards the z-direction during the first 50,000 simulation steps. The field is linearly released during the next 25,000 iterations, becoming null at the 75,000.*

During the first 50,000 steps, the electric field stretches the tetragonal lattice towards the z-direction as can be seen from the value of  $c$ . Also, the lattice shrinks in the x-direction and y-direction due to Poisson effect. It should be noticed that the supercell thermalizes during the first 35,000 steps (14ps), approximately. This means that the thermalization of bigger supercells via the induced-polarization method is more computationally demanding (compare with figure 17).

As the electric field decreases linearly from step 50,000 to 75,000, the lattice relaxes until it reaches the equilibrium state of remnant polarization characteristic of the tetragonal phase, with magnitude of  $0.19\text{C/m}^2$  (compare figure 30 with figure 13).

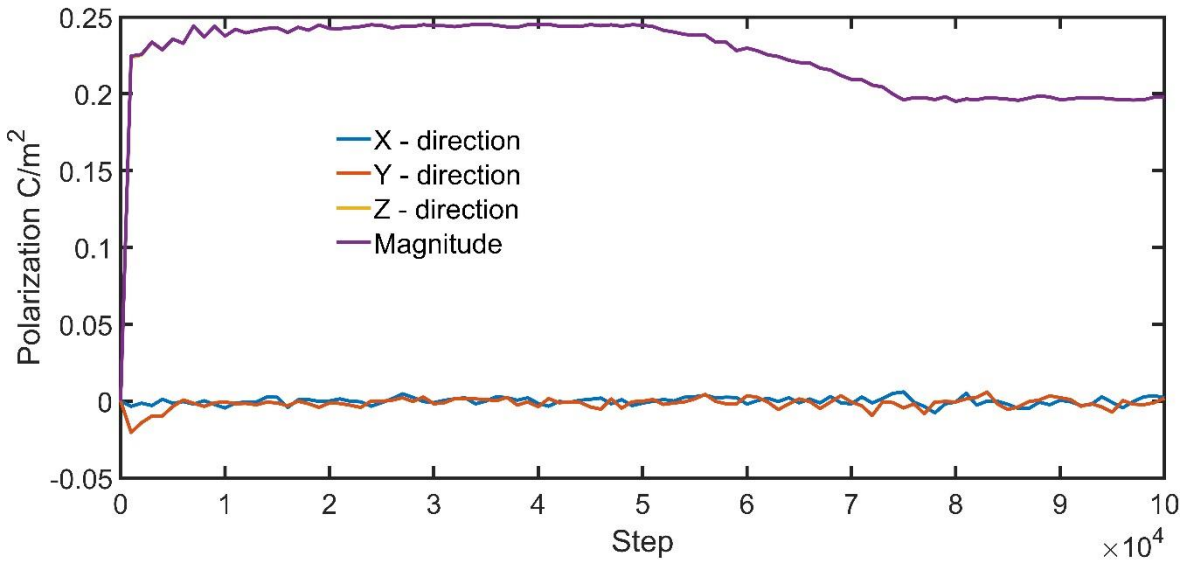


*Figure 30 – Average polarization density for a  $30 \times 30 \times 30$  BTO supercell at 300K and 0.1GPa. An external electric field of 250MV/m is applied towards the z-direction during the first 50,000 simulation steps. The field is linearly released during the next 25,000 iterations, becoming null at the 75,000. The polarization magnitude and its z-direction component are nearly overlapped.*

## 2.2. THE PIEZOELECTRIC COEFFICIENTS

The global strain tensor  $[S]$  has been calculated between the steps 40,000 and 80,000 of the simulation, yielding:

$$[S] = \begin{bmatrix} 0.002465 & 0.000007 & 0.000075 \\ 0.000007 & 0.002451 & 0.000109 \\ 0.000075 & 0.000109 & -0.008111 \end{bmatrix}$$

Equation (36)

The strain tensor representation is consistent with the tetragonal symmetry of the deformation generated from the lattice relaxation. Only the diagonal elements are not negligible and from them the  $S_{xx}$  and  $S_{yy}$  are expansive and practically equal, while the  $S_{zz}$  is compressive and nearly four times higher in magnitude than  $S_{xx}$  and  $S_{yy}$ . Given that the deformation was caused by an electric field of 250MV/m in the z-direction and that there was no externally applied stress<sup>15</sup>, substituting the corresponding values in equation (19) for the converse piezoelectric effect in a tetragonal supercell, gives:

<sup>15</sup> The base level pressure of the barostat is neglected.

$$\begin{bmatrix} 0.002465 \\ 0.002451 \\ -0.008111 \\ 0.000109 \\ 0.000075 \\ 0.000007 \end{bmatrix} = \begin{bmatrix} 0 & 0 & d_{31} \\ 0 & 0 & d_{31} \\ 0 & 0 & d_{33} \\ 0 & d_{15} & 0 \\ d_{15} & 0 & 0 \\ 0 & 0 & 0 \end{bmatrix} \begin{bmatrix} 0 \\ 0 \\ 250 \end{bmatrix}$$

Equation (37)

Which can be solved for the  $d_{31}$  and  $d_{33}$  coefficients, yielding:

$$d_{31} = 9.8(3) \text{ pC/N}$$

$$d_{33} = 32.44 \text{ pC/N}$$

Equation (38)

Where the last digit in the coefficient  $d_{31}$  was obtained from averaging the  $S_{xx}$  and  $S_{yy}$  elements in the strain tensor. The value of  $d_{33}$  is slightly underestimated from the experimental value ranging from  $45\text{pC/N}$  to  $172\text{pC/N}$  as obtained by Hiroshi Maiwa [27]. Nevertheless, in this case a perfectly crystalline supercell is being studied instead of a bulk material like the HIP-BT. Finally, the calculation of the  $d_{15}$  piezoelectric coefficient is a more delicate task from the perspective of MD simulations. This is because the application of electric fields in a non-symmetry axis breaks the tetragonal symmetry of the supercell lattice; nonetheless, the measurement might be possible by employing weaker electric fields, although bigger supercells would be required to appreciate the global deformation.

## HYSTERESIS CYCLES AND FERROELECTRICITY

### 3.1. SIMULATION ANALYSIS

*Hysteresis\_100*, *Hysteresis\_220*, *Hysteresis\_300* and *Hysteresis\_400* are designed to test the electric behavior of BTO in the four phases exhibited at atmospheric pressure. A full +  $\frac{1}{4}$  cycle of sinusoidal electric field with null phase factor and magnitude of  $120\text{MV/m}$ ,  $75\text{MV/m}$ ,  $50\text{MV/m}$ ,  $100\text{MV/m}$ , resp. was applied during 2,500,000 simulation iterations. The supercells were pre-polarized in the directions  $[1\ 1\ 1]$ ,  $[1\ 1\ 0]$ ,  $[0\ 0\ 1]$ , respectively (except for the cubic phase), via the induced-polarization method described in section 1.3. of this chapter. The sinusoidal field was applied in the same direction as in the induced-polarization stage; therefore, polarization density was projected in the electric field direction when building the corresponding curves against electric field. The hysteresis loops for each simulation are shown in figures 31 to 34, respectively, where a *wavelet transform* algorithm was employed to denoise the plots from thermostat and barostat oscillations.

At first sight, the paraelectric behavior in the cubic phase is immediately recognized from the other three ferroelectric phases, the later requiring an electric field offset to cancel and reverse the spontaneous polarization in a process known as *ferroelectric switching*.

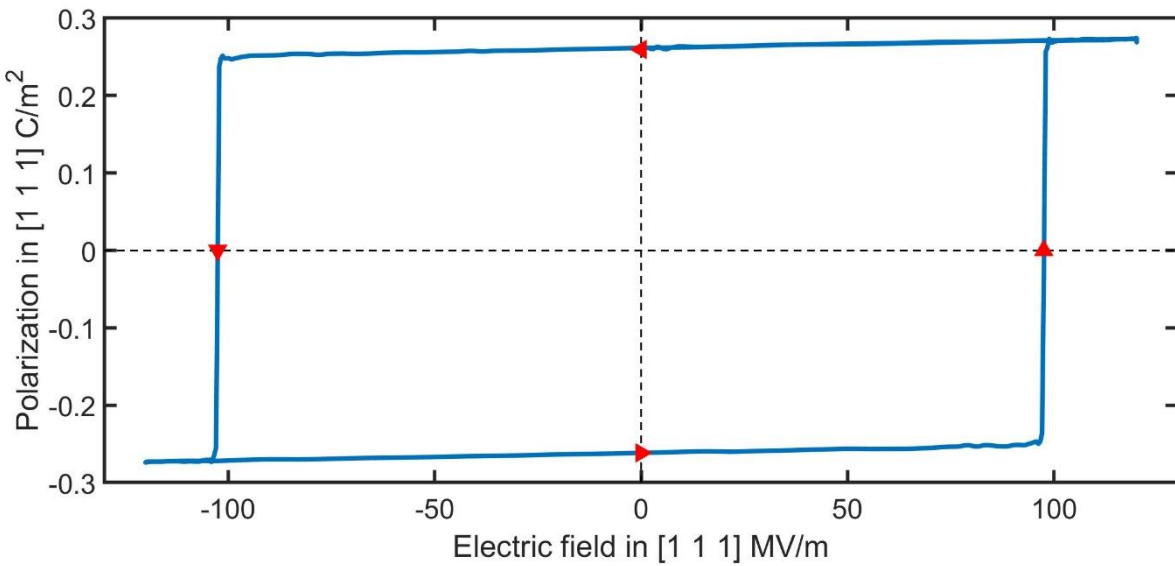


*Figure 31 – Polarization density versus electric field in the [1 1 1] direction for a 10x10x10 BTO supercell at 100K and atmospheric pressure (rhombohedral). A full + ¼ cycle of sinusoidal electric field with null phase factor and magnitude of 120MV/m is plotted. The loop is characteristic of ferroelectric switching and its intersections with the polarization density and electric field axes are marked by the red triangles.*

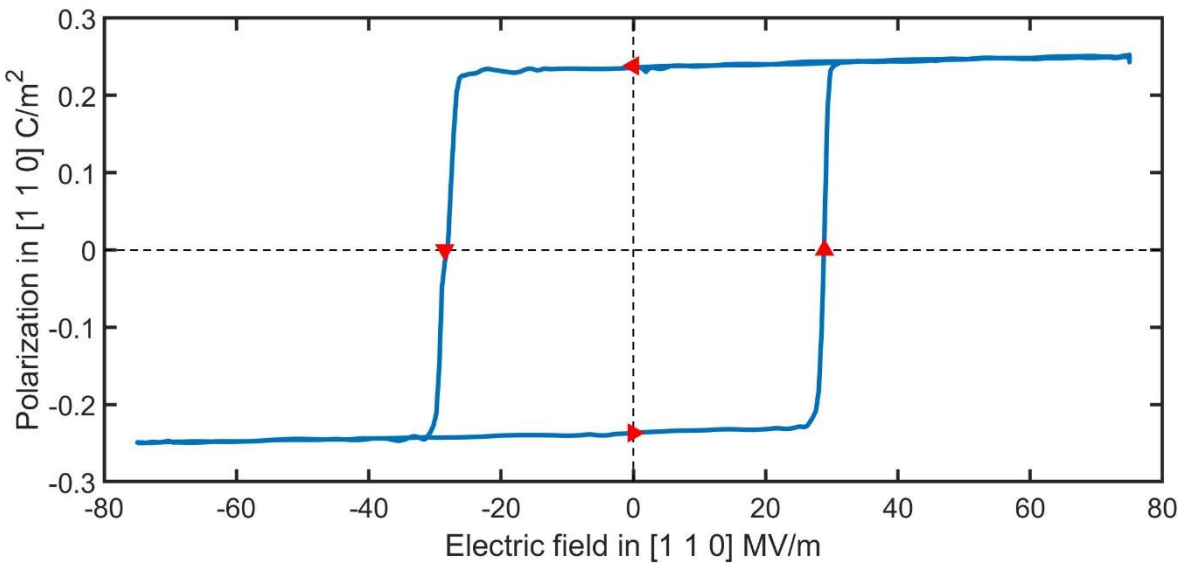


*Figure 32 – Polarization density versus electric field in the [1 1 0] direction for a 10x10x10 BTO supercell at 220K and atmospheric pressure (orthorhombic). A full + ¼ cycle of sinusoidal electric field with null phase factor and magnitude of 75MV/m is plotted. The loop is characteristic of ferroelectric switching and its intersections with the polarization density and electric field axes are marked by the red triangles.*

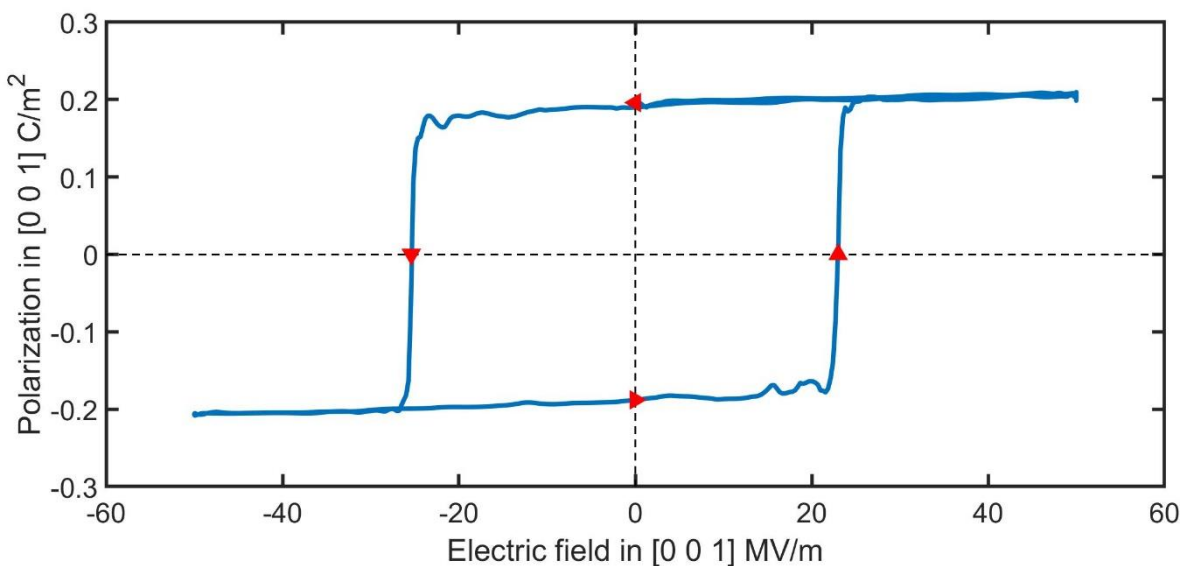


*Figure 33* – Polarization density versus electric field in the  $[0\ 0\ 1]$  direction for a  $10 \times 10 \times 10$  BTO supercell at 300K and atmospheric pressure (tetragonal). A full  $+ \frac{1}{4}$  cycle of sinusoidal electric field with null phase factor and magnitude of 50MV/m is plotted. The loop is characteristic of ferroelectric switching and its intersections with the polarization density and electric field axes are marked by the red triangles.

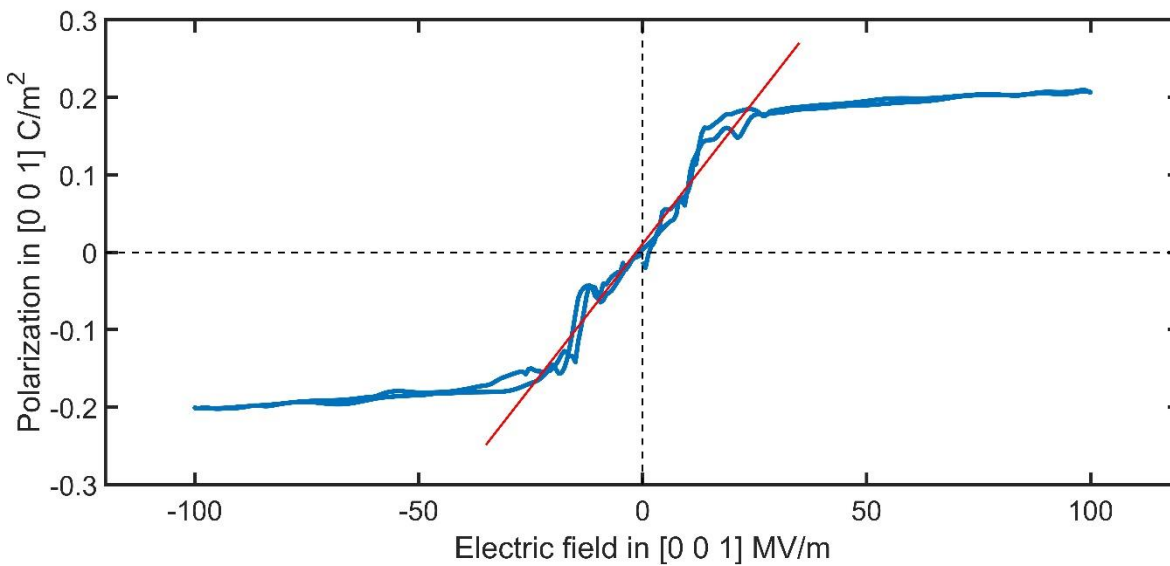


*Figure 34* – Polarization density versus electric field in the  $[0\ 0\ 1]$  direction for a  $10 \times 10 \times 10$  BTO supercell at 400K and atmospheric pressure (cubic). A full cycle of sinusoidal electric field with null phase factor and magnitude of 100MV/m is plotted. The absence of a loop is typical of paraelectric behavior. A linear model has been fitted around the origin to estimate the dielectric constant (see section 3.2. of this chapter).

Moreover, the rhombohedral phase in figure 31 exhibits very sharp hysteresis but the behavior smoothens with temperature as can be seen from the loops in the orthorhombic and tetragonal geometry. Further, the polarization saturation values for the rhombohedral, orthorhombic and tetragonal phase are  $0.27\text{C/m}^2$ ,  $0.24\text{C/m}^2$  and  $0.20\text{C/m}^2$ , respectively, which are practically equal to the values of remanence or spontaneous polarization intersecting the electric field axis:  $0.26\text{C/m}^2$ ,  $0.24\text{C/m}^2$  and  $0.19\text{C/m}^2$ , the latter being coincident with the ones previously reported in figures 11 to 13. Besides, the polarization saturation and spontaneous polarization values are symmetric in the positive and negative states of the ferroelectric switch; however, there is some level of asymmetry in the coercivity of the cycles; that is, in the values of electric field needed to cancel the polarization. The asymmetry is higher in the rhombohedral phase with coercivities of  $-102.5\text{MV/m}$  and  $97.5\text{MV/m}$ ; moderated in the tetragonal phase with  $-25.4\text{MV/m}$  and  $23.0\text{MV/m}$ , and relatively low in the orthorhombic phase with  $-28.5\text{MV/m}$  and  $28.9\text{MV/m}$ . This behavior might be caused due to some level of randomness generated due to thermal fluctuations at the onset of the ferroelectric switching.

Also, simulation instabilities increase with temperature, especially in the case of the cubic paraelectric phase. This behavior, which was previously observed in figures 19 to 22 when building the temperature versus pressure diagram, is attributed to the migration of the titanium atom among the thermally activated directions given by the Takahasi model. Nonetheless, good reproducibility is observed in the electric behavior of the cubic phase, as can be seen from the overlapping of the polarization vs electric field curve within the full cycle; furthermore, the saturation points are relatively symmetric with values of  $0.18\text{C/m}^2$  at  $26.7\text{MV/m}$  and  $0.18\text{C/m}^2$  at  $-28.5\text{MV/m}$ .

---

### 3.2. ELECTRIC SUSCEPTIBILITY AND DIELECTRIC CONSTANTS

The fact that the remanence and polarization saturation values coincide in the ferroelectric phases makes it impossible to determine their electric susceptibility. For the  $10 \times 10 \times 10$  simulated supercells the polarization of every unit cell rapidly points towards the externally applied electric field; however, in bulk BTO this happens to be a gradual process involving complex energy minimization mechanisms, which consist of switching multiple polarization domains until the maximum level of alignment provided by the crystal structure has been reached. Thereby, the  $10 \times 10 \times 10$  boxes are by far insufficient to expand the ferroelectric behavior of the polarization density in powers of the electric field by means of electric susceptibilities:

$$\mathbf{P}_T = \mathbf{P}_S + \varepsilon_0[\mathbf{X}] \mathbf{E} + \dots$$

Equation (39)

Where the sum is truncated to first order (compare with equation 21). Nonetheless, as shown in figures 31 to 33, the ferroelectric switching can be successfully reproduced. On the other hand, the cubic paraelectric phase does not exhibit the difficulties attributed to the ferroelectric phases. Its polarization density shifts smoothly from the negative to the positive state guided solely by the external electric field and the internal thermal fluctuations.

Thus, equation (39) with the zeroth order ferroelectric term discarded can be used to fit a linear model next to the origin in figure 34. The obtained slope has a value of  $7.4 * 10^{-9} C/Vm$ , which is equivalent to the relative permittivity or dielectric constant for the paraelectric cubic phase (see equations 9 and 10):

$$\varepsilon_r = 1 + \chi_{11} = 836.8$$

Equation (40)

The value is consistent with the ones reported in experimental studies, although these can range from 500 up to 10,000. For example, Petrovsky et al. found a value of 500 for hydrothermal BTO powders that raised up to 3,000 after annealing at 1250°C. Meanwhile, Maiwa found values ranging from 2850 to 4050 for HIP-BT dependent on annealing temperature, density and grain size [27] [40]. Thereby, the MD model predicts a relatively low value of the dielectric constant, although being able to estimate it from first principle calculations is remarkable.

Finally, as mentioned in the calculation of the piezoelectric coefficients for the tetragonal phase at 300K, the effect that an externally applied electric field has on the triclinic lattice parameters is substantial. When building the hysteresis loops, the electric field direction was chosen to maintain the corresponding lattice geometry at the given temperature; otherwise, the converse piezoelectric effect would have induced a phase transition and the crystal symmetries given at a certain temperature would have been broken. In figure 35, the triclinic lattice constants evolution for the paraelectric cubic phase subject to the 100MV/m cyclic electric field in the [0 0 1] direction exposes the amount of strain induced in the supercell (compare with figure 34).

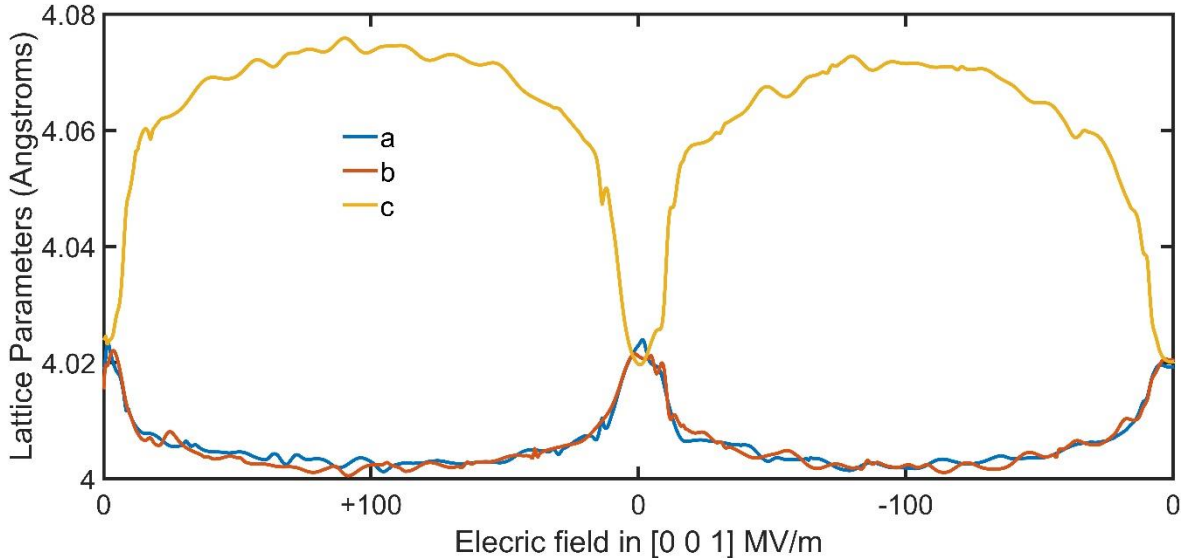


Figure 35 – Triclinic lattice parameters evolution for a 10x10x10 BTO supercell at 400K under the application of a sinusoidal electric field with amplitude of 100MV/m pointing towards the z-direction. A full cycle is shown in the picture.

## FUTURE WORK

This section is designed to introduce the author's current research aiming to analyze BTO flexoelectricity via MD simulations. Although the preliminary results and methods behind them are far more elaborated and beyond the scope of this thesis, is enriching to at least review them here briefly.

### 4.1. RELEASING THE PERIODIC BOUNDARIES

Until now, the simulations reported in this thesis considered the application of periodic boundary conditions in the three supercell directions; however, focusing in flexoelectricity both a mathematically compatible<sup>16</sup> and simple enough strain gradient are required for performing realistic and easily analyzable experiments, respectively. Thereby, the release of at least one periodic direction is required for carrying out flexion or indentation; in fact, the release of two or even three would be ideal for achieving simple bending states.

The main problematic with releasing periodic boundary conditions is the appearance of free surface. The core-shell model derived by Vilma et al. was built assuming periodicity of the supercell; thereby, there is no guarantee that it would behave as expected or be stable in the presence of free surface. Fortunately, when testing several supercells in the shape of indentation boxes and beams with only two periodic directions and one periodic direction, respectively, it was found that the model maintains its stability and physical fidelity under certain specific conditions and rules. Some of these are listed as follows:

- *Particle-freezing*: When trying to maintain the supercell fixed, like in the case of a cantilever beam, pinning the coordinates of some particles to simulate the supporting wall results in poor physical results and eventual collapse of the simulation.
- *Auto-bend*: When there is no symmetric distribution of electric charge along the supercell, it bends due to the unbalanced repulsion and attraction present at the free surface (see figure 36).
- *Free-corners*: The presence of free corners in the supercell is highly unstable and always leads to simulation collapse. Therefore, until now, the maximum number of non-periodic directions for achieving a stable simulation is two.
- *Vibration-reduction*: The presence of free surface favors the introduction of unwanted supercell collective oscillations (mainly during the thermalization stage); thereby, special methods such as simulated viscosity need to be applied for achieving energy minimization and time independent strain gradients.

---

<sup>16</sup> The strain gradient  $[\partial S]$  must obey a series of compatibility equations when analyzed from the perspective of continuum mechanics.

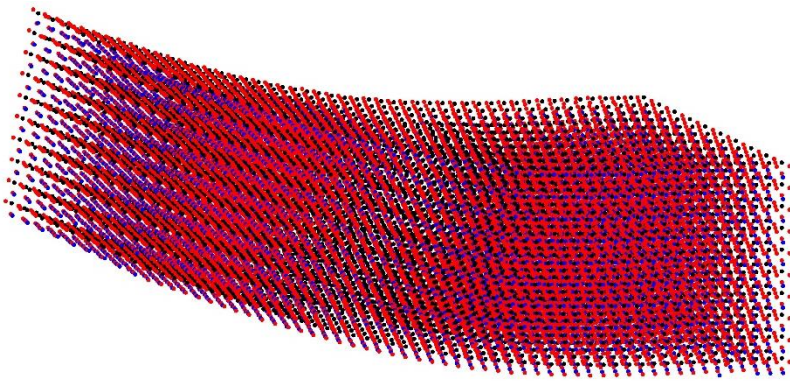


*Figure 36 – 50x10x10 BTO supercell with two non-periodic directions displaying *auto-bending* due to charge asymmetry originated from the upper surface being made of titanium-oxygen atoms and lower surface consisting in a barium-oxygen layer. Titanium atoms are represented in black, oxygen atoms in red and barium atoms in blue. The beam is pinned from the right via *particle-freezing*, which eventually leads to simulation collapse.*

In section 4.2. below, some solutions to avoid the *auto-bend* are introduced, while in section 4.3. a successful alternative to *particle-freezing* is explored.

---

## 4.2. SURFACE MODIFICATIONS

A straightforward solution to avoid supercell *auto-bend* consists in generating supercells with symmetrical electric charge distribution with respect to the free surface. For that purpose, the supercell generating software *BTO\_generator* was expanded to support surface modifications divided in two categories:

- *Invariant modifications* – This type of surface modifications preserve the total stoichiometry and charge neutrality of the BTO supercell; that is, like for the case of the fully periodic supercells employed in this thesis, the number of barium, oxygen and titanium atoms are in the proportion 1:3:1, respectively. Furthermore, the net electric charge of the supercell is zero. The advantage of this kind of surface modification is that the supercell cannot move as a rigid body with the application of external electric fields; nonetheless, the free surface configuration may be unstable and its geometry need to be tested in simulation (see figure 37).
- *Variant modifications* – This type of surface modifications does not preserve the total stoichiometry and charge neutrality of the BTO supercell; that is, atoms are added in the free surface to achieve the symmetric distribution of electric charge. The main advantage of this kind of modifications is the good stability of the surface geometry, although the lack of charge neutrality might generate rigid motion of the supercell when applying external electric fields (see figure 38).

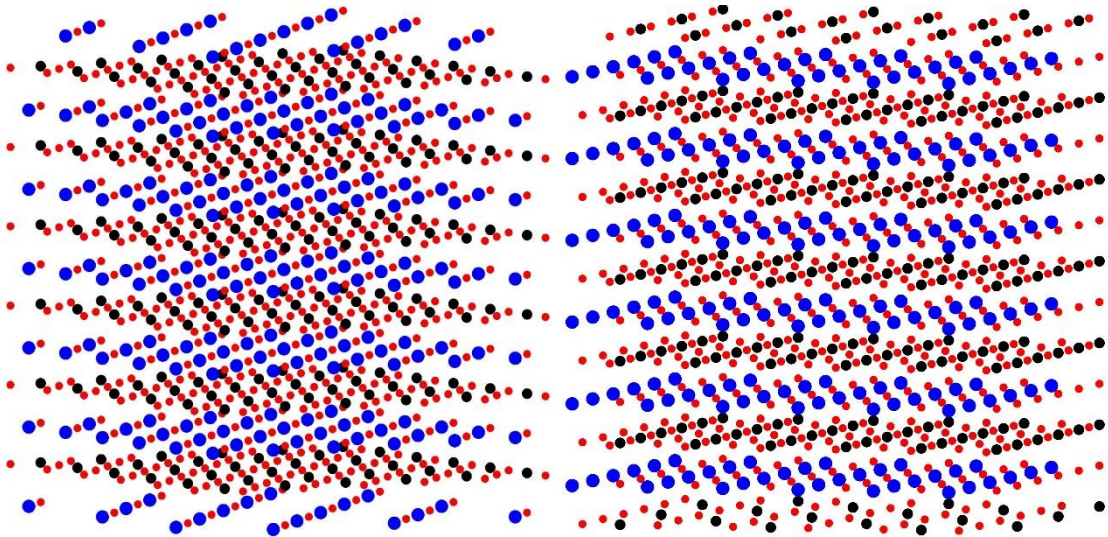


*Figure 37* – Two 6x6x6 BTO supercells with different style of invariant surface modification applied in the upper and lower layer. *Left*: Zig-zag barium-oxygen chain modification. *Right*: Oxygen-titanium-oxygen dotted line modification. It should be noticed that in both cases the missing atoms in the upper layer were translated to the lower layer; thus, preserving total stoichiometry and net electric charge neutrality. Titanium atoms are represented in black, oxygen atoms in red and barium atoms in blue.

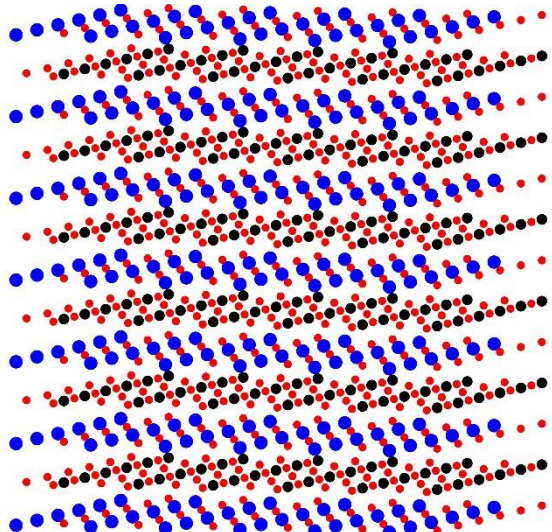


*Figure 38* – 6x6x6 BTO supercell with variant surface modification applied in the upper layer. A full plane of barium and oxygen atoms was added in the top of the supercell; thus, enhancing geometric stability at the expense of not preserving total stoichiometry and net electric charge neutrality. Titanium atoms are represented in black, oxygen atoms in red and barium atoms in blue.

#### 4.3. INDENTATION AND BENDING

Although from experimental experience indentation is a method to determine some mechanical properties of a sample, the basic definition of an indenter as a short-range bulk interaction can be extended to achieve controlled supercell confinement.

An indenter in LAMMPS is modeled analogously to an externally applied electric field, on which a constant force is simply added to the integrator for every iteration step. This time, instead of using the classical Lorentz expression, the force exerted by the indenter on a particle is calculated from a repulsive contact function with magnitude:

$$F(r) = \begin{cases} -K(r - R)^2 & r \leq R \\ 0 & r > R \end{cases}$$

Equation (41)

Where  $R$  is the radius of the indenter,  $r$  is the distance from the particle to the center of the indenter and  $K$  is the force constant representing the indenter hardness. The direction of the force lies in the line joining the center of the indenter and the corresponding particle. Moreover, only when the particle lies within the indenter radius a non-zero force will be exerted on it. Equation (41) can be easily generalized for other geometries rather than the spherical; in fact, LAMMPS supports spherical, cylindrical and plane indenters where the principal axis of the cylinder and the normal to the plane are restricted to be oriented in the  $x$ ,  $y$  or  $z$  directions. Nevertheless, Dr. Jan Ocenasek did modify the LAMMPS code of the plane indenter allowing for tilting the plane on a direction specified by the user. (see figure 39).

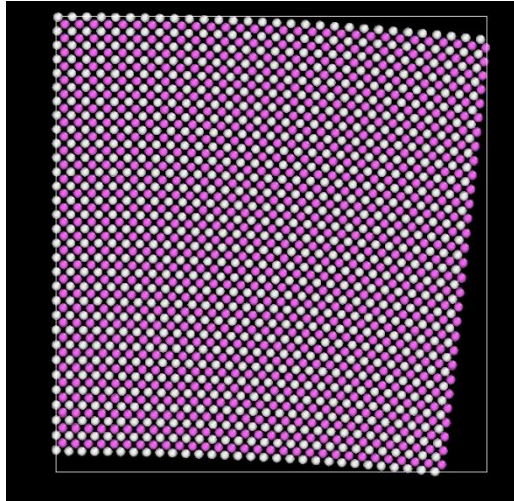


Figure 39 – Side view of a 30x30x30 BTO supercell with variant surface modification applied in the upper layer. Deformation has been generated using a tilted-plane indenter acting from the left. Circular indenters shape the bending at the top and bottom while a vertical plane indenter keeps the supercell fixed from the right. Periodic boundary conditions are applied in the direction normal to the picture. Barium atoms are shown in white and oxygen atoms in purple, using the OVITO open source visualization software.

The main advantage of indenters is that they can be used as constraining walls around the supercell without requiring the defective *particle-freezing* method. Indeed, the Vilma et al. model performs very well in non-periodic boundary conditions when using indenters to fix the supercell. Besides, plane, cylindrical and spherical indenters can be combined to generate more complicated configurations such as the three-point beam bending (see section 4.4. below). More information regarding the indenters supported by LAMMPS can be consulted in [41].

#### 4.4. FLEXOELECTRICITY AT FIRST GLANCE

By gathering all the information obtained from the BTO model described in this thesis, is possible to make the first attempts towards flexoelectricity. Flexoelectric experiments with non-periodic boundary conditions using the Vilma et al. BTO description have never been performed before; thus, the research line is as innovative as challenging. As stated in section 4.1. of this chapter, the main difficulty resides in the appearance of free surface; however, the application of surface modifications and the use of indenters to fix and deform the supercell, have proven to be the correct way to go in achieving stable simulations with relatively simple strain gradients.

Further, after several tests at different temperatures, the studies in flexoelectricity are now being focused in the paraelectric cubic phase. The reason is that the cubic supercell does not exhibit piezoelectricity due to its centrosymmetric geometry, making it the ideal candidate for symmetry breaking by the sole application of strain gradients. Until now, two main types of experiments are being performed:

- *Three-point bending* – A long BTO supercell resembling a beam is bent using three cylindrical indenters at the extremes of the bar and at its center such that a strain gradient is induced (see figure 40). The main advantage of this procedure is the great simulation stability that can be achieved after a proper thermalization; nevertheless, considerable amount of iterations is needed to tame the unwanted collective oscillations for achieving time independent strain gradients.
- *Accordion bending* – A pair of circular indenters, a plane indenter and a tilted-plane indenter are used to deform the supercell in the way shown in figure 39. The main advantage of this method is that the induced strain gradient has a simple mathematical description on which only one element of the strain gradient tensor  $[\partial S]$  is not null<sup>17</sup> (see appendix B); however, the stress field introduced by the indenters is difficult to estimate and to control.

So far, no sight of induced polarization due to strain gradients has been observed in the cubic phase; besides, experiments performed in the ferroelectric phases always develop polarization aligned with the longest dimension of the supercell regardless the application of strain gradients.

The latter result is an artifact due to the usage of non-periodic boundary conditions, inconsistent with the previous results on which the BTO phase diagram was reproduced. Bigger supercells, enhanced simulation scripts and better thermalization stages are being used/developed to overcome these difficulties; also, simulation collapse rarely occurs and the bending methods employed have proven to be reproducible.

---

<sup>17</sup> Several strain gradients were derived and analyzed in plane deformation conditions. The *accordion* bending is the best candidate for achieving simple strain gradient configurations (see appendix B).

On the other hand, the software extension for *BTO\_Visuals* to compute local strain tensor measurements has not yet been fully developed. In comparison to global strain tensor measurements, where a continuum mechanics approach can be directly applied to the whole simulation box, performing local studies requires suitable tessellation of the supercell aiming to describe the deformation process of single unit cells. This is not a simple task although several alternatives are being considered.

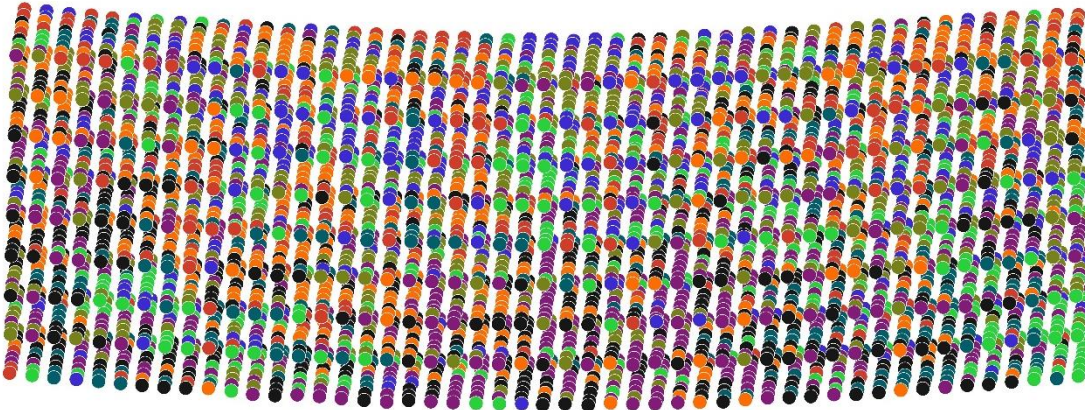


*Figure 40 – 50x10x10 BTO supercell at 400K and atmospheric pressure with two non-periodic directions and variant surface modifications displaying deformation due to three-point bending using cylindrical indenters. Each spherical marker represents a unit cell by means of its polarization direction according to the color code introduced in section 1.5. of this chapter. The polarization is nearly randomly distributed although a strain gradient induced state was expected.*

#### 4.5. PHONONS IN BTO

Besides flexoelectricity, an interesting and quite controversial research line regarding BTO is related to the underlying mechanisms acting in the phase transitions. As mentioned in section 2.2. of the *literature review*, the softening of phonon modes may be a key to understand these mechanisms; that is, the reduced role of thermal fluctuations in the polarization density distribution at different temperatures may be explained in terms of vibrational modes *frozen* at a certain BTO phase but active in another [8]. Thereby, performing vibrational studies of the BTO supercell by means of MD simulations provide an interesting approach. LAMMPS supports a method for obtaining phonon dispersion curves and phonon density of states directly from the evolution of the particle coordinates in the simulation. The algorithm, developed by Kong, relies in the calculation of phonon frequencies directly from the eigenvalues of the dynamical matrix obtained via time-averaged k-space transformation of the real space supercell [42]. LAMMPS implementation of the Kong method can be consulted in [43].

The algorithm was tested on different BTO supercells and post-processed using *BTO\_Visuals*; unfortunately, this approach turned out to be unsuccessful because of three main drawbacks:

- The algorithm is not suited for systems with many atoms per unit cell. BTO, having five atoms on its basis, considerably lowers the accuracy of the Kong method.
- The atoms in the core-shell model are not single particles. Kong model needs to be redefined to consider atoms as being split into two separate particles whose mutual vibrations accounts for a single possible phonon frequency.
- The number of wavevector points in the first Brillouin zone of the phonon dispersion curves is the total number of unit cells in the supercell; therefore, for achieving better resolution in the dispersion relations, bigger supercells must be employed.

Nonetheless, some features of the BTO supercell are correctly predicted by the Kong model, as explained in figure 41. Currently, the research group is working in adapting the Kong method for the core-shell model; besides, other alternatives for obtaining phonon dispersion and density of states in BTO simulations are reported in the literature [44] [45].

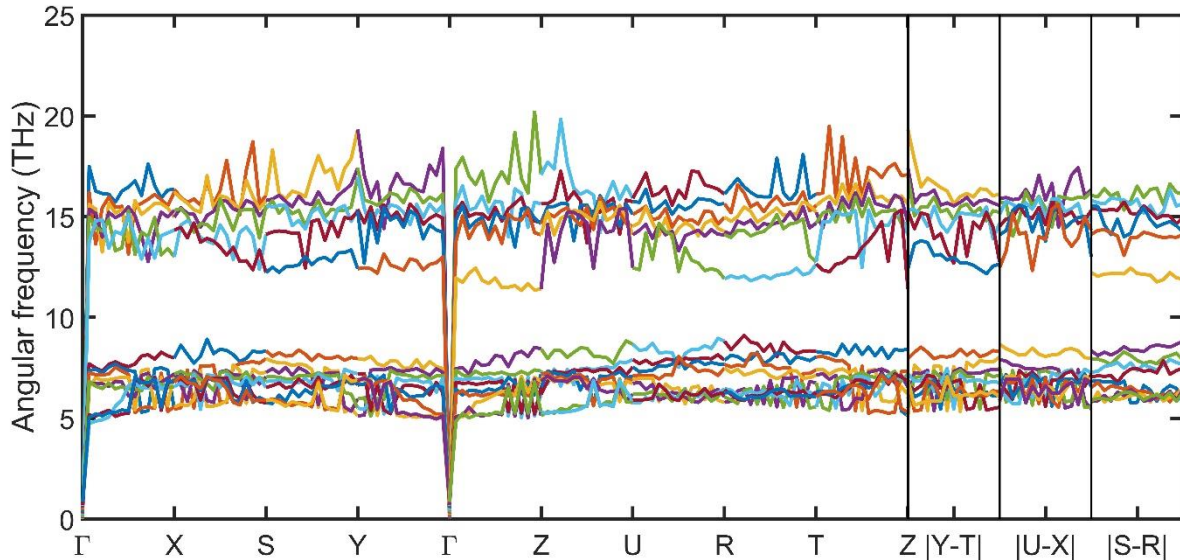


*Figure 41* – Phonon dispersion for the shells of a 30x30x30 periodic BTO supercell at 220K and atmospheric pressure. There are exactly 15 branches in the dispersion, associated with the three degrees of freedom for each of the five shells in a unit cell. The 15 low-frequency branches for the cores are not plotted. The dispersion is separated in two bands of high and low frequency with 6 and 9 branches, respectively, the former associated with the vibration of the titanium and barium shells and the latter due to the shell motion in the oxygen atoms. Acoustic and optic modes are distinguished among the high-symmetry directions of the first Brillouin zone in the orthorhombic BTO phase. The excessive noise and lack of accuracy (with respect to results reported in the literature) are due to having 10 particles per unit cell and not being able to group the cores and shells as single atoms within the Kong model.

## CONCLUSION

In this thesis, the core-shell model for BTO was implemented and successfully applied to investigate phase transitions under externally applied pressure, polarization loops, piezoelectric and flexoelectric responses. In doing so, custom-made simulation post-processing software was developed by the author.

The core-shell model fitted from *ab initio* calculations by Vielma et al. shows outstanding robustness in mimicking the thermodynamic and electric properties of BTO when using periodic boundary conditions. Although the critical point in the phase diagram is slightly overestimated and the transition temperatures are somewhat shifted as compared to the experimental values, the model adequately captures the rhombohedral, orthorhombic, tetragonal and cubic geometries. Furthermore, the polarization density shows a strong correspondence with the Takahashi model; even though the underlying mechanism for the phase transformation remains unclear. Local polarization nano-domains were observed when studying the polarization behavior near the phase transitions, opening the possibility for performing further research on the dynamical evolution of these structures, which naturally emerge and whose local arrangement is thought to rule the overall polarization density across the material scales.

The piezoelectric coefficients measured in the tetragonal phase and the estimated dielectric constant for the cubic paraelectric phase are in good agreement with the values reported in the literature. In this context, while the ferroelectric switching was reproduced in the simulations, new approaches must be considered aiming to estimate the electric susceptibility coefficients in the ferroelectric phases. One outcome of the investigation is the need to prevent strain-induced phase transitions, as they become important artifacts affecting computation of the piezoelectric coefficient  $d_{15}$  in the tetragonal phase.

The simulations show that the model by Vielma et al. displays significant robustness under periodic boundary conditions. A systematic study aiming to remove such conditions has been performed using indenters and surface modification techniques. Nonetheless, induced polarization due to the breakdown of centro-symmetry in the cubic paraelectric phase has not yet been observed and further efforts towards the modeling of flexoelectricity are needed. Also, new models of phonon dispersion obtained directly from particle coordinates in the core-shell model must be explored in the study of the role that crystal vibrational modes play in the phase transitions of BTO. Finally, the custom-made software developed during this investigation is anticipated to become a key element in future analyses of flexoelectricity. The software is continuously evolving to fulfil the requirements needed to measure new types of physical properties; mapping the local strain tensor emerges as an important priority in this regard.

## ECONOMIC & ECOLOGICAL IMPACT

The economic and ecological impact generated from the realization of this thesis are directly linked and related to the employment of the supercomputing cluster belonging to the Surface Interaction Group (InSup) of the Polytechnic University of Catalonia (UPC).

Average consumption per node of 16 processors is 2kWh<sup>18</sup>. All the simulations were run using parallelism between three nodes. The total estimated simulation time, including tests and essays not reported in this document, was nearly 672 hours. Thereby, the estimated total energy consumption is:

$$2 \text{ kWh} * \frac{3.6 \text{ MJ}}{1 \text{ kWh}} * 3 * 672 \approx 14.5 \text{ GJ}$$

Which is roughly equivalent to combusting 2 barrels (159L each) of crude oil<sup>19</sup>. The CO<sub>2</sub> emission per kWh reported by the Catalan Office of Climate Change in 2017 is 392g/kWh<sup>20</sup>. Hence, the approximate CO<sub>2</sub> emissions from developing this thesis are:

$$2 \text{ kWh} * 3 * 672 * \frac{392 \text{ g}}{\text{kWh}} \approx 1,580 \text{ kg}$$

Finally, the estimated cost of electricity according to the fares of some Catalan companies in 2018 is nearly 0.123€/kWh<sup>21</sup>. Besides, the amortized cost of supercomputing for the required time of 672 hours is nearly 1000€<sup>22</sup>; hence, the total economic cost due to the realization of this work is approximately:

$$2 \text{ kWh} * 3 * 672 * \frac{0.123 \text{ €}}{\text{kWh}} + 1000\text{€} \approx 1,496 \text{ €}$$

---

**Acknowledgement:** I would like to thank my mentors Prof. Jorge Alcalá Cabrelles and Dr. Jan Ocenasek for their time and the innumerable occasions they guide me through the development of this thesis. Moreover, my sincere gratitude goes to the AMASE program coordinators and the Erasmus+ association. Also, I want to thank the Polytechnic University of Catalonia for providing me access to the supercomputing cluster and to a proper workspace. Finally, I want to smile on my friends in both sides of the sea and my beloved Belgian girlfriend. This thesis is dedicated to my family, which is very far and very close.

---

<sup>18</sup> As reported in the UPC InSup archives.

<sup>19</sup> U.S. Energy Information Administration. [Online]. Available:  
[https://www.eia.gov/energyexplained/index.php?page=about\\_energy\\_units](https://www.eia.gov/energyexplained/index.php?page=about_energy_units)

<sup>20</sup> Government of Catalonia. [Online]. Available:  
[http://canvicalmotic.gencat.cat/es/reduceix\\_emissions/com-calcular-emissions-de-geh/factors\\_demissio\\_associats\\_a\\_lenergia/](http://canvicalmotic.gencat.cat/es/reduceix_emissions/com-calcular-emissions-de-geh/factors_demissio_associats_a_lenergia/)

<sup>21</sup> Holaluz Spain. [Online]. Available: <https://www.holaluz.com/tarifas-luz-un-precio-20/>

<sup>22</sup> As reported in the UPC InSup archives.

## REFERENCES

- [1] W. Cai, J. Li, and S. Yip, "1.09 - Molecular Dynamics," *Compr. Nucl. Mater.*, pp. 249–265, 2012.
- [2] J. K. Johnson, J. A. Zollweg, and K. E. Gubbins, "The lennard-jones equation of state revisited," *Mol. Phys.*, vol. 78, no. 3, pp. 591–618, 1993.
- [3] H. Goldstein, C. Poole, and J. Safko, "Classical Mechanics," *Book*. pp. 1–646, 2007.
- [4] R. Balescu, *Equilibrium and nonequilibrium statistical mechanics*, vol. 76. 1975.
- [5] D. J. Evans and B. L. Holian, "The Nose-Hoover thermostat," *J. Chem. Phys.*, vol. 83, no. 8, pp. 4069–4074, 1985.
- [6] H. J. C. Berendsen, J. P. M. Postma, W. F. Van Gunsteren, A. Dinola, and J. R. Haak, "Molecular dynamics with coupling to an external bath," *J. Chem. Phys.*, vol. 81, no. 8, pp. 3684–3690, 1984.
- [7] Kittel, *Introduction to Solid State Physics*. 2010.
- [8] M. Paściak, S. E. Boulfelfel, and S. Leoni, "Polarized cluster dynamics at the paraelectric to ferroelectric phase transition in BaTiO<sub>3</sub>," *J. Phys. Chem. B*, vol. 114, no. 49, pp. 16465–16470, 2010.
- [9] Y. Li, Z. Liao, F. Fang, X. Wang, L. Li, and J. Zhu, "Significant increase of Curie temperature in nano-scale BaTiO<sub>3</sub>," *Appl. Phys. Lett.*, vol. 105, no. 18, 2014.
- [10] Z. Zhang, D. Geng, and X. Wang, "Calculation of the piezoelectric and flexoelectric effects in nanowires using a decoupled finite element analysis method," *J. Appl. Phys.*, vol. 119, no. 15, 2016.
- [11] S. B. Lang, L. H. Rice, and S. A. Shaw, "Pyroelectric effect in barium titanate ceramic," *J. Appl. Phys.*, vol. 40, no. 11, pp. 4335–4340, 1969.
- [12] A. R. West, T. B. Adams, F. D. Morrison, and D. C. Sinclair, "Novel high capacitance materials:- BaTiO<sub>3</sub>:La and CaCu<sub>3</sub>Ti<sub>4</sub>O<sub>12</sub>," *J. Eur. Ceram. Soc.*, vol. 24, no. 6, pp. 1439–1448, 2004.
- [13] K. Tsuda, R. Sano, and M. Tanaka, "Nanoscale local structures of rhombohedral symmetry in the orthorhombic and tetragonal phases of BaTiO<sub>3</sub> studied by convergent-beam electron diffraction," *Phys. Rev. B - Condens. Matter Mater. Phys.*, vol. 86, no. 21, 2012.
- [14] H. Takahasi, "A note on the theory of barium titanate," *J. Phys. Soc. Jpn.*, vol. 16, p. 1685, 1961.
- [15] S. a Hayward and E. K. H. Salje, "The pressure temperature phase diagram of BaTiO<sub>3</sub> : a macroscopic description of the low-temperature behaviour," *J. Phys. Condens. Matter*, vol. 14, pp. 599–604, 2002.
- [16] P. Maksymovych *et al.*, "Intrinsic nucleation mechanism and disorder effects in polarization switching on ferroelectric surfaces," *Phys. Rev. Lett.*, vol. 102, no. 1, 2009.
- [17] Y. Zhang, J. Hong, B. Liu, and D. Fang, "Molecular dynamics investigations on the size-dependent ferroelectric behavior of BaTiO<sub>3</sub> nanowires," *Nanotechnology*, vol. 20, no. 40, 2009.

- [18] J. D. Jackson, "Classical Electrodynamics Third Edition," *John Wiley & Sons, INC.* pp. 75–79, 1999.
- [19] I. Petousis *et al.*, "High-throughput screening of inorganic compounds for the discovery of novel dielectric and optical materials," *Sci. Data*, vol. 4, p. 160134, 2017.
- [20] Q. Zhang, T. Cagin, and W. A. Goddard, "The ferroelectric and cubic phases in BaTiO<sub>3</sub> ferroelectrics are also antiferroelectric," *Proc. Natl. Acad. Sci.*, vol. 103, no. 40, pp. 14695–14700, 2006.
- [21] F. Endres and P. Steinmann, "Molecular statics simulations of ferroelectric barium titanate in the rhombohedral phase," *GAMM Mitteilungen*, vol. 38, no. 1, pp. 132–146, 2015.
- [22] V. Boddu, F. Endres, and P. Steinmann, "Molecular dynamics study of ferroelectric domain nucleation and domain switching dynamics," *Sci. Rep.*, vol. 7, no. 1, 2017.
- [23] J. M. Vielma and G. Schneider, "Shell model of BaTiO<sub>3</sub> derived from ab-initio total energy calculations," *J. Appl. Phys.*, vol. 114, no. 17, p. 174108, 2013.
- [24] G. Gautschi, *Piezoelectric Sensorics*. Berlin, Heidelberg: Springer Berlin Heidelberg, 2002.
- [25] T. Ikeda, *Fundamentals of piezoelectricity*. Oxford University Press, 1996.
- [26] A. L. Kholkin, N. A. Pertsev, and A. V. Goltsev, "Piezoelectricity and crystal symmetry," in *Piezoelectric and Acoustic Materials for Transducer Applications*, 2008, pp. 17–38.
- [27] H. Maiwa, "Piezoelectric properties of BaTiO<sub>3</sub> ceramics prepared by hot isostatic pressing," *Nippon Seramikkusu Kyokai Gakujutsu Ronbunshi/Journal Ceram. Soc. Japan*, vol. 121, no. 1416, 2013.
- [28] P. Zubko, G. Catalan, and A. K. Tagantsev, "Flexoelectric Effect in Solids," *Annu. Rev. Mater. Res.*, vol. 43, no. 1, pp. 387–421, Jul. 2013.
- [29] L. Shu, X. Wei, T. Pang, X. Yao, and C. Wang, "Symmetry of flexoelectric coefficients in crystalline medium," in *Journal of Applied Physics*, 2011, vol. 110, no. 10.
- [30] L. Shu *et al.*, "Converse flexoelectric coefficient f1212 in bulk Ba<sub>0.67</sub>Sr<sub>0.33</sub>TiO<sub>3</sub>," *Appl. Phys. Lett.*, vol. 104, no. 23, 2014.
- [31] W. Ma and L. E. Cross, "Flexoelectricity of barium titanate," *Appl. Phys. Lett.*, vol. 88, no. 23, 2006.
- [32] S. Plimpton, "Fast parallel algorithms for short-range molecular dynamics," *J. Comput. Phys.*, vol. 117, no. 1, pp. 1–19, 1995.
- [33] "Official LAMMPS Site." [Online]. Available: <http://lammps.sandia.gov/index.html>.
- [34] A. Asthagiri, Z. Wu, N. Choudhury, and R. E. Cohen, "Advances in first-principles studies of transducer materials," in *Ferroelectrics*, 2006, vol. 333, pp. 69–78.
- [35] "LAMMPS Units." [Online]. Available: <http://lammps.sandia.gov/doc/units.html>.
- [36] F. Jin *et al.*, "Equilibration and thermalization of classical systems," *New J. Phys.*, vol. 15, 2013.
- [37] "LAMMPS Triclinic." [Online]. Available: [http://lammps.sandia.gov/doc/Section\\_howto.html#howto-12](http://lammps.sandia.gov/doc/Section_howto.html#howto-12).

- [38] “Stereographic Projection.” [Online]. Available: <http://pille.iwr.uni-heidelberg.de/~kugeln/mathstereoprod.html>.
- [39] T. Ishidate, S. Abe, H. Takahashi, and N. Môri, “Phase Diagram of BaTiO<sub>3</sub>,” *Phys. Rev. Lett.*, vol. 78, no. 12, pp. 2397–2400, 1997.
- [40] V. Petrovsky, T. Petrovsky, S. Kamlapurkar, and F. Dogan, “Dielectric constant of barium titanate powders near curie temperature,” *J. Am. Ceram. Soc.*, vol. 91, no. 11, pp. 3590–3592, 2008.
- [41] “LAMMPS Indenters.” [Online]. Available: [http://lammmps.sandia.gov/doc/fix\\_indent.html](http://lammmps.sandia.gov/doc/fix_indent.html).
- [42] L. T. Kong, “Phonon dispersion measured directly from molecular dynamics simulations,” *Comput. Phys. Commun.*, vol. 182, no. 10, pp. 2201–2207, 2011.
- [43] “LAMMPS Phonons.” [Online]. Available: [http://lammmps.sandia.gov/doc/fix\\_phonon.html](http://lammmps.sandia.gov/doc/fix_phonon.html).
- [44] S. Tinte, M. G. Stachiotti, M. Sepliarsky, R. L. Migoni, and C. O. Rodriguez, “Atomistic modelling of BaTiO<sub>3</sub> based on first-principles calculations,” *J. Phys. Condens. Matter*, vol. 11, no. 48, pp. 9679–9690, 1999.
- [45] D. Khatib, R. Migoni, G. E. Kugel, and L. Godefroy, “Lattice dynamics of BaTiO<sub>3</sub> in the cubic phase,” *J. Phys. Condens. Matter*, vol. 1, no. 49, pp. 9811–9822, 1989.

## APPENDIX

### A: DATABASE

The database attached with this thesis is a directory within the main *Master Thesis* folder containing three subdirectories:

- *MATLAB Figures*
- *Simulations*
- *Software*

*MATLAB Figures* – Contains all the pictures in the thesis built with the custom-made software written in MATLAB® R2018a (Academic License).

*Simulations* – Contains all the LAMMPS *input scripts*, initial coordinates files, electric field scripts, *log files*, *dumps* and *shell launcher* files for the 13 simulations detailed in the *experimental section*:

- ✚ *Reference\_100, Reference\_220 & Reference\_300*
- ✚ *Induced\_Thermalization*
- ✚ *Phase\_Diagram\_0, Phase\_Diagram\_2, Phase\_Diagram\_4 & Phase\_Diagram\_6*
- ✚ *Hysteresis\_100, Hysteresis\_220, Hysteresis\_300 & Hysteresis\_400*

*Software* – Contains an updated copy of *BTO\_Visuals* and *BTO\_generator* up to the latest debugged version (28 May 2018). Moreover, there is a *Special Functions* directory containing tools employed for building the phase diagram and hysteresis loops, and for visualizing the three strain gradients described in appendix B. Even more, all the simulations contained in the *Simulations* directory are copied and pre-processed in the *BTO\_Visuals* main directory; thereby, the thesis results can be directly reproduced and the custom-made software can be easily explored.

### B: STRAIN GRADIENTS

As stated in section 4.4. of the *results and discussion* chapter, simple strain gradient configurations are wanted when analyzing flexoelectric response. In this thesis, three strain gradients were derived and discussed, leading to the employment of the *accordion bending* shown in figure 39. The derivations of the *wedge*, *circular* and *accordion* strain gradients in plane deformation conditions are shown below.

## 1.1. WEDGE DEFORMATION

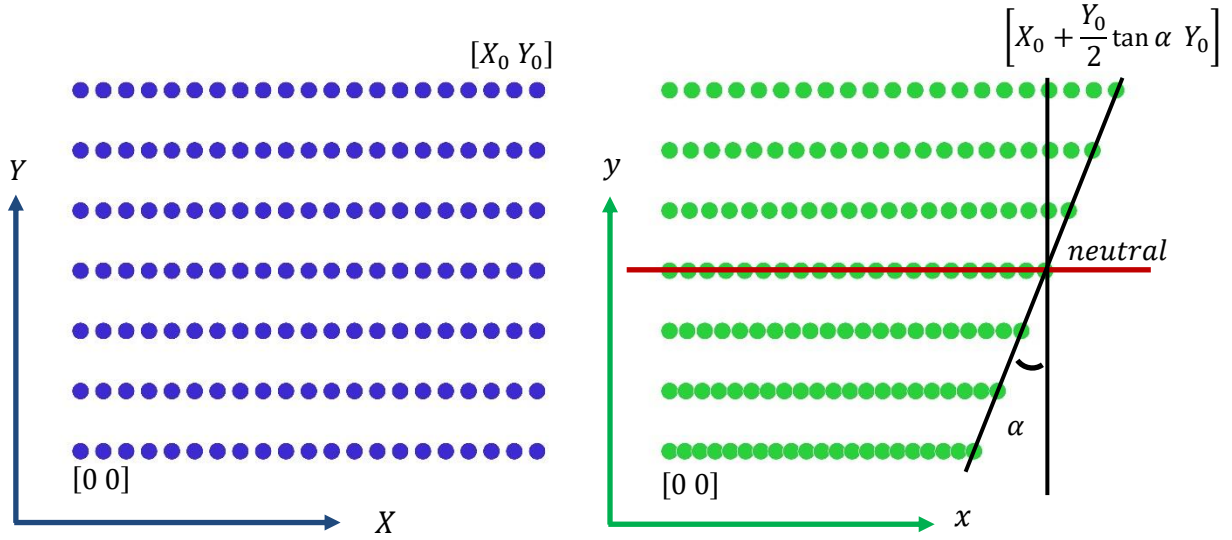


Figure 42 – Derivation of the wedge transformation for a grid of 21x7 test points. The lower half of the box gets compressed meanwhile the upper expands; thus, generating a neutral axis in the middle. The coordinates of the lower-left and upper-right corners are shown before and after the transformation.

When transforming the right edge of the original box, any point of the form  $[X_0 \quad Y]$  will be mapped to  $\left[X_0 + \left(Y - \frac{Y_0}{2}\right) \tan \alpha \quad Y_0\right]$ ; moreover, the vertical coordinate is always invariant:  $y = Y$ . Thus, by requiring the points to be x-equidistant for any value of  $y$ , the following map is satisfied:

$$\frac{X_0}{n} \rightarrow \frac{X_0 + \left(Y - \frac{Y_0}{2}\right) \tan \alpha}{n} = \frac{X_0}{n} \left[1 + \left(Y - \frac{Y_0}{2}\right) \frac{\tan \alpha}{X_0}\right]$$

Equation (A.1)

With  $n$  a positive number. Thereby, in the limit  $n \rightarrow \infty$ , the next infinitesimal relation holds:

$$dX \rightarrow dX \left[1 + \left(Y - \frac{Y_0}{2}\right) \frac{\tan \alpha}{X_0}\right]$$

Equation (A.2)

Then, by straightforward integration, the mapping function is obtained:

$$\begin{bmatrix} x \\ y \end{bmatrix} = \begin{bmatrix} 1 + \left(Y - \frac{Y_0}{2}\right) \frac{\tan \alpha}{X_0} & 0 \\ 0 & 1 \end{bmatrix} \begin{bmatrix} X \\ Y \end{bmatrix}$$

Equation (A.3)

The map is Y-dependent and non-linear; nevertheless, linearity is recovered locally when choosing some value of Y. Calculating the deformation gradient  $[F]$  yields (see equation 18):

$$[F] \doteq \begin{bmatrix} 1 + kY & kX \\ 0 & 1 \end{bmatrix}$$

Equation (A.4)

By defining  $k = \frac{\tan \alpha}{X_0}$  and the Y-translation  $\left(Y - \frac{Y_0}{2}\right) \rightarrow Y$ . Using equation (17) for computing the strain tensor  $[S]$  and then calculating the strain gradient tensor gives:

$$[S] \doteq \begin{bmatrix} (1 + kY)^2 - 1 & (1 + kY)kX \\ (1 + kY)kX & (kx)^2 \end{bmatrix}$$

$[\partial S] = \text{terms of order 1 or zeros}$

Equation (A.5)

Therefore, the wedge deformation strain tensor  $[\partial S]$  is relatively simple due to its linear character; nevertheless, it has 6 non-zero values. Achieving such deformation state could be possible by using plane indenters in the top, left edge and bottom of the original box, together with a tilted-plane indenter positioned at the right edge.

## 1.2. CIRCULAR BENDING

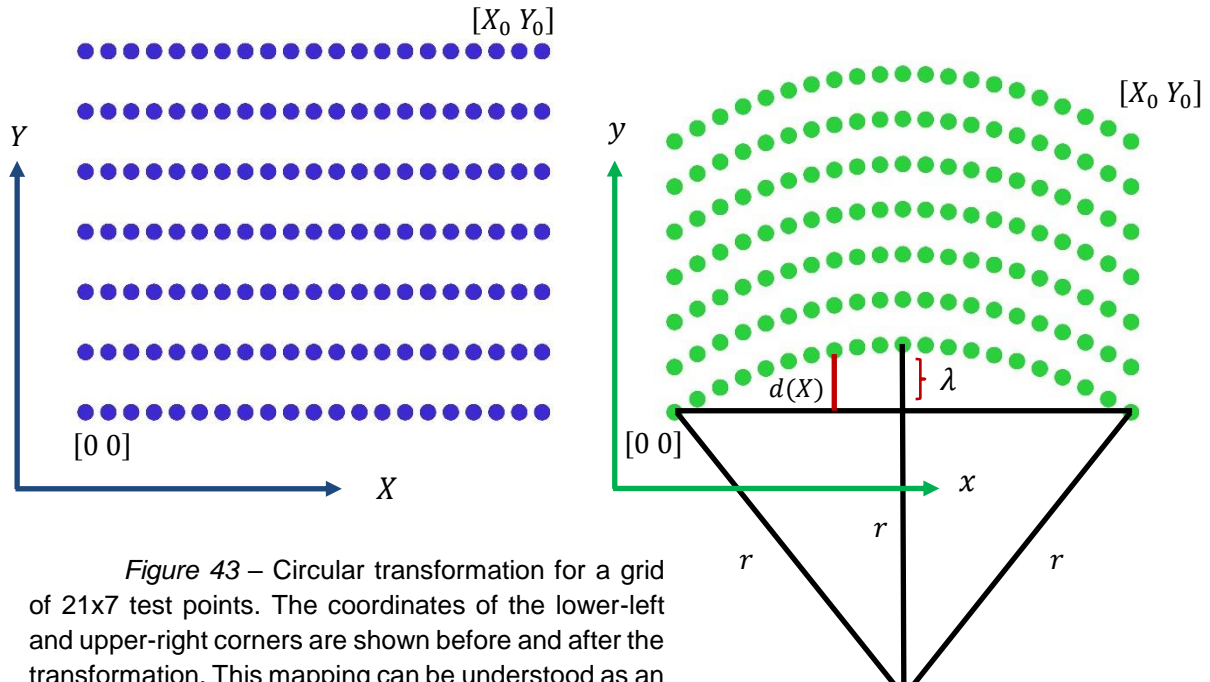


Figure 43 – Circular transformation for a grid of 21x7 test points. The coordinates of the lower-left and upper-right corners are shown before and after the transformation. This mapping can be understood as an increment in the vertical direction whose magnitude is dependent of the horizontal position. In this case the increment is given by the distance between the chord and arc of a circle of radius  $r$ .

This case, the horizontal coordinate remains invariant:  $x = X$ , meanwhile the vertical coordinate obeys the mapping  $Y \rightarrow Y + d(X)$ , on which  $d(X)$  are the positive y-coordinate values in the equation of the circle:

$$\left(x - \frac{X_0}{2}\right)^2 + [y + (r - \lambda)]^2 = r^2$$

Equation (B.1)

Furthermore, noticing that the point  $[0 \ 0]$  satisfies the equation above, the radius  $r$  can be written in terms of the parameters  $X_0$  and  $\lambda$ , yielding:

$$r = \frac{1}{2\lambda} \left[ \frac{X_0^2}{4} + \lambda^2 \right]$$

Equation (B.2)

The introduction of these parameters is very practical for controlling the amount of bending. On the other hand, combining the two last equations yields an expression of  $d(X)$  which is dependent on a square root; therefore, the derivatives of  $d(X)$  will not vanish and the strain gradient  $[\partial S]$  will have a very complex analytical expression. A general calculation of the strain tensor yields:

$$[S] \doteq \frac{1}{2} \begin{bmatrix} d'(X)^2 & d'(X) \\ d'(X) & 0 \end{bmatrix}$$

Equation (B.3)

Therefore, only three components of  $[\partial S]$  will be non-zero:

$$\frac{\partial S_{xx}}{\partial X} = d'(x)d''(x)$$

$$\frac{\partial S_{xy}}{\partial X} = \frac{\partial S_{yx}}{\partial X} = \frac{1}{2}d''(x)$$

Equation (B.4)

Unfortunately, the explicit expressions for the case of circular deformation are far too complicated to be practical. The circular strain gradient can be achieved using plane indenters at the left and right edges of the original box and circular indenters of the same radius at the top and bottom. Although analogous configurations testing other geometries than circular are theoretically simpler due to the reduction of order after taking subsequent derivatives (parabolic, polynomial, etc.), LAMMPS does not support these indenter geometries; nonetheless, these could be defined as in the case of the tilted-plane indenter.

### 1.3. ACCORDION BENDING

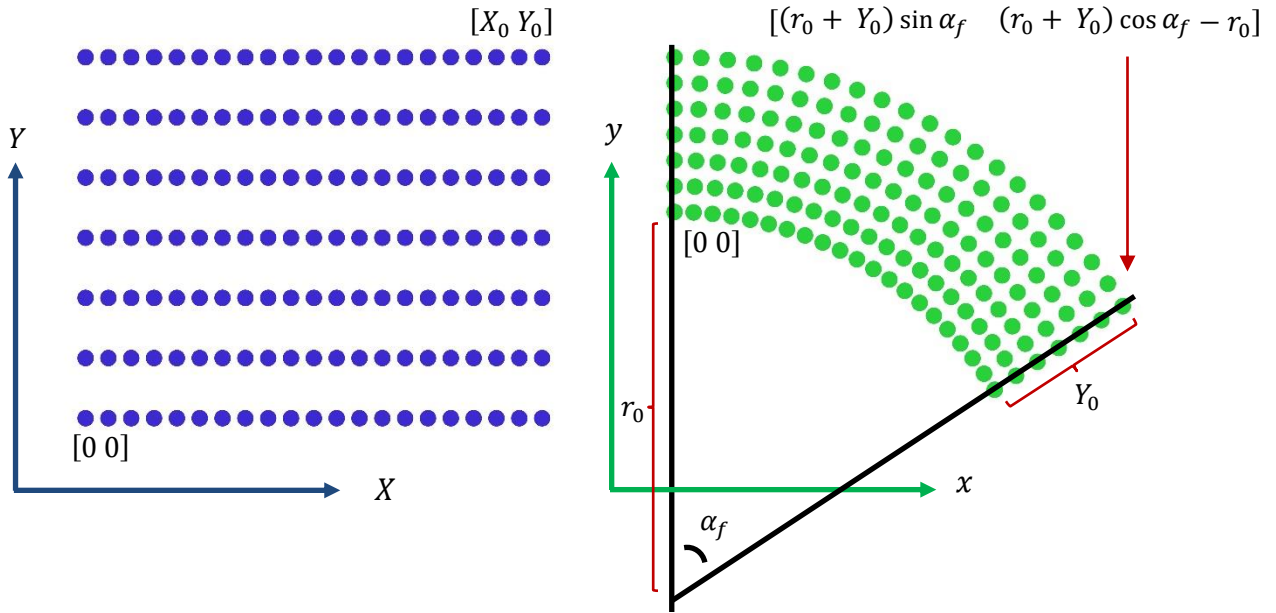


Figure 44 – Accordion transformation for a grid of  $21 \times 7$  test points. The coordinates of the lower-left and upper-right corners are shown before and after the transformation. This mapping can be understood as arching the test box by an angle  $\alpha_f$ .

The coordinates of the deformed configuration can be described in terms of the displaced polar map:

$$x = r \sin \alpha$$

$$y = r \cos \alpha - r_0$$

Equation (C.1)

Furthermore, the thickness of the test box is required to be invariant under the transformation; therefore, the identification  $r = r_0 + Y$  can be made. Also, the arclength of the deformed configuration for some value  $Y$  can be written:

$$s = (r_0 + Y)\alpha = k(Y)X$$

Equation (C.2)

On which a linear function  $k(Y)$  is defined as the scale factor of the X-coordinate during the deformation. Hence, evaluating the arclength in  $[X_0 0]$  and  $[X_0 Y_0]$  yields:

$$k(0) = \frac{r_0}{X_0} \alpha_f$$

$$k(Y_0) = \frac{(r_0 + Y_0)}{X_0} \alpha_f$$

Equation (C.3)

Then, from the linearity requirement, the function  $k(Y)$  is found to be:

$$k(Y) = \frac{(r_0 + Y)}{X_0} \alpha_f$$

Equation (C.4)

Therefore, solving equation (C.2) for  $\alpha$  and substituting in equation (C.1) the final expression for the mapping function is obtained:

$$\begin{aligned} x &= (r_0 + Y) \sin\left(\frac{\alpha_f}{X_0} X\right) \\ y &= (r_0 + Y) \cos\left(\frac{\alpha_f}{X_0} X\right) - r_0 \end{aligned}$$

Equation (C.5)

Using equation (17) and (18) for computing the strain tensor  $[S]$  gives:

$$[S] \doteq \frac{1}{2} \begin{bmatrix} \left[(r_0 + Y) \frac{\alpha_f}{X_0}\right]^2 - 1 & 0 \\ 0 & 0 \end{bmatrix}$$

Equation (C.6)

Thus, the strain gradient  $[\partial S]$  has only one non-zero component:

$$\frac{\partial S_{xx}}{\partial Y} = (r_0 + Y) \left(\frac{\alpha_f}{X_0}\right)^2$$

Equation (C.7)

Which depends linearly on  $Y$ . Furthermore, the geometrical parameters are all known. The accordion configuration can be achieved using a plane indenter on the left edge of the original box, a tilted-plane on the right edge, and circular indenters of radius  $r_0$  and  $r_0 + Y_0$  at the bottom and top, respectively. It should be noticed that in the three strain gradient configurations derived here, an external stress field exists in the supercell due to the presence of the indenters. Calculating these fields can be approximated from knowing the indentation area and the exerted force per particle.

## DEFINITIONS

Physical Fidelity	Relates to the degree to which the simulation replicates the physical properties of the system under study.
Computational Efficiency	Also known as algorithmic efficiency, is the number of computational resources needed to perform a certain task.
Long-term stability	Property of a simulation which shows an acceptable degree of deterioration due to accumulated floating-point round-off errors or unexpected long-term behavior of the interaction potential which may lead to crashing and/or loss of physical fidelity.
Statistical Ensemble	Physical idealization consisting of all virtual copies of a system each one representing one possible state the system might be in.
Partition Function	Sum over the possible states of a system of the probability distribution function induced by a certain statistical ensemble; for example, the NVT partition function is given by:
$Z = \sum_i e^{-\beta E_i}$ <span style="float: right;">Equation (D.1)</span>	
<p>On which <math>e^{-\beta E_i}</math> is the Boltzmann distribution, <math>\beta = 1/k_B T</math> is the Boltzmann factor and <math>E_i</math> is the energy of the i-th microstate of the system.</p>	
Kinetic Energy	The kinetic energy of a system of $N$ particles is defined as the sum of the individual kinetic energies:
$K = \frac{1}{2} \sum_{i=1}^N m_i \mathbf{v}_i \cdot \mathbf{v}_i$ <span style="float: right;">Equation (D.2)</span>	
Equipartition Theorem	Not on its most general form, the classical theorem states that the average kinetic energy for a 3D system of $N$ particles in thermal equilibrium is shared equally among all the particles, such that:
$\langle K \rangle = \frac{3}{2} N k_B T$ <span style="float: right;">Equation (D.3)</span>	
<p>On which <math>\langle \rangle</math> represents the ensemble average. Therefore, from equations D.2 and D.3 the temperature of the system can be measured to be:</p>	

$$T = \frac{1}{3Nk_B} \left\langle \sum_{i=1}^N m_i \mathbf{v}_i \cdot \mathbf{v}_i \right\rangle$$

Equation (D.4)

Similarly, it can be proved that an expression for the system pressure in the case of pairwise potentials  $\phi(r_{ij})$  is given by:

$$P = \frac{1}{3V} \left\langle \sum_{i=1}^N \left( m_i \mathbf{v}_i \cdot \mathbf{v}_i - \sum_{j>i} \frac{\partial \phi(r_{ij})}{\partial r_{ij}} r_{ij} \right) \right\rangle$$

Equation (D.5)

Which is a statement of the Clausius virial equation.

Maxwell-Boltzmann distribution

For a 3D system of non-interacting particles (like at the initialization step of a MD simulation), the Maxwell-Boltzmann probability distribution of velocities is given by:

$$f(v) = \left( \frac{m}{2\pi k_B T} \right)^{3/2} 4\pi v^2 e^{-mv^2/2k_B T}$$

Equation (D.6)

Which depends on the mass of the particles and on temperature (both defined by the user in a MD simulation).

Gaussian distribution of velocities

A normal distribution with a mean set to zero can be used to assign initial particle velocities in a rather simpler way:

$$f(v) = \left( \frac{m}{2\pi k_B T} \right)^{-1/2} e^{-mv^2/2k_B T}$$

Equation (D.7)

Which depends on the mass of the particles and on temperature (both defined by the user in a MD simulation).

Voigt notation

Convention made in linear algebra to represent symmetric tensors by reducing its order; for example, in the case of the stress tensor the convention reads:

$$\begin{bmatrix} \sigma_{11} & \sigma_{12} & \sigma_{13} \\ \sigma_{21} & \sigma_{22} & \sigma_{23} \\ \sigma_{31} & \sigma_{32} & \sigma_{33} \end{bmatrix} \rightarrow \begin{bmatrix} \sigma_{11} \\ \sigma_{22} \\ \sigma_{33} \\ \sigma_{23} \\ \sigma_{13} \\ \sigma_{12} \end{bmatrix} \rightarrow \begin{bmatrix} \sigma_1 \\ \sigma_2 \\ \sigma_3 \\ \sigma_4 \\ \sigma_5 \\ \sigma_6 \end{bmatrix}$$

The rule can be generalized and applied for higher rank tensors.

## ACRONYMS

<i>MD</i>	<i>Molecular Dynamics</i>
<i>BTO</i>	<i>Barium Titanate</i>
<i>EPR</i>	<i>Electric Paramagnetic Resonance</i>
<i>NMR</i>	<i>Nuclear Magnetic Resonance</i>
<i>CBED</i>	<i>Convergent-Beam Electron Diffraction</i>
<i>DFT</i>	<i>Density Functional Theory</i>
<i>PBEsol</i>	<i>Perdew-Burke-Ernzehof generalized gradient approximation for solids</i>
<i>HIP-BT</i>	<i>Hot Isostatic-Pressed Barium Titanate</i>
<i>LAMMPS</i>	<i>Large-scale Atomic/Molecular Massively Parallel Simulator</i>
<i>GUI</i>	<i>Graphical User Interface</i>

## MATHEMATICAL CONVENTIONS

Vectors $\in \mathbb{R}^3$	Represented with bold characters
Tensors $\in \mathbb{R}^3 \otimes \dots \otimes \mathbb{R}^3$	Represented with bold characters and enclosed in brackets
Matrix representations	Represented with bold characters and indexed
$\doteq$	The symbol reads: “The tensor is represented by”
Number with hat	Negative of the number